



**NTNU – Trondheim**  
Norwegian University of  
Science and Technology

# Operational modal analysis of the Dolmsundet Bridge during construction

**Ruth Hetland**

Civil and Environmental Engineering

Submission date: June 2015

Supervisor: Ole Andre Øiseth, KT

Norwegian University of Science and Technology  
Department of Structural Engineering





## MASTER THESIS 2015

SUBJECT AREA: Structural Dynamics	DATE: 20.06.2015	NO. OF PAGES:
--------------------------------------	---------------------	---------------

TITLE:

**Operational modal analysis of the Dolmsundet Bridge during construction**

**Modalanalyse av Dolmsundbrua i byggefasen**

BY:

Ruth Hetland



**SUMMARY:** This study investigates the dynamic behaviour of a cantilever bridge during construction. The investigations are carried out using operational modal analysis techniques. The Second-Order Blind Identification (SOBI) Method is implemented in MATLAB. This method is tested and compared with analytical results obtained from a shear frame with non-proportional damping properties. The accuracy is investigated for several damping ratios, and the quality of the results are considerably reduced for higher damping ratios. The method showed noteworthy improvement for longer time series durations. Modal analysis of the Dolmsundet Bridge measurements were carried out with SOBI method and compared with results from Covariance-driven Stochastic Subspace Identification. Similar modes obtained from the two methods showed little deviation in the obtained frequencies. The influence of the temporary support structure is found to be significant. Predicted values are available for two periods during construction. The numerically predicted stage one follows the tendency found from the measurements, while the numerically predicted building stage two shows significant deviation from the observed tendency. The last mode of interest in the experimental data appears at a lower frequency than the numerically predicted mode. The damping estimates are more scattered. The predicted damping ratio appears to be non-conservative for the investigated wind loading. Modal parameters obtained from a more extensive dataset will contribute to updates of analytical models, increase knowledge and contribute to the safety during construction stage under more challenging conditions.

RESPONSIBLE TEACHER: Associate Professor Ole Andre Øiseth

SUPERVISOR(S) Associate Professor Ole Andre Øiseth, Ph.D. Candidate Knut Andreas Kvåle

CARRIED OUT AT: Department of Structural Engineering



**Institutt for konstruksjonsteknikk**

FAKULTET FOR INGENIØRVITENSKAP OG TEKNOLOGI  
NTNU – Norges teknisk-naturvitenskapelige universitet

## **MASTEROPPGAVE 2015**

for

*Ruth Hetland*

### **Modalanalyse av Dolmsundbrua i byggefasen**

*Operational modal analysis of the Dolmsundet Bridge during construction*

Dolmsundbrua er for tiden under bygging og planlegges ferdigstilt i 2016. Brua bygges etter fritt frambygg prinsippet, hvilket innebærer at det kan oppstå uønskede svingninger i byggefasen før konstruksjonen sammenkobles. For å kunne utvikle en bedre forståelse for denne konstruksjonstypens dynamiske oppførsel i byggefasen er det installert et omfattende målesystem som registrerer vind, tøyninger og akselerasjoner. Denne oppgaven dreier seg om modalanalyse av brua i byggefasen.

Oppgaven bør inneholde følgende temaer:

- Grunnleggende teori for modalanalyse.
- Implementering av en metode for modalanalyse.
- Estimert av demping, frekvenser og moder.
- Grundig analyse av usikkerheter.
- Diskusjon av hvordan konstruksjonens egenskaper endres under bygging.

Besvarelsen organiseres i henhold til gjeldende retningslinjer.

*Veileder(e):* Ole Andre Øiseth, Knut Andreas Kvåle

NTNU, 16.3.2015

Ole Andre Øiseth  
Faglærer



## Abstract

This study investigates the dynamic behaviour of a cantilever bridge during construction. The investigations are carried out using operational modal analysis techniques. The Second-Order Blind Identification (SOBI) Method is implemented in MATLAB. This method is tested and compared with analytical results obtained from a shear frame with non-proportional damping properties. The accuracy is investigated for several damping ratios, and the quality of the results are considerably reduced for higher damping ratios. The method showed noteworthy improvement for longer time series durations. Modal analysis of the Dolmsundet Bridge measurements were carried out with SOBI method and compared with results from Covariance-driven Stochastic Subspace Identification. Similar modes obtained from the two methods showed little deviation in the obtained frequencies. The influence of the temporary support structure is found to be significant. Predicted values are available for two periods during construction, received from the Norwegian Public Roads Administration. The numerically predicted stage one follows the tendency found from the measurements, while the numerically predicted second building stage shows significant deviation from the observed tendency. The last mode of interest in the experimental data appears at a lower frequency than the numerically predicted mode. The damping estimates are more scattered. The predicted damping ratio appears to be non-conservative for the investigated wind loading. Modal parameters obtained from a more extensive dataset will contribute to updates of analytical models, increase knowledge and contribute to the safety during construction stage under more challenging conditions.





## Sammendrag

Dynamiske egenskaper til en fritt frembygg bro i byggefasen er undersøkt ved hjelp av modal analyse. Systemidentifikasjons metoden, *Second-Order Blind Identification* (SOBI) er implementert i MATLAB. Metoden er testet og sammenlignet med analytiske verdier fra en skjær ramme med ikke-proporsjonale dempings egenskaper. Nøyaktigheten er undersøkt for flere dempingsstadier og var betydelig redusert ved høyere dempingsforhold. Analyse av lengre tidsserier gave mindre avvik fra analytiske verdier. Estimer fra målinger fra Dolmsundbrua er funnet med SOBI metoden og sammenlignet med estimer fra system identifikasjons metoden; *covariance-driven Stochastic Subspace Identification*. Lignende moder fra disse metodene viste lite avvik i egenfrekvensverdier. Innvirkning av oppført midlertidig hjelpesøyle kommer tydelig frem i analysen. Numerisk predikerte moder er tilgjengelig fra to perioder under bygging, motatt av Statens Vegvesen. Det numerisk beregnet byggesteget nummer en følger en observert trend funnet fra målingene, mens byggesteg nummer to avviker fra dette. Dempingsestimer fra analysen er spredte, og regnes som dels usikre. Dempingsforhold påsatt beregninger ser ut til å være ikke-konservative for den undersøkte vindbelastningen. Modale parametre hentet fra et mer omfattende datasett vil kunne bidra til oppdateringer av analytiske modeller, øke kunnskapen og dermed bidra til økt sikkerhet i byggefasen.



## Preface

This master thesis is the final dissertation for the M.Sc degree at the Department of Structural Engineering at the Norwegian University of Science and Technology (NTNU). The master thesis has been carried out under supervision of Associate Professor Ole Øiseth and PhD Candidate Knut Andreas Kvåle.

I will give thanks to Associate Professor Ole Andre Øiseth for helpful guidance throughout the master thesis. I am grateful for this opportunity, and the new encountered knowledge of operational modal analysis has been educational and challenging.

I have received generous support from Ph.D Candidate Knut Andreas Kvåle, which is highly appreciated. Thanks for your open door, and willingness to help.

An additional thanks are going to people at Norwegian Public Roads Administration and Cautus Geo, which provided measurement data and reports I needed. I appreciated your fast email answers and willingness to help.

I would also like to thank fellow student, Ingrid Simensen, for helpful and constructive discussions throughout the semester.

*Ruth Hetland*

*Trondheim, June 2015*



# Contents

<b>LIST OF FIGURES.....</b>	<b>III</b>
<b>LIST OF TABLES.....</b>	<b>VII</b>
<b>LIST OF ABBREVIATIONS .....</b>	<b>IX</b>
<b>LIST OF SYMBOLS.....</b>	<b>XI</b>
<b>CHAPTER 1 INTRODUCTION.....</b>	<b>1</b>
1.1 BACKGROUND .....	2
1.2 SCOPE OF WORK .....	3
1.3 STRUCTURE OF THE REPORT.....	4
<b>CHAPTER 2 THEORY.....</b>	<b>5</b>
2.1 RANDOM DATA.....	5
2.1.1 <i>Processes</i> .....	5
2.1.2 <i>Basic concepts</i> .....	6
2.1.3 <i>Spectral density</i> .....	7
2.1.4 <i>White noise</i> .....	8
2.2 DYNAMICS OF MDOF.....	9
2.2.1 <i>Complex solution</i> .....	9
2.2.2 <i>MDOF system –Modal expansion</i> .....	10
2.2.3 <i>State-space formulation</i> .....	12
2.2.4 <i>Rayleigh damping</i> .....	14
2.2.5 <i>Damping, logarithmic decrement</i> .....	15
2.3 SIGNAL PROCESSING .....	16
2.3.1 <i>Concepts in signal processing</i> .....	16
2.3.2 <i>Fourier transformation</i> .....	16
2.3.3 <i>Leakage, windowing and zero padding</i> .....	17
2.3.4 <i>Welch method</i> .....	19
2.3.5 <i>Filters</i> .....	19
2.3.6 <i>Butterworth filter</i> .....	21

---

2.4	SYSTEM IDENTIFICATION METHODS .....	22
2.4.1	<i>Second Order Blind Identification method</i> .....	24
2.4.2	<i>Stochastic Subspace Identification</i> .....	30
2.4.3	<i>Quality check and comparison</i> .....	33
<b>CHAPTER 3</b>	<b>METHOD .....</b>	<b>37</b>
3.1	IMPLEMENTATION OF SYSTEM IDENTIFICATION METHOD.....	37
3.2	CASE STUDY I –IMPLEMENTATION OF SOBI ON A SHEAR FRAME .....	37
3.2.1	<i>Properties of 5DOF shear frame</i> .....	38
3.2.2	<i>Method</i> .....	38
3.2.3	<i>Result and considerations</i> .....	41
3.3	CASE STUDY 2 - OPERATIONAL MODAL ANALYSIS OF DOLMSUNDET BRIDGE.....	43
3.3.1	<i>Dolmsundet Bridge</i> .....	43
3.3.2	<i>Instrument positions</i> .....	45
3.3.3	<i>Description of file structure and importing considerations</i> .....	46
3.3.4	<i>Choice of time series</i> .....	49
3.3.5	<i>Validation of dataset</i> .....	49
3.3.6	<i>Signal processing</i> .....	52
3.3.7	<i>Second-order Blind Identification method</i> .....	54
3.3.8	<i>cov-SSI with MACEC software</i> .....	56
<b>CHAPTER 4</b>	<b>RESULTS AND DISCUSSION .....</b>	<b>61</b>
4.1	MODAL PARAMETERS FROM CONSTRUCTION STAGE 2.....	61
4.1.1	<i>Predicted modal parameters</i> .....	61
4.1.2	<i>Modal parameters obtained by SOBI</i> .....	62
4.1.3	<i>Modal parameters obtained by cov-SSI</i> .....	65
4.1.4	<i>Comparison of modal parameters obtained from SOBI and cov-SSI</i> .....	68
4.1.5	<i>Uncertainty considerations</i> .....	70
4.2	VARIATION OF MODAL PARAMETERS THROUGH DIFFERENT BUILDING STAGES.....	71
4.2.1	<i>Eigenfrequencies</i> .....	71
4.2.2	<i>Damping</i> .....	73
<b>CHAPTER 5</b>	<b>CONCLUDING REMARKS.....</b>	<b>75</b>
<b>CHAPTER 6</b>	<b>FURTHER WORK .....</b>	<b>77</b>
<b>CHAPTER 7</b>	<b>REFERENCES .....</b>	<b>79</b>
<b>A</b>	<b>SELECTED TIME SERIES .....</b>	<b>I</b>
<b>B</b>	<b>RESULT FROM ALL INVESTIGATED TIME SERIES .....</b>	<b>III</b>

# List of Figures

FIGURE 1.1 A) LOCATION OF DOLMSUNDET BRIGDE B) ILLUSTRATION OF PROPOSED STRUCTURE [4].....	2
FIGURE 2.1 PLOT OF TIME HISTORY OF WHITE NOISE OVER THE FREQUENCIES BETWEEN 0-5 Hz. PLOT B) AND C) REPRESENT THE VARIANCE SPECTRUM AND COVARIANCE OF THE BROAD BANDED WHITE NOISE.....	8
FIGURE 2.2 A) IS SAMPLED WITH NYQUIST FREQUENCY = 120 Hz. B) IS SAMPLED WITH 70 Hz AND EXHIBITS THE EFFECT OF ALIASING. ....	16
FIGURE 2.3 A SINUS CURVE WITH FREQUENCY 3 Hz OVER 7.5 s IS PLOTTED IN BOTH TIME AND FREQUENCY DOMAIN. A HANNING WINDOW IS APPLIED IN THE RIGHT HAND PLOTS. THE AMOUNT OF LEAKAGE IS REDUCED IN THE BOTTOM RIGHT PLOT, DUE TO THE WINDOWED TIME SERIES ABOVE.....	18
FIGURE 2.4 THE FREQUENCY RESPONSE OF TWO SINE CURVES WITH AMPLITUDE 1 AND FREQUENCIES 1 Hz AND 1.4 Hz ARE SHOWN IN THE FIGURE. THE SOLID LINE IS ZERO PADDED WITH FOUR TIMES AS MANY SAMPLES AS THE DOTTED CURVE. ....	19
FIGURE 2.5 THE PSD OF A ONE HOUR LONG TIME SERIES, OBTAINED FROM CASE STUDY1, IS CALCULATED WITH WELCH METHOD. PLOT A) IS CALCULATED WITH ONE WINDOWED SEGMENT. IN B), N SAMPLING VALUES IS DIVIDED INTO SEGMENTS WITH $K=N/15$ SAMPLING VALUES EACH WITH A 50% WINDOW OVERLAP. ....	19
FIGURE 2.6 SIGNAL WITH WHITE NOISE COMPARED WITH FILTERED SIGNAL (TO THE RIGHT). THE NOISE REMOVAL COULD BE VIEWED IN THE FREQUENCY DOMAIN, WHERE FREQUENCY ABOVE CUT OUT FREQUENCY 10 Hz IS ATTENUATED. A <code>FILTFILT()</code> MATLAB FUNCTION IS USED WHICH PRESERVE THE PHASE OF THE TIME SERIES.....	20
FIGURE 2.7 SPECIFICATION OF A LOW-PASS FILTER WITH IDEAL AND ACTUAL RESPONSE. THE TRANSITION BAND, PASSBAND, REJECT BAND DENOTES WHICH FREQUENCIES ARE ATTENUATED. THE CUT-OFF FREQUENCY IS 3 Hz WITH MAX RIPPLE 3 dB. ....	21
FIGURE 2.8 THE UPPER GRAPH SHOWS THE GAIN OF A BUTTERWORTH LOW PASS FILTER. WITH A CUT FREQUENCY OF 15 Hz, EQUAL TO $0.3 \times \pi/sample$ , HERE WITH $FS=1000$ . THE BOTTOM GRAPH SHOWS THE PHASE TREATED WITH <code>UNWRAP</code> . 22	22
FIGURE 2.9 A SCHEMATIC ILLUSTRATION OF THE COMBINED SYSTEM WITH WHITE NOISE INPUT AND THE FOURIER OF THE MEASURED RESPONSE. ....	22
FIGURE 2.10 FLOW CHART OF SECOND-ORDER BLIND IDENTIFICATION.....	24
FIGURE 3.1 ILLUSTRATION OF MDOF SHEAR FRAME AND NUMBERING OF DOFS.....	38
FIGURE 3.2 A-B) ILLUSTRATION OF CORRELATION MATRIX BEFORE AND AFTER APPLIED WHITENING AND JAD. ....	39
FIGURE 3.3 SOURCES, SHOWN FOR THE 60 FIRST SECOND, IS SHOWN TO THE LEFT. PSD OF SOURCES ARE SHOWN TO THE RIGHT WITH CORRESPONDING PEAK VALUE. ....	40
FIGURE 3.4 CORRELATION OF SOURCES, GIVEN WITH DAMPED FREQUENCIES, $fd$ . ....	40
FIGURE 3.5 THE SLOPE OF THE LINEAR CURVE GIVES AN ESTIMATED VALUE OF THE LOGARITHMIC DECREMENT. ....	41
FIGURE 3.6 MODE SHAPES FROM ANALYTICAL SOLUTION AND FROM THE MIXING MATRIX A. SCALED TO UNIT DISPLACEMENT IN DOF1. ....	42
FIGURE 3.7 ERROR OF DAMPING RATIO WITH RESPECT TO LENGTH OF THE ANALYSED SIGNAL.....	42

FIGURE 3.8 ERROR ESTIMATES FOR DIFFERENT DAMPING RATIOS.....	43
FIGURE 3.9 BRIDGE WITH DIMENSIONS, BEFORE CONNECTING TO ADJACENT CANTILEVER. ....	44
FIGURE 3.10 DOLMSUNDET BRIDGE UNDER CONSTRUCTION. A) VIEW FROM DOLMSUNDET TOWARDS HITRA [30] B) CANTILEVER WITH FORM TRAVELLER ON THE CANTILEVER EDGES [31].....	44
FIGURE 3.11. INCLUDED ELEMENTS IN THE DIFFERENT ANALYSIS M1-M4, WITH DATES OF THE OBTAINED MEASUREMENTS.....	45
FIGURE 3.12 INSTRUMENT POSITIONS WITH LOCAL AND GLOBAL COORDINATES. ....	46
FIGURE 3.13 ACCELEROMETER POSITIONS ALONG THE SPAN. ....	46
FIGURE 3.14 OVERVIEW OVER FILE STORAGE. ....	47
FIGURE 3.15 FLOW CHART OF IMPORT PROCEDURE.....	48
FIGURE 3.16 ILLUSTRATION OF 60 SAMPLES, SAMPLED WITH FS=100. BLUE STARS DENOTES ORIGINAL SERIES, RED CIRCLES ARE ADDED THE SERIES IN THE INTERPOLATION.....	48
FIGURE 3.17 WIND DIRECTION A) CARTESIAN COORDINATES B) POLAR COORDINATES. ....	50
FIGURE 3.18 WIND TIME SERIES, DISTRIBUTION AND PSD PLOT FOR VERTICAL- AND HORIZONTAL WIND SPEEDS. ....	50
FIGURE 3.19 ACCELERATION TIME SERIES.....	51
FIGURE 3.20 THE RAW DATA ACCELERATIONS DO NOT FOLLOW A GAUSSIAN DISTRIBUTED, IN A), AND ARE BANDPASS FILTERED, SHOWN IN B).....	51
FIGURE 3.21 THE LINEAR INTERPOLATION CREATES DROPOUTS IN THE SIGNAL. ....	52
FIGURE 3.22 APPLIED FILTER BUTTERWORTH FILTER OF ORDER 5, WITH LOWER $f_c$ OF 3 HZ AND HIGHER $f_c$ OF 0.14 HZ. ....	53
FIGURE 3.23 ACCELERATION TIME SERIES, TOP PLOT, AND SPECTRAL DENSITY, BOTTOM PLOT, BEFORE AND AFTER APPLIED FILTER. .....	53
FIGURE 3.24 CHOICE OF NM ACTIVE MODES. NOISE IS SEEN IN THE TWO BOTTOM TIME SERIES. ....	54
FIGURE 3.25. CROSS CORRELATION MATRIX OF SOURCES FOR TIME-LAGS 1:1000. ....	55
FIGURE 3.26 IDENTIFIED SOURCES WITH PEAK SPECTRAL DENSITY PLOT .....	55
FIGURE 3.27 AUTOCORRELATION FUNCTIONS WITH RESPECT TO NUMBER OF TIME-LAGS, $\tau$ .....	55
FIGURE 3.28 ZERO CROSSINGS AND MAXIMA OF AUTOCORRELATION FUNCTION FROM SOURCE 1.....	56
FIGURE 3.29 LINEAR REGRESSION OF THE LOGARITHMIC DECREMENT .....	56
FIGURE 3.30 A) SCREENSHOT OF SSI WINDOW IN MACEC B) SINGULAR VALUE PLOT.....	57
FIGURE 3.31 USER INTERFACE IN MACEC OF THE STABILIZATION DIAGRAM, PROVIDED WITH VARIANCE LIMITS.....	59
FIGURE 3.32 STABILIZATION DIAGRAM, WITHOUT VARIANCE LIMITS, 5 MODES ARE SELECTED IN FREQUENCY RANGE FROM 0.2-1 Hz. ....	60
FIGURE 4.1 AUTOMAC MATRIX OF MODES OBTAINED FROM SOBI. ....	65
FIGURE 4.2 AUTOMAC MATRIX OF THE MODES FORM COV-SSI .....	67
FIGURE 4.3 SCATTER DIAGRAM REPRESENTING THE SCATTER BETWEEN MODE SHAPE VECTORS OBTAINED FROM THE TWO METHODS. ....	68
FIGURE 4.4 CROSSMAC MATRIX OF SOBI AND COV-SSI MODES.....	69
FIGURE 4.5 FREQUENCY VARIATION FOR CONSTRUCTION STAGE M1-4.....	72
FIGURE 4.6 FREQUENCY VARIATION FOR CONSTRUCTION STAGE M1-M4 AND NUMERICALLY PREDICTED MODES IN B21 AND B22. .....	73



---

FIGURE 4.7 MEAN VALUES OF DAMPING RATIOS FOR DIFFERENT CONSTRUCTION STAGES.....	74
FIGURE B.1 A) STABILIZATION DIAGRAM B) AUTOMAC MATRIX, TIME SERIES ID01 .....	V
FIGURE B.2 A) STABILIZATION DIAGRAM B) AUTOMAC MATRIX, TIME SERIES ID02 .....	VII
FIGURE B.3 CROSSMAC MATRIX, COMPARING MODES FROM COV-SSI AND SOBI. ....	VIII
FIGURE B.4 STABILIZATION DIAGRAM, ID03. ....	IX
FIGURE B.5 STABILIZATION DIAGRAM .....	XI
FIGURE B.6 A) STABILIZATION DIAGRAM B) AUTOMAC MATRIX OF MODES FROM COV-SSI, TIME SERIES ID05 .....	XIII
FIGURE B.7 CROSS CORRELATION MATRIX FROM SOBI, TIME SERIES ID05 .....	XIV
FIGURE B.8 STABILIZATION DIAGRAM OBTAINED FROM TIME SERIES ID06 .....	XV
FIGURE B.9 STABILIZATION DIAGRAM FROM ID08 .....	XVII



# List of Tables

TABLE 3-1 PROPERTIES OF SYSTEM 1 AND 2, CASE STUDY 1 .....	38
TABLE 3-2 RESULT, SYSTEM 1A .....	41
TABLE 3-3 RESULTS, SYSTEM 2A.....	42
TABLE 4-1 PREDICTED EIGENFREQUENCIES AND MODE SHAPES FOR CONSTRUCTION STAGE B22. ILLUSTRATION AND FREQUENCIES ARE OBTAINED FROM CALCULATION REPORT PROVIDED BY THE NORWEGIAN PUBLIC ROADS ADMINISTRATION [32].....	62
TABLE 4-2 RESULT OBTAINED BY SOBI, TIME SERIES ID07, CONSTRUCTION STAGE M4. ....	63
TABLE 4-3 ILLUSTRATION OF MODES OBTAINED FROM SOBI, AND LABELLED WITH ASSUMED MODE SHAPE DESCRIPTION. ....	63
TABLE 4-4 RESULT OBTAINED BY COV-SSI, TIME SERIES ID07, CONSTRUCTION STAGE M4. INCLUDED WITH $2\sigma$ CONFIDENCE INTERVAL.....	65
TABLE 4-5 ILLUSTRATION OF MODES AND COMPLEXITY PLOT OBTAINED FROM COV-SSI AND LABELLED WITH ASSUMED MODE SHAPE DESCRIPTION .....	66
TABLE 4-6 RELATIVE SCATTER AND MAC VALUES COMPARING SOBI MODES WITH COV-SSI.....	68
TABLE 4-7 MODES CHOSEN TO BE COMPARED FOR DIFFERENT CONSTRUCTION STAGES.....	69
TABLE 4-8 FREQUENCIES OBTAINED FROM CASTING STAGE M1-M4, FREQUENCIES ARE GIVEN AS SOBI/SSI.....	71
TABLE 4-9 FREQUENCIES AND MODE LABELS FROM PREDICTED CONSTRUCTION STAGES B21 AND B22, MODE 1-3.....	72
TABLE 4-10 DAMPING RATIOS OBTAINED FROM CASTING STAGE M1-M4, GIVEN FROM TWO METHODS SOBI/SSI .....	73
TABLE A-1 DATE AND TIME OF COLLECTED TIME SERIES .....	I
TABLE A-2 TIME SERIES WITH CORRESPONDING FILENAMES. ....	I
TABLE B-1 PARAMETERS VARIATIONS FOR DIFFERENT TIME SERIES.....	III
TABLE B-2 COV-SSI RESULT FROM TIME SERIES ID01, GIVEN WITH $2\sigma$ CONFIDENCE INTERVAL .....	V
TABLE B-3 SOBI RESULT FROM TIME SERIES ID01 .....	V
TABLE B-4 COMPARISON OF SOBI AND SSI MODES FROM TIME SERIES ID01.....	V
TABLE B-5 COV-SSI RESULT FROM TIME SERIES ID02, GIVEN WITH $2\sigma$ CONFIDENCE INTERVAL .....	VII
TABLE B-6 SOBI RESULTS FROM TIME SERIES ID02.....	VII
TABLE B-7 COMPARISON OF SOBI AND SSI MODES FROM TIME SERIES ID02.....	VII
TABLE B-8 COV-SSI RESULT FROM TIME SERIES ID03 .....	IX
TABLE B-9 SOBI RESULTS FROM TIME SERIES ID03.....	IX
TABLE B-10 COMPARISON OF SOBI AND SSI MODES FROM TIME SERIES ID03.....	IX
TABLE B-11 COV-SSI RESULT FROM TIME SERIES ID04 .....	XI
TABLE B-12 SOBI RESULT FROM TIME SERIES ID04 .....	XI
TABLE B-13 COMPARISON OF SOBI AND SSI MODES FROM TIME SERIES ID04.....	XII
TABLE B-14 COV-SSI RESULT FROM TIME SERIES ID05 .....	XIII

---

TABLE B-15 SOBI RESULT FROM TIME SERIES ID05 .....	XIII
TABLE B-16 COMPARISON OF SOBI AND SSI MODES FROM TIME SERIES ID05.....	XIV
TABLE B-17 COV-SSI RESULT FROM TIME SERIES ID06 .....	XV
TABLE B-18 SOBI RESULT FROM TIME SERIES ID06 .....	XV
TABLE B-19 COMPARISON OF SOBI AND SSI MODES FROM TIME SERIES ID06.....	XV
TABLE B-20 COV-SSI RESULT FROM TIME SERIES ID08 .....	XVII
TABLE B-21 SOBI RESULT FROM TIME SERIES ID08 .....	XVII
TABLE B-22 COMPARISON OF SOBI AND SSI MODES FROM TIME SERIES ID08.....	XVII

---

## List of Abbreviations

BMID	Blind Modal Identification
BSS	Blind Source separation
cov-SSI	Covariance driven Stochastic Subspace Identification
dB	Decibel
DFT	Discrete Fourier transform
DOF	Degree Of Freedom
EMA	Experimental Modal Analysis
FEM	Finite Element Model
FFT	Fast Fourier transform
FRF	Frequency Response Function
IMAC	International Modal Analysis Conference
IRR	Infinite Impulse Response
JAD	Joint Approximate Diagonalization
LTI	Linear time-invariant system
MAC	Modal assurance criterion
MDOF	Multi-degree of freedom
MP	Mean Phase
MPC	Modal Phase Collinearity
MPD	Mean Phase Deviation
ODEs	Ordinary differential equations
OMA	Operational Modal Analysis
PSD	Power Spectral Density
SDOF	Single Degree of Freedom
SOBI	Second-order blind identification
SSI	Stochastic Subspace Identification
SVD	Singular Value Decomposition
ZOH	Zero order hold
SHM	Structural Health Monitoring



## List of Symbols

$[ \ ]$	Matrix
$[ \ ]^T$	Matrix transpose
$[ \ ]^+$	Pseudoinverse
$[ \ ]^{-1}$	Matrix inverse
$\{ \ }$	Column vector
$[ \hat{\ } ]$	Estimate of $[ \ ]$
$\cdot$	Time derivative, $\frac{d}{dt}$
$a_0, a_1$	Rayleigh damping coefficients
$\{a\}$	Vector of constants
$[A]$	Discrete-time state matrix (State-space) /mixing matrix (SOBI)
$[A_c]$	State matrix in continuous time
$[A']$	Unitary matrix
$[\tilde{A}]$	Unitary matrix from optimization problem
$[B]$	Selection matrix/Discrete time input matrix
$[\bar{B}]$	Location of inputs in State-space model
$[B_c]$	Input influence matrix (continuous time)
$[C]$	Damping matrix/ Discrete-time output influence matrix /combination matrix ( SOBI)
$[C_a], [C_v], [C_d]$	Selection matrices for acceleration, velocity and displacement
$[C_c]$	Output influence matrix
$[C_x]$	Covariance matrix for variable vector $\{x(t)\}$
$C_{xx}$	Autocovariance of variable $x$
$C_{xy}$	Autocovariance of variable $x$ and $y$
$[\tilde{C}]$	Modal equivalent damping matrix
$[D]$	Discrete-time direct transmission matrix/ Diagonal eigenvalue matrix
$[D_c]$	Direct transmission matrix
$e$	The natural logarithm
$E[ \ ]$	Statistical expectancy value of random variable, equal $\mu$
$[E]$	Matrix of the right singular vectors from SVD

---

$f_n$	Natural frequency
$f_s$	Sampling frequency
$\hat{f}$	Fourier transform of signal $f$
$f_c$	cut-off frequency
$\{f(t)\}$	Nodal forces
$[F]$	Factor in robust whitening
$F(\omega)$	Force in frequency domain
$G(\omega)$	Gain (filters)
$[G]$	Next state-output covariance matrix
$H(\omega)$	Frequency response function
$i$	Imaginary unit/number of block rows
$[I]$	Identity matrix
$Im(\cdot)$	Imaginary part of complex number
$[K]$	Stiffness matrix
$[\tilde{K}]$	Modal equivalent stiffness matrix
$[M]$	Mass matrix
$[\tilde{M}]$	Modal equivalent mass matrix
$\{n(t)\}$	sensor noise
$N_m$	Number of modes
$N_r$	Number of DOFs
$N(\omega)$	With noise in frequency domain
$[O_i]$	Observability matrix
$\{\tilde{P}\}$	Load vector
$q_n(t)$	Modal coordinate for mode $n$
$[R_i]$	Output correlation matrix at time-lag $i$
$R_{xx}$	Autocorrelation of variable $x$
$R_{xy}$	Cross-correlation of variables $x$ and $y$
$Re(\cdot)$	Real part of complex number
$[R]$	Correlation matrices
$\{s(t)\}$	State vector (State-space model)/Source (SOBI)
$\{\dot{s}(t)\}$	Change in the state vector
$\{s_k\}$	Discrete-time state vector
$S_{xx}$	Autospectral density of variable $x$
$S_{xy}$	Cross-spectral density of variable $x$ and $y$



---

$S_{xy}^+$	One-sided cross-spectral density
$S_0$	Constant autospectral density
$\Delta t$	Time interval
$[T_{i j}]$	Block Toeplitz matrix, entries on first row equals correlations from time lag $i$ to $j$
$[T]$	Non-singular square matrix
$\{u(t)\}$	Time variation of the input (state-space model)
$[U]$	Demixing matrix (SOBI)
$[U_1]$	Matrix of the left singular vectors corresponding to nonzero singular values
$\{v_k\}$	Measurement noise
$[V]$	Orthogonal eigenvector matrix
$[V_1]$	Matrix of the right singular vectors corresponding to nonzero singular values
$\{w_k\}$	Process noise
$[W]$	Whitening matrix in SOBI
$\{x(t)\}$	Signal part of observed data (in SOBI)/time-series
$x(t)$	Random variable
$\{y(t)\}, \{\dot{y}(t)\}, \{\ddot{y}(t)\}$	MDOF displacement, velocity and acceleration vectors
$\{y(t)\}$	measured output (SOBI)/observation equation (SSI)
$\{y_l(t)\}$	Observation vector at location $l$
$\{y_k\}$	Observation equation in discrete time
$Y(\omega)$	System output in frequency domain
$[Y]$	Observed data signals, SSI
$\{z(t)\}$	Whitened data
$[W]$	Whitening matrix in SOBI
$\alpha_i$	Contribution factor, robust whitening
$[\Gamma_i]$	Reversed controllability matrix
$\delta$	Logarithmic decrement
$\delta(\tau)$	Kronecker delta for time-lag $\tau$
$\Delta$	Small increment
$\lambda$	Continuous-time pole/eigenvalue
$\mu$	Discrete-time pole/mean
$\sigma^2$	Statistical Variance
$\sigma_x^2$	Statistical variance of variable $x$

$\tau$	time-lag
$[\Sigma]$	Diagonal matrix of singular values
$[\Sigma_1]$	Sub-matrix of $[\Sigma]$ , only nonzero singular values
$[\phi]$	Mode shape matrix
$\{\phi\}$	Mode shape
$\xi$	Damping ratio
$\omega$	Angular frequency

## Chapter 1 Introduction

*“Understanding the dynamic response of large civil structures improves design and safety, extends life, and reduces maintenance.”* Stated in the IMAC, A conference on Structural Dynamics [1].

Civil engineering structures are built in correspondence to planning based on engineering calculations. Finite Element Model (FEM) programs are an excellent tool for structural analysis. However, with an increasing complexity of the structures, the need for an additional tool to support and validate the numerical analysis is evident. In dynamic analysis, parameters and effects such as damping, friction and fatigue properties are hard to predict[2]. Values of structural damping used for calculations are usually rough estimates based on assumptions from similar structures. A more accurate prediction could increase physical insight and improve structural performance and integrity. Modal analysis can be performed in order to identify characteristics and properties of the structure of interest. Modal parameters such as eigenvalues, eigenfrequencies and corresponding mode shapes, give knowledge of the dynamic system. This can be used to validate or upgrade the analytic model or to increase knowledge of built structures.

It is of interest to better understand the behavior of a cantilever bridge under construction. Cantilever bridges are frequently built for spans between 100-300 m in Norway. They are preferable because of their efficient construction [3]. As the name implies, the bridge is built from both sides, standing as a cantilever before being connected at the middle. The dynamic demands are largest during construction, and this will often give the dimension criteria of the bridge. Dolmsundet Bridge is constructed as a cantilever bridge, and is the structure of interest in this study. A measurement system is installed on the bridge so that dynamical behavior throughout the building process can be investigated.

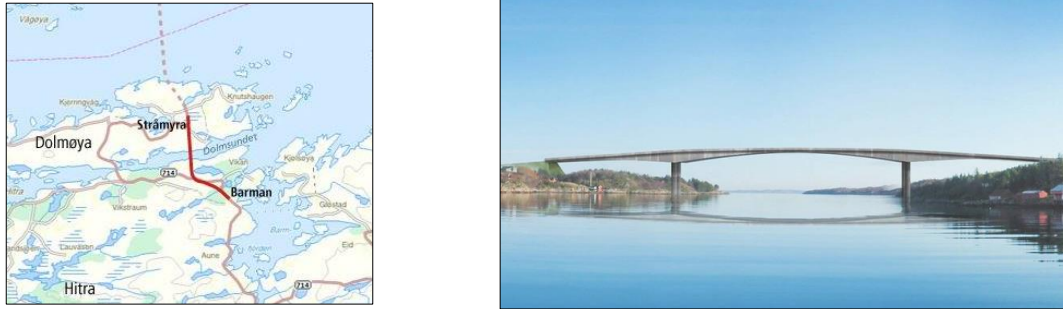


Figure 1.1 a) Location of Dolmsundet bridge b) Illustration of proposed structure [4].

Dolmsundet Bridge crosses Dolmsundet, connecting Hitra and Dolmøya, shown in Figure 1.1. The new bridge will reduce the road Fv. 714 by almost 6 km, and thus reduce transport road as well as increase road safety. It is estimated to open over summer 2016. As of June 2015, both cantilevers spanning from the column at the Hitra side are constructed, and the measurements are collected from this structure before connecting to adjacent cantilevers. The construction of the cantilevers spanning from the column positioned at Dolmøya are about to start.

## 1.1 Background

Operational, experimental or combined modal analysis are separated into three different steps [5].

1. Collection of data and preprocessing
2. System identification
3. Determination of modal characteristics (modal analysis)

Hence, the terminology modal analysis is defined as both the processing and the determination of modal characteristics.

Dynamic characteristics can be identified through deterministic investigation by artificial excitation and corresponding vibration, noted as Experimental Modal Analysis (EMA). This is challenging for civil engineering structures, due to their large size and low frequencies. The development of Operational Modal Analysis (OMA) has increased in the last few decades, and the methods are mostly derived from the EMA methods. OMA uses excitation from the environment as an unknown load on the structure, such as wind and traffic, and is therefore suitable for civil engineering structures. It is solved as an inverse problem, where output is known, but either input or system characteristics are unknown. In OMA, the normal approach is to make an assumption about the input and solve for the unknown system

---

characteristics. It is developed in a stochastic framework for analysis of random signals. A vast amount of relevant articles are produced in the field. Rainieri and Fabbrocino (2014) [6] have gathered relevant research and background information in their book “Operational Modal Analysis of Civil Engineering Structure”, which is useful in this study. OMA of civil engineering structures has tools for understanding dynamics of advanced structures and update and verify analytical models. Progress has also been made in the field of Automated OMA, which provides possible applications in the field of civil Structural Health Monitoring (SHM). SHM is an active research field that includes investigation of how Modal Analysis testing can be used to detect damage in the structures.

The Second-Order Blind Identification (SOBI) method is studied in detail. This method was chosen for several reasons. The method has not been previously implemented at the department of structural engineering at NTNU, and would increase their knowledge base. Additionally, it is not a part of the MATLAB toolbox MACEC which includes several state of the art methods. The method has become popular as the interest in automated codes increases. Combining this method with other methods, or implementing modified versions of the method can give an automated modal analyses with reliable results. [7]

## 1.2 Scope of work

Modal analysis is not common knowledge for most civil engineers, so a lot of time is devoted to review of the different OMA methods available and to common practice in the field of OMA. The SOBI method is implemented in MATLAB. A benchmark shear frame is created to serve as a quality check of the implemented method. Modal analysis of Dolmsundet Bridge during construction will be carried out by the SOBI method in this study. The commercial software MACEC, with the covariance-driven Stochastic Subspace Identification (SSI) method is used for comparison of the estimates. The result will be compared on the basis of estimated damping, frequencies and mode shapes. A FEM analysis of the bridge has been performed by Norwegian Public Roads Administration and is used for further comparison. The validity of the estimates will be discussed.

It should be noted that the data acquisition system provided for this study appeared less comprehensive than assumed. The strain sensors were found inadequate for dynamical investigation, due to low sampling rate. The accelerometer sensor had an adequate sampling rate, and will therefore be used. The sensor location was firstly assumed to be on both cantilevers but were found to be on the same cantilever late in the study.

### 1.3 Structure of the report

Necessary theories for understanding, implementing and performing the modal analysis method are outlined in Chapter 2. Stochastic processes and system identification are unfamiliar for most civil engineers. The statistical foundation of modal analysis is fundamental, and therefore emphasized in the explanation. The implemented modal analysis methods are explained in detail as well as common procedures for obtaining consistency and quality of results.

Chapter 3 presents the method.. The method is split into two case studies. The first case study concentrates on the implementation of SOBI performed on a benchmark shear frame model. As the results are important for further studies, they are presented and discussed in the method part case 1. The second case study is the analysis of the cantilever bridge, performed with both the SOBI and the SSI method for different time of occurrences.

The results and discussion are presented in Chapter 4. Concluding remarks and suggestions of further work are presented in Chapter 6 and Chapter 7 respectively. The material is presented on a level suitable for engineering students with fundamental structural dynamic courses.

## Chapter 2 Theory

### 2.1 Random data

An introduction to terminology and techniques for analysis of random processes will be provided. Basic statistics are assumed known and stochastic processes are emphasized in the explanation. Dynamic analyses are performed in both deterministic and stochastic framework. A deterministic analysis requires a known load time history; thus, the observed data must be able to be described by an explicit mathematical relationship. A random property characterizes several physical processes, and each observation of the process will be unique. It must therefore be described in terms of statistical properties, as in the case of wave and wind generated loads.

#### 2.1.1 Processes

A stochastic process is the collection of all possible sample functions representing a random phenomenon, also called a random process. A single time history, also noted as a sample function or ensemble, may be regarded as a realization of a stochastic process as defined by Bendat and Piersol [8].

A random process is defined to be stationary if the statistical properties of one instance are equal for all points in time. Næss [9] defines a process to be weakly stationary if the mean;

$$\mu_x(t) = E[x_k(t)] \quad (2.1)$$

and the autocorrelation;

$$R_{xx}(\tau) = E[x_k(t)x_k(t + \tau)] \quad (2.2)$$

is independent of  $t$ .  $x_k(t)$  is a random variable over the index  $k$ . The autocorrelation in Equation (2.2) will be explained in the next section. Higher order moments can prove strong stationary. In the case of Gaussian processes, weak stationarity implies strong stationarity since all possible probability distributions depends on mean values and covariance functions [8]. As defined by Næss (2008) [9], the process is ergodic if every ensemble mean in a stationary process can be replaced by a time average over a single realization. Hence, the

autocorrelation and mean value will be independent of the realization being studied. The property of an ergodic process makes it possible to use one single time history to estimate statistical parameters of the process.

### 2.1.2 Basic concepts

Stationarity is assumed in the following description of statistical properties. Autocorrelation gives the correlation between different instants in a single ensemble. The term ‘auto’ indicates that only one time history is involved. The autocorrelation function,  $R_{xx}(\tau)$ , is defined in Equation (2.2) and can be estimated by direct computation from realizations as [8]:

$$\hat{R}_{xx}(r\Delta t) = \frac{1}{N-r} \sum_{n=1}^{N-r} x_n x_{n+r} \quad r = 0, 1, 2, \dots, m \quad (2.3)$$

Where  $r$  is the number of time-lag intervals,  $\Delta t$  is an equally spaced time interval,  $m$  is the maximum lag number and  $N$  is the length of the time series investigated. Autocorrelations are even functions with respect to time-lag intervals, thus only positive lags need to be considered.

$R_{xy}$  is the cross-correlation function between the time series  $\{x(t)\}$  and  $\{y(t)\}$ . Cross-correlation gives the relationship between two different time series, either of two different realizations of the same process or from two different processes [10], given by:

$$R_{xy}(\tau) = E[x_k(t)y_k(t + \tau)] \quad (2.4)$$

Autocorrelation is a special case of the cross-correlation. The cross-correlation can be estimated from realizations from:

$$\hat{R}_{xy}(r\Delta t) = \frac{1}{N-r} \sum_{n=1}^{N-r} x_n y_{n+r} \quad r = 0, 1, 2, \dots, m \quad (2.5)$$

Where  $r$  is the lag number,  $N$  is the length of time series,  $\Delta t$  is an equally spaced time interval,  $m$  is the maximum lag number, and  $x$  and  $y$  are different realizations. Cross-correlations are not even, but satisfy the relationship  $R_{xy}(-\tau) = R_{yx}(\tau)$ . The relationship between covariance and correlation is:

$$C_{xx}(\tau) = R_{xx}(\tau) - \mu_x^2 \quad (2.6)$$



$$C_{xy}(\tau) = R_{xy}(\tau) - \mu_x \mu_y$$

Hence, two stationary random processes are uncorrelated if  $C_{xy}(\tau) = 0$ , as this implies a correlation  $R_{xy}(\tau) = \mu_x \mu_y$ , and they are thus independent of each other. Correlation and cross-correlation functions are identical with covariance and cross-covariance functions for a zero mean process. The covariance with time-lag equal to zero equals the variance.

$$\sigma_x^2 = C_{xx}(0) \quad (2.7)$$

A vector process  $\{x(t)\}$ , containing several ensembles, is stationary if all component processes are stationary and jointly stationary [9]. Thus, the variance and cross spectra components can be collected into a covariance matrix. The covariance matrix is then independent of  $t$  and defined as:

$$[C_x(\tau)] = \begin{bmatrix} C_{1,1}(\tau) & C_{1,2}(\tau) & \cdots \\ C_{2,1}(\tau) & C_{2,2}(\tau) & \cdots \\ \vdots & \vdots & \ddots \end{bmatrix} \quad (2.8)$$

Where the diagonal terms are the autocovariances and the off diagonal terms equal the cross-covariance between the different realizations.

### 2.1.3 Spectral density

The variance spectrum is defined as the Fourier transform of the covariance function [9]. A closer look at the Fourier transform is provided in section 2.3.2. The variance spectrum is also known as the power spectral density, the energy spectrum, the spectral density or just the spectrum [9]. It shows how the variances are distributed along the frequency axis. The autospectral density function,  $S_{xx}(\omega)$ , and cross-spectral density function,  $S_{xy}(\omega)$ , are given as:

$$S_{xx}(\omega) = \frac{1}{2\pi} \int_{-\infty}^{\infty} C_{xx}(\tau) e^{-i\omega\tau} d\tau \quad (2.9)$$

$$S_{xy}(\omega) = \frac{1}{2\pi} \int_{-\infty}^{\infty} C_{xy}(\tau) e^{-i\omega\tau} d\tau \quad (2.10)$$

The cross-variance  $S_{xy}(\omega)$  can also be calculated directly from the realizations by a Fast Fourier transform algorithm (FFT) and the covariance can then be found from the inverse Fourier transform of the variance spectrum:

$$C_{xy}(\tau) = \int_{-\infty}^{\infty} S_{xy}(\omega) e^{i\omega\tau} d\omega \quad (2.11)$$

A one-sided spectral density function is often used, since it is represented with positive, and thus physically realizable, frequencies. One-sided spectral density function,  $S_{xy}^+(\omega)$ , is defined as:

$$S_{xy}^+(\omega) = \begin{cases} 2S_{xy}(\omega) & \omega \geq 0 \\ 0 & \omega < 0 \end{cases} \quad (2.12)$$

#### 2.1.4 White noise

The white noise spectrum is a broad banded spectrum where the spectrum is constant for all frequencies. In theory, this distribution will give an infinite variance. According to Næss (2013) [9], the process will, in practice, be regarded as white noise if the largest frequency  $f_2$  is significantly higher than all other relevant frequencies. A Gaussian white noise ensemble can be simulated with the  $randn(\cdot)$  function in MATLAB. One of the shortcomings of this function is that it provides slightly different results depending on the number of segments used. A time history and a constant spectrum from a broad banded process is visualized in Figure 2.1, with sample frequency 10 Hz.

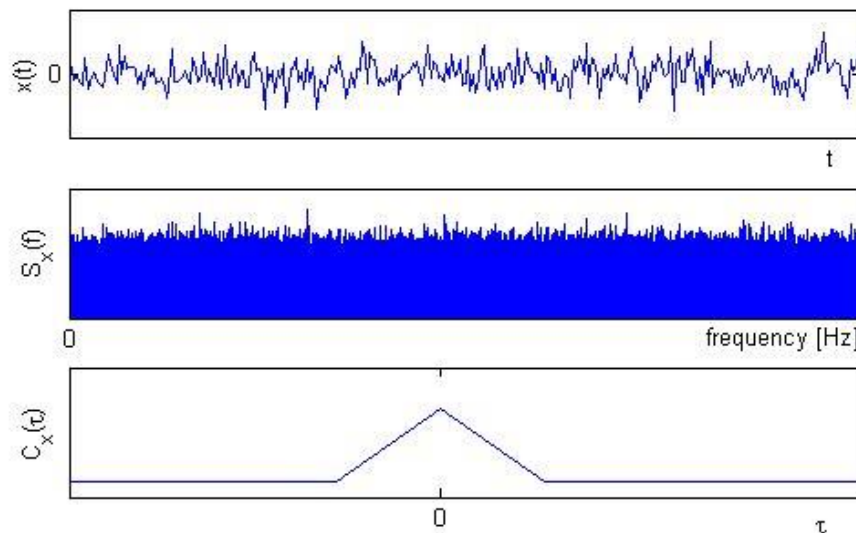


Figure 2.1 Plot of time history of white noise over the frequencies between 0-5 Hz. Plot b) and c) represent the variance spectrum and covariance of the broad banded white noise.

Note that the  $randn(\cdot)$  is used in Figure 2.1, and the figure deviates from perfect white noise conditions. The auto covariance should be represented with a spike at time-lag zero, and zero elsewhere. The covariance function of broad banded spectrum is defined as: [9]

$$C_x(\tau) = S_0 \int_{-\infty}^{\infty} e^{-i\omega\tau} d\omega = 2\pi S_0 \delta(\tau) \quad (2.13)$$

where  $\delta(\tau)$  is the Kronecker delta, and  $S_0$  denotes constant auto-spectral density. In a broad-banded process, the autocorrelation decreases rapidly for increasing time-lags, which represents a weak statistical dependence between the values at different time instants.

## 2.2 Dynamics of MDOF

A multiple degree of freedom (MDOF) system can be described with a linear, second order differential equation in matrix form as given below:

$$[M]\{\ddot{y}(t)\} + [C]\{\dot{y}(t)\} + [K]\{y(t)\} = [B]\{f(t)\} \quad (2.14)$$

The matrices  $[M]$ ,  $[C]$ , and  $[K]$  denote the mass, damping and stiffness matrices for the given structural system. The vector  $\{f(t)\}$  contains the nodal forces and  $\{y(t)\}$  describes the nodal displacements. The matrix  $[B]$  is the selection matrix which connects the loads to the respective degrees of freedom (DOF), and  $t$  is the time. The undamped eigenfrequencies,  $\omega_n$ , and associated real-valued modes,  $\{\phi_n\}$ , can be solved as a classic eigenvalue problem;

$$\begin{aligned} ([K] - \omega_n^2[M])\{\phi_n\} &= 0 \\ \det([K] - \omega_n^2[M]) &= 0 \end{aligned} \quad (2.15)$$

This solution is valid for proportional, also called classical, damped systems. Proportional damping is present if the matrix  $[K][M]^{-1}[C]$  is symmetrical. A non-proportional damped system can only be solved by complex solutions since its undamped frequencies will deviate from the undamped frequencies found by classical eigenvalue problem in Equation (2.15).

### 2.2.1 Complex solution

The homogenous solution of Equation (2.14) can be assumed to be of the form:

$$\{y(t)\} = \{a\}e^{\lambda t} \quad (2.16)$$

Here,  $\{a\}$  is as a vector of constants and the pole,  $\lambda$ , is a scalar. Inserting equation (2.16) into the homogenous equation (2.14), with  $\{f(t)\} = 0$ , yields:

$$(\lambda^2[M] + \lambda[C] + [K])\{a\} = \{0\} \quad (2.17)$$

The nonlinear eigenvalue problem can be solved by different approaches. A tutorial on the solution using a state space model is given by Lallement and Inman (1995) [11]. The obtained eigenvalues, denoted as poles,  $\lambda$ , are in complex conjugate pairs, given as [11]:

$$\lambda_r = -\xi_r \omega_r \mp i \omega_r \sqrt{1 - \xi_r^2} \quad (2.18)$$

The poles hold information about frequencies and damping ratios, where  $\omega_r$  is the  $r^{th}$  undamped natural frequency and  $\xi_r$  is the  $r^{th}$  modal damping ratio. Undamped frequency  $f_r$ , damped frequency  $f_{d,r}$ , and modal damping ratio  $\xi_r$  are obtained from the following relations:

$$f_r = \left| \frac{\lambda_r}{2\pi} \right| \quad (2.19)$$

$$f_{d,r} = \frac{Im(\lambda_r)}{2\pi} \quad (2.20)$$

$$\xi_r = \frac{-Re(\lambda_r)}{|\lambda_r|} \quad (2.21)$$

The vector of constants,  $\{a_r\}$ , corresponds to eigenvectors, given in complex pairs for the  $r^{th}$  mode. For proportional damping, the complex modes will equal real valued modes obtained from the undamped case with damping matrix  $[C] = [0]$ .

### 2.2.2 MDOF system –Modal expansion

The MDOF system in Equation (2.14) can be solved as modal analysis under the condition of linear system with classical damping. The total displacement can be represented as a superposition of modal contributions [12]:

$$y(t) = \sum_{n=1}^{\infty} \{\phi_n\} q_n(t) = [\phi] \{q(t)\} \quad (2.22)$$

$\{\phi_n\}$  is the mode shape with associated generalised coordinates,  $\{q_n(t)\}$ . Natural modes  $\{\phi_n\}$  are orthogonal and independent by definition, and are used as a basis for representing the displacement [12]. In a discrete format, the matrix  $[\phi]$  consists of  $n$  mode shapes with  $N_r$  global DOFs. The mode shape is given as:

$$\{\phi_n\} = [\phi_1 \quad \phi_2 \quad \cdots \quad \phi_{N_r}]^T \quad (2.23)$$

The generalized coordinate is a time dependent vector  $q_n(t)$  and will depend on the level of the excitation force.  $N_m$  is the number of modes included in order to represent the displacement. The generalized coordinate vector is defined [13]:

$$\{q(t)\} = [q_1 \quad q_2 \quad \cdots \quad q_{N_m}]^T \quad (2.24)$$

Introducing Equation (2.22) into Equation (2.14) and multiplying by  $[\phi]^T$ , the equation of motion can be expressed in modal coordinates as [13]:

$$[\phi]^T[M][\phi]\{\ddot{q}(t)\} + [\phi]^T[C][\phi]\{\dot{q}(t)\} + [\phi]^T[K][\phi]\{q(t)\} = [\phi]^T[B]\{f(t)\} \quad (2.25)$$

The modal equivalent structural properties are defined as;

$$\begin{aligned} [\tilde{M}] &= [\phi]^T[M][\phi] \\ [\tilde{C}] &= [\phi]^T[C][\phi] \\ [\tilde{K}] &= [\phi]^T[K][\phi] \end{aligned} \quad (2.26)$$

and the load vector becomes:

$$\{\tilde{P}\} = [\phi]^T[B]\{f(t)\} \quad (2.27)$$

Due to orthogonal properties of the mode shapes,  $[\tilde{M}]$  and  $[\tilde{K}]$  are diagonal matrices. Since classical damping is required,  $[\tilde{C}]$  will become a diagonal matrix.

Hence, the MDOF system consists of uncoupled diagonal matrices and can be divided into uncoupled single degree of freedom (SDOF) systems. The system is solved with respect to generalized coordinates and then transformed back into original coordinates by Equation (2.22). Thus, only  $N_{mod}$  equations need to be solved. For a system with few active modes and a large number of DOFs this may give a computational advantage. In a practical context, a few modes will yield reasonably accurate displacement estimate.

The spectral density of the displacement,  $S_{yy}(\omega)$ , is related to the spectral density of the modal coordinate,  $S_{qq}(\omega)$ , as given by Strømmen [13],

$$S_{yy}(\omega) = [\phi]S_{qq}(\omega)[\phi]^T \quad (2.28)$$

Since the modal shape matrix is independent of time, the relation can be shown to hold for the autocovariance by an inverse Fourier transform of the spectral density.

$$\int_{-\infty}^{\infty} C_{yy}(\tau) e^{i\omega\tau} d\tau = [\phi] \int_{-\infty}^{\infty} C_{qq}(\tau) e^{i\omega\tau} d\tau [\phi]^T \quad (2.29)$$

$$C_{yy}(\tau) = [\phi] C_{qq}(\tau) [\phi]^T \quad (2.30)$$

This relation will be useful in order to relate the autocovariance of modal coordinates to the response time series.

### 2.2.3 State-space formulation

State-space techniques represent mathematical models of physical systems and are a convenient method to analyze systems with multiple inputs and outputs [9]. This can be used to solve the linear dynamic model in Equation (2.14). The state-space model converts second order ordinary differential equations (ODEs) into coupled first order ODEs. This is done by partitioning the differential equation into a state equation and an observation equation. The following section outlines the state-space formulation by Rainier [6], and the reference can be used for further explanations.

The state variable, a state vector  $\{s(t)\}$ , holds the information about the system at a time instant, given as:

$$\{s(t)\} = \begin{Bmatrix} \{\dot{y}(t)\} \\ \{y(t)\} \end{Bmatrix} \quad (2.31)$$

The second-order ODE is rewritten as a first-order matrix equation, defined as the state equation. This equation expresses the change in the state vector:

$$\{\dot{s}(t)\} = [A_c]\{s(t)\} + [B_c]\{u(t)\} \quad (2.32)$$

$[A_c]$  is defined as the state matrix and transforms one state to the next state.  $[B_c]$  is the input influence matrix in continuous time. The vector,  $\{u(t)\}$ , represent time variation. Acceleration, velocity and displacement are measured in discrete locations and collected as linear combinations into an observation vector  $\{y_l(t)\}$ . Measured output at location  $l$  is represented by the observation equation:

$$\{y_l(t)\} = [C_a]\{\ddot{y}(t)\} + [C_v]\{\dot{y}(t)\} + [C_d]\{y(t)\} \quad (2.33)$$

Generalized for all locations, the observation equation is given as:

$$\{y(t)\} = [C_c]\{s(t)\} + [D_c]\{u(t)\} \quad (2.34)$$

$[A_c]$ ,  $[C_c]$  and  $[D_c]$  are considered to be the state-space matrices. They are determined by inserting the observation equation into Equation (2.14). The index  $c$  implies that the state-space matrices are in a continuous format.  $[A_c]$  is the state matrix as noted above.  $[C_c]$  is the output influence matrix, and consists of the output location for acceleration, velocity and displacements, which are held in the selection matrices  $[C_a]$ ,  $[C_v]$  and  $[C_d]$ .  $[D_c]$  is the direct transmission matrix and is only needed if accelerometers are used in the output measurements. The matrix  $[D_c]$  will reflect the changes in the time variation of the input,  $\{u(t)\}$ . The matrix  $[\bar{B}]$  contains information about locations of inputs. The state-space matrices are defined:

$$A_c = \begin{bmatrix} -[M]^{-1}[C] & [M]^{-1}[K] \\ [I] & [0] \end{bmatrix} \quad (2.35)$$

$$B_c = \begin{bmatrix} -[M]^{-1}[\bar{B}] \\ [0] \end{bmatrix} \quad (2.36)$$

$$C_c = \begin{bmatrix} [C_v] - [C_a][M]^{-1}[D] & [0] \\ [0] & [C_d] - [C_a][M]^{-1}[D] \end{bmatrix} \quad (2.37)$$

$$D_c = \begin{bmatrix} [C_a][M]^{-1}[\bar{B}] & [0] \\ [0] & [0] \end{bmatrix} \quad (2.38)$$

A discrete formulation of the state-space is advantageous, as the measurements are found from a distinct number of samples. The discrete-time stochastic state-space model is presented in Equation (2.39), where  $k$  is the sample number. The state equation is given as:

$$\{s_{k+1}\} = [A]\{s_k\} + \{w_k\} \quad (2.39)$$

The observation equation is then:

$$\{y_k\} = [C]\{s_k\} + \{v_k\} \quad (2.40)$$

In the transfer from a continuous to a deterministic approach, a Zero Order Hold (ZOH) assumption is utilized. The ZOH states that input is piecewise constant over the sampling period. The discrete state-space matrices are equal:

$$[A] = e^{[A_c]\Delta t} \quad (2.41)$$

$$[B] = ([A] - [I])[A_c]^{-1}[B_c] \quad (2.42)$$

$$[C] = [C_c] \quad (2.43)$$

$$[D] = [D_c] \quad (2.44)$$

where  $\Delta t$  is the discrete time step. The stochastic approach is identical to classical discretization, except for the ability to handle noise. The noise represents the two stochastic processes in the problem, and would account for the immeasurable inputs in the OMA context.  $\{w_k\}$  is the process noise and  $\{v_k\}$  is the measurement noise raised from sensor inaccuracies. The input to the system is assumed to possess natural white noise with a zero mean Gaussian distribution. The response in the state-space model can be represented as a zero mean Gaussian process, so that the covariance matrix equals correlation matrix and is given by:

$$[R_i] = E[\{y_{k+i}\}\{y_k\}^T] \quad (2.45)$$

Mathematical manipulations of the state-space equations leads to fundamental relations. Refer to [6] for more details. Factorization of the correlation matrices can be derived:

$$[R_i] = [C][A]^{i-1}[G] \quad (2.46)$$

Where the covariance between the system and the updated state vector is described by:

$$[G] = E[\{s_{k+i}\}\{y_k\}^T] \quad (2.47)$$

The matrix  $[G]$  equals the next state-output covariance matrix. This gives a fundamental relation necessary for the solution of the stochastic subspace identification (SSI) methods.

#### 2.2.4 Rayleigh damping

Rayleigh damping is a method to construct the damping matrix from modal damping ratios and provides an idealized classical damping matrix. Relevant estimates of modal damping ratios can be found in literature from measured data of similar structures.

Rayleigh damping is defined as a linear combination of the mass and stiffness matrix. A linear combination of stiffness proportional and mass proportional damping is given:

$$[C] = a_0[M] + a_1[K] \quad (2.48)$$



Rayleigh damping ratios are defined by the undamped angular eigenfrequencies,  $\omega_i$  and  $\omega_j$ , of the  $i^{th}$  and  $j^{th}$  mode in a MDOF system. The coefficients  $a_0$  and  $a_1$  are defined by Chopra (2012) [12] as:

$$a_0 = \xi \frac{2\omega_i\omega_j}{\omega_i + \omega_j}, \quad a_1 = \xi \frac{2}{\omega_i + \omega_j} \quad (2.49)$$

The damping ratio for the  $n^{th}$  mode is given as:

$$\xi_n = \frac{a_0}{2} \frac{1}{\omega_n} + \frac{a_1}{2} \omega_n \quad (2.50)$$

### 2.2.5 Damping, logarithmic decrement

Damping ratios can be estimated from the response of a structure excited with an impact load. The damping is estimated by the logarithmic decrement which is the natural logarithm of the ratio of two successive peaks [12]. The logarithmic decrement can be obtained for a free vibration time series when damping is present. It can also be determined from the autocorrelation function of a SDOF system, as the envelope depends on the damping alone [14]. It is desirable to define the logarithmic decrement for the  $k^{th}$  extreme, where both peaks and valleys are considered. Hence, the decrement can be defined for slow decays and is more accurate as all maxima can be included. The logarithmic decrement is found from:

$$\delta = \frac{2}{k} \ln \frac{r_1}{|r_{k+1}|} \quad (2.51)$$

Where  $r$  is the value of the peak. When the logarithmic decrement is obtained, the modal damping ratio is given by:

$$\xi = \frac{\delta}{\sqrt{\delta^2 + 4\pi^2}} \quad (2.52)$$

Thus, this provides a way to directly compute the damping. To find the logarithmic decrement in this study, a linear regression of  $k\delta$  and  $2 \ln \frac{r_1}{|r_{k+1}|}$  is used [14].

## 2.3 Signal processing

### 2.3.1 Concepts in signal processing

The signal needs to be adequately sampled in order to capture the analog signal. Lost information is not the only problem that can occur, because a low sampling frequency,  $f_s$ , can cause frequencies to be represented as lower frequency signals due to aliasing. Aliasing occurs when the sampling frequency is too low, and the registered signal is different than the one that actually occurred. Digital sampling cannot capture higher frequencies than the *Nyquist frequency*. The *Nyquist frequency* is equal to  $f_s/2$ , where  $f_s$  is digital sampling rate  $1/\Delta t$  [15]. Figure 2.2 illustrates a cosine curve, of 60 Hz, sampled with a) a sampling rate of twice the signal frequency (*Nyquist frequency*) and b) a sampling rate below the *Nyquist frequency*, which presents a low frequency curve. Digital filters cannot remove the effect of aliasing after the signal has been sampled.

The signal may be resampled in order to achieve a new sampling frequency. Decimation (down-sampling) saves computational time and is used when the signal is sampled with a higher frequency than needed in the analysis. Decimation must be performed with care as aliasing might occur. Thus, any signal above the new *Nyquist frequency* needs to be blocked, which can be performed with a low-pass filter before decimation [6].

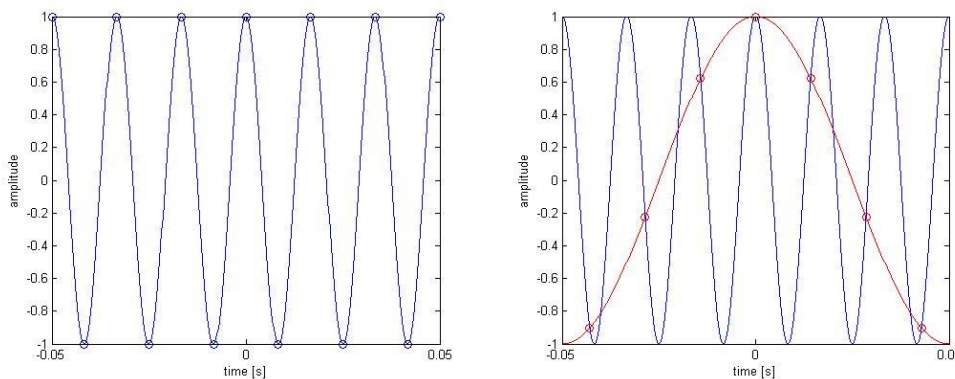


Figure 2.2 a) is sampled with Nyquist frequency = 120 Hz. b) is sampled with 70 Hz and exhibits the effect of aliasing.

### 2.3.2 Fourier transformation

A Fourier transformation transforms a time series into a sum of harmonic oscillations. Hence, the signal can be transformed from the time domain into the frequency domain. This can be performed in both real and complex terms. See Kreyszig [16] for more details. The continuous Fourier transform in complex terms is given by:

$$\hat{f}(\omega) = \frac{1}{\sqrt{2\pi}} \int_{-\infty}^{\infty} f(t) e^{-i\omega t} dt \quad (2.53)$$

And the inverse

$$f(t) = \frac{1}{\sqrt{2\pi}} \int_{-\infty}^{\infty} \hat{f}(\omega) e^{i\omega t} d\omega \quad (2.54)$$

When dealing with samples instead of functions, the Fourier transform is replaced by a discrete Fourier transform (DFT). The signal  $f$  is transformed by a discrete Fourier transform into  $\hat{f}$ .  $\hat{f}$  gives the frequency spectrum of the signal [16].

$$f = [f_0 \cdots f_{N-1}]^T \quad (2.55)$$

$$\hat{f} = [\hat{f}_0 \cdots \hat{f}_{N-1}]^T \quad (2.56)$$

With components

$$\hat{f}_n = \sum_{k=0}^{N-1} f_k e^{-inx_k} \quad (2.57)$$

This requires  $O(N^2)$  operations for every  $n > \frac{N}{2}$  where  $N$  is the number of measurements [16]. Hence, the Fourier transform is a time demanding operation. The fast Fourier transform (FFT) algorithm has been developed in order to reduce the number of operations [6]. It operates by breaking down the operation into smaller problems.  $N$  measurements are divided into  $N = 2^p$  measurements and the method only needs  $O(N) \log_2 N$  operations.

### 2.3.3 Leakage, windowing and zero padding

DFT takes a non-periodic signal and makes it periodic. For a periodic signal, the sampling needs to be done with caution with regard to the wavelength of the signal to avoid discontinuities at the boundary of the observation interval. For a random data series the signal will inherit different properties, and discontinuities at the boundary will occur. The effect of this is large side lobes in the frequency domain, as seen in Figure 2.3. This is called leakage, as the energy at one specific frequency is spread out to the nearby frequencies.

Windows are introduced to reduce the effect of leakage. Smoothing windows will reduce the amplitudes of the time domain data at the beginning and the end of the finite observation

intervals as in Figure 2.3 c). Thus, the periodic extension of the signal would be continuous [17].

A frequency spectrum based on a time series without windowing will have the narrowest central peak, but the leakage is significant [15]. The amount of leakage is reduced as seen in the comparison in Figure 2.3, but a broader central peak is introduced. The main peak has a lower amplitude due to windowing. This is a result of loss of energy due to the envelope created in the windowing process.

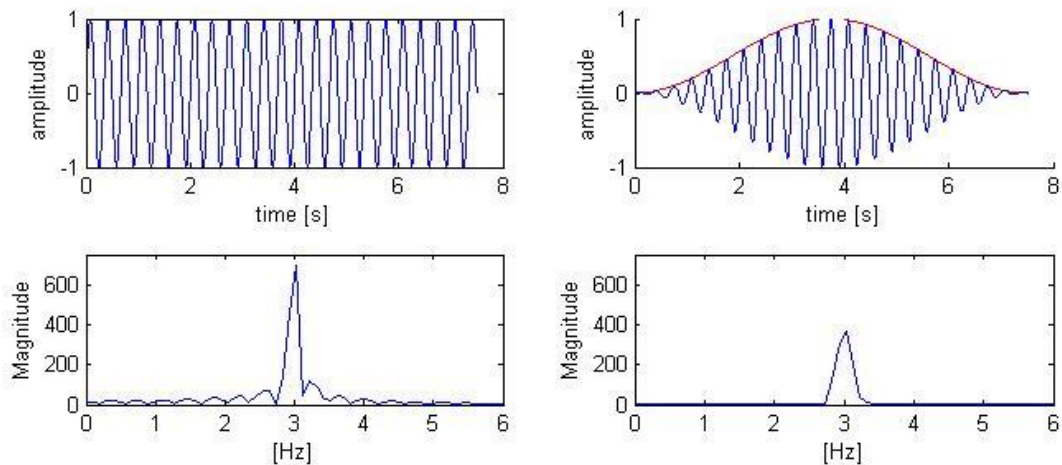


Figure 2.3 A sinus curve with frequency 3 Hz over 7.5 s is plotted in both time and frequency domain. A Hanning window is applied in the right hand plots. The amount of leakage is reduced in the bottom right plot, due to the windowed time series above.

Zero padding is a common technique in a FFT analysis [15]. It is performed by adding a string of zeros to the time domain signal. This provides two effects. Firstly, it is used to run a more efficient FFT algorithm by increasing the sample number to the power of two. Secondly, it carries out an interpolation in the frequency domain and can be seen as a frequency interpolation function. The interpolation occurs when the same frequency range is presented with more sampling points. This does not improve the frequency resolution but can reveal details. E.g. if peaks are split between two bins in the FFT analysis they can be revealed as exemplified in Figure 2.4. The solid curve shows the zero padded data with 4 times as many points as the original data series. The data series contains frequencies of 1 and 1.4 Hz. Here, the zero padding is able to reveal two successive peaks. There are few drawbacks with the method, however, it increases computational cost without actually improving the resolution.

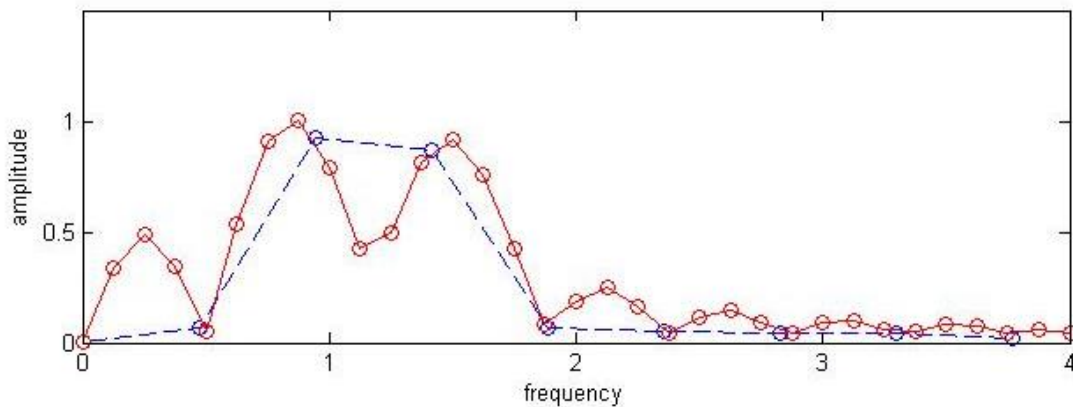


Figure 2.4 The frequency response of two sine curves with amplitude 1 and frequencies 1 Hz and 1.4 Hz are shown in the figure. The solid line is zero padded with four times as many samples as the dotted curve.

### 2.3.4 Welch method

The FFT is a direct computation of the power spectral density (PSD). Different signal processing algorithms can be used to calculate the PSD, in order to reduce the amount of noise and to reduce computational effort. The Welch method is a common procedure and involves sectioning the time series into several overlapping shorter intervals. Each interval is treated with a window in order to limit the discontinuities between the intervals. A FFT is calculated for each windowed segment and the total PSD is an averaged estimated spectra. The averaging reduces the variance of the spectra and the PSD is improved. The noise improvement is illustrated in Figure 2.5. The Welch method requires fewer computations [18] and gives an improved result of the FFT calculations.

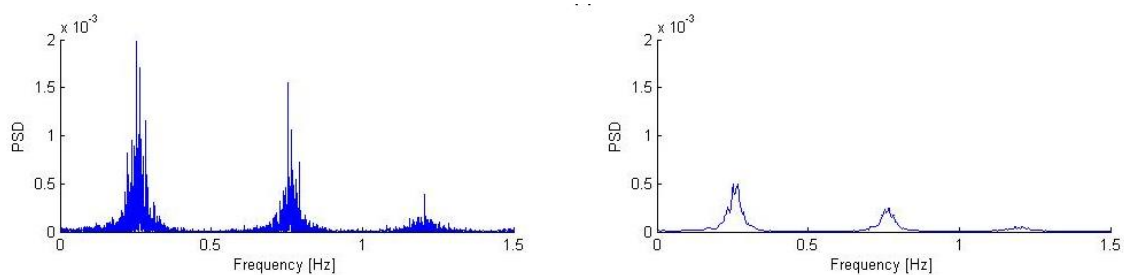


Figure 2.5 The PSD of a one hour long time series, obtained from case study1, is calculated with Welch method. Plot a) is calculated with one windowed segment. In b),  $N$  sampling values is divided into segments with  $K=N/15$  sampling values each with a 50% window overlap.

### 2.3.5 Filters

Digital filters attenuate or enhance certain frequency components from a signal. They are an important part of OMA, as they are efficient for noise removal. Figure 2.6 shows a time series with added white noise compared with the filtered time series. The effect could be

viewed in the frequency domain where frequency above the cut out frequency (10 Hz) is attenuated. Filters can be understood as a transfer function that gives a specified response containing a certain frequency range of the selected input signal. Even though filtering is thought of as a method in the frequency domain, it is implemented in the time domain.

A low-pass filter indicates that the low frequencies will be prevalent in the filtered signal. These frequencies are passed through the passband, while frequencies above the pass-band are attenuated. The converse is a high-pass filter. Band-pass and band-stop filters eliminate certain frequency ranges.

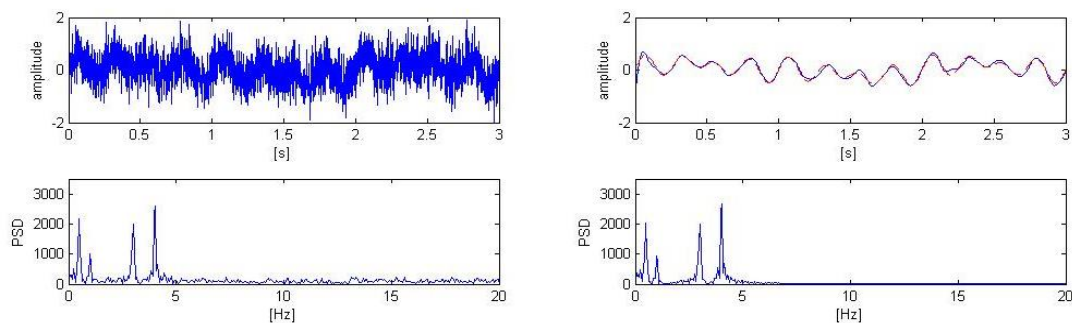


Figure 2.6 Signal with white noise compared with filtered signal (to the right). The noise removal could be viewed in the frequency domain, where frequency above cut out frequency 10 Hz is attenuated. A `filtfilt()` matlab function is used which preserve the phase of the time series.

The signal does not remain unchanged through the filtering process, and the concepts of gain and phase are introduced [19]. The amplitudes of the signal components would be larger or smaller with respect to the filter's transfer function; this characteristic is called gain. The gain is the ratio between the input signal and the filtered output signal with respect to the frequencies. The time of occurrence might be shifted with respect to input signal. This shift between input and output is expressed in relative terms of phase. This study will use designed filters, and further theory of filter design will not be emphasized.

The specification of filtered responses is utilized with various parameters. The cut-off frequency,  $f_c$ , determines where the frequencies are attenuated. Filtering is approximate, and tolerances can be specified in the passband, noted as ripple. The order of the filter determines the steepness of the transition band, which is the area between cut-off frequency and the reject band (see Figure 2.7). The transition band will have a sharper change with a higher order, but needs an infinite order to achieve a true step change. The frequency response is expected to be smooth and discontinuities are not allowed.

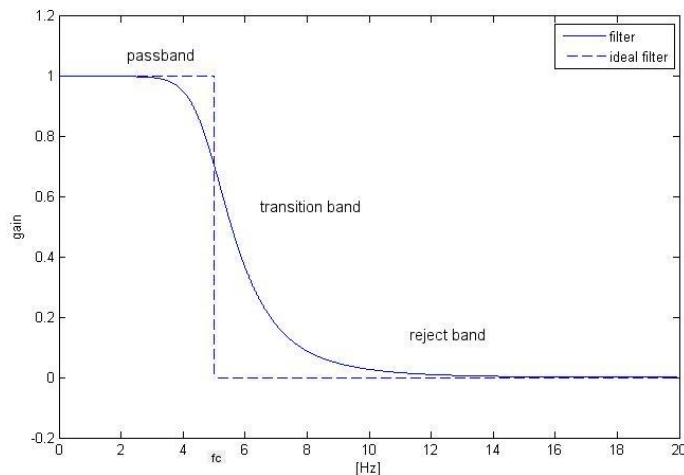


Figure 2.7 Specification of a low-pass filter with ideal and actual response. The transition band, passband, reject band denotes which frequencies are attenuated. The cut-off frequency is 3 Hz with max ripple 3 dB.

### 2.3.6 Butterworth filter

The Butterworth filter can be applied as either low-pass, high-pass or band-pass filter. The flat frequency response in either a passband or a stopband is characteristic for the Butterworth filter [19]. Frequencies in the passband (below the cut-off frequency) can be reduced with a max ripple of  $1/\sqrt{2} = 3 \text{ dB}$ . The gain of a Butterworth filter is given in Equation (2.58). The gain,  $G$ , is a complex function, and thus it inherits both the magnitude and the phase, which are plotted in Figure 2.8. The phase is represented in relative terms and is cyclical over  $2\pi$ . This effect is called wrapping, and is removed with the MATLAB function `unwrap(·)`. The unwrapped phase is plotted in Figure 2.8.

$$|G(\omega)|^2 = \frac{1}{1 + \omega^{2n}} \quad (2.58)$$

$n$  denotes the order of the filter, which determines the steepness of the transition zone.  $\omega$  is here the cutoff frequency, given as normalized frequency  $\times \pi/\text{sample}$ . A Butterworth filter can be created in MATLAB with the function `butter(n, wc)`, where  $n$  is the filter order and  $w_c$  is the normalized cutoff frequency. Butterworth is an Infinite Impulse Response (IIR) filter and has a nonlinear phase [19]. MATLAB gives the option of a zero-phase filtering approach by the `filtfilt(·)` function. It will eliminate the nonlinear phase distortion when applying an IIR filter.

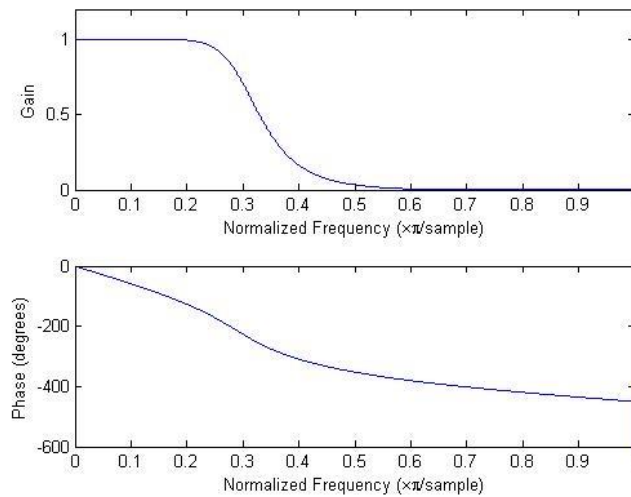


Figure 2.8 The upper graph shows the gain of a Butterworth low pass filter. With a cut frequency of 15 Hz, equal to  $0.3 \times \pi/\text{sample}$ , here with  $f_s=1000$ . The bottom graph shows the phase treated with unwrap.

## 2.4 System Identification methods

System identification methods are used to investigate the system characteristics of a structure. Operational Modal Analysis (OMA) use already existing impacts like ambient forces and operational loads, such as wind, and traffic as system inputs. Fundamental principles and assumptions about the system are required. The system needs to be a linear time-invariant system (LTI). A linear system implies that superposition will be valid and a time-invariant system requires stationarity, where the structural properties are independent of time. The sensor needs to be designed in a way to observe the modes of interest, thus one must have an observable system [6].

The physical process is assumed to be white noise. This is seldom the case for an ambient load input. By investigating both the excitation system and structural system as a combined system, the random load can be considered as an input to the system, as illustrated in Figure 2.9.

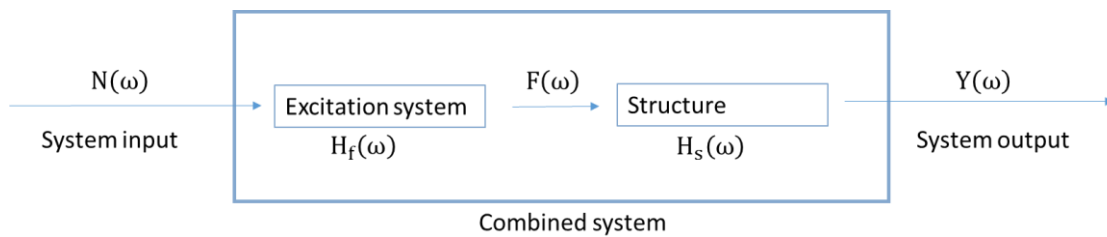


Figure 2.9 A schematic illustration of the combined system with white noise input and the Fourier of the measured response.



The flowchart in Figure 2.9 is given in the frequency domain, to explain the combined model. This is done, even though the investigated methods are in the time-domain. White noise in the frequency domain,  $N(\omega)$ , serve as input to the combined system. The force on the structure from the excitation system,  $F(\omega)$ , is unknown.  $Y(\omega)$  is the FFT of the observed response.  $H_f(\omega)$  and  $H_s(\omega)$  are the frequency response functions of excitation system and structure.

The combined frequency response function,  $H_c(\omega)$ , is given as the product of the excitation system and structural system in the combined system:

$$H_c(\omega) = H_f(\omega)H_s(\omega) \quad (2.59)$$

The unknown force is defined from the white noise input and the transfer function of the excitation system:

$$F(\omega) = H_f(\omega)N(\omega) \quad (2.60)$$

Hence, the combined system response can be described by:

$$Y(\omega) = H_s(\omega)F(\omega) = H_s(\omega)H_f(\omega)N(\omega) \quad (2.61)$$

Which yields:

$$Y(\omega) = H_c(\omega)N(\omega) \quad (2.62)$$

The white noise will, together with an excitation system, provide a given, unknown load on the structure of interest. The output is by definition the response of the combined system. The excitation system is assumed to be a broad-banded process, so that all relevant frequencies are excited and the accuracy is not changed. Due to the excitation transfer function, assumed broad-banded, the investigated structural characteristics will be from the structural system. Variance plays a fundamental role in the investigation. The input is considered uncorrelated by the white noise assumption. Hence, the covariance holds the physical information about the structural system only.

OMA methods are divided into different classes. Methods where a model is fitted to the data are denoted parametric methods with the converse being non-parametric methods. Parametric methods often define a model order to the dataset of interest. This will often require a stabilization diagram. Parametric methods are divided into low order methods, which imply that the physical coordinates are larger than the obtained eigenvalues, and high order models, which denote an under-sampled system. Another distinction is made between

SDOF and MDOF models, and - indicates if one or more modes determine the structural response. SDOF assumption can be used if the modes are well separated. The methods that calculate all modal parameters in one step are called one-step methods. Likewise, two stage methods calculate one set of parameters first, and the other modal parameters are estimated based on the data found in step one. Methods are also classified by the domain of implementation, and are either time domain methods or frequency domain methods. This provides differences with regard to noise rejection and the quality of numerical conditioning. Analyses of time histories or correlation functions are denoted as time domain methods and frequency methods are based on spectral density calculations.

### 2.4.1 Second Order Blind Identification method

The Second Order Blind Identification (SOBI) method is a non-parametric system identification method in the time domain. The procedure is outlined in the following flowchart:

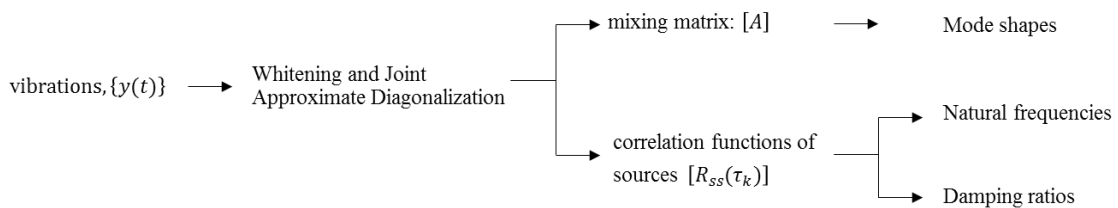


Figure 2.10 Flow chart of Second-Order Blind Identification

Different sensors measure vibrations created by a structure under ambient vibrations. These measurements can be regarded as a sum of original sources multiplied by an unknown matrix. The linear and static mixture of sources can be given as [20]:

$$\{y(t)\} = [A]\{s(t)\} + \{n(t)\} \quad (2.63)$$

$\{y(t)\}$  is defined as the mixture of the real sources  $\{s(t)\}$ .  $[A]$  is the unknown nonsingular mixing matrix.  $\{n(t)\}$  is assumed to be sensor noise. The linear mixture  $[A]\{s(t)\}$  could be seen as a modal extension problem given in Equation (2.22), repeated for convenience:

$$\{y(t)\} = \sum_{n=1}^{\infty} \{\phi_n\} q_n(t) = [\phi]\{q(t)\} \quad (2.64)$$

The matrix  $[A]$  can be set equal to the mode shape matrix  $[\phi]$ , and where the sources can be physically interpreted as the modal coordinates. The column of the modal matrix consists of orthogonal mode shapes, which are obtainable if the mixing matrix is found. The method

separates the different modal coordinates that provide virtual sources with different spectral contents [21].

The SOBI method identifies the unobserved sources by analyzing the linear mixtures from the observed signal. Based on source separation techniques, the mixing matrix  $[A]$  in Equation (2.63) is identified through the observed time series and assumptions of its correlations and noise properties. As the noise input into the system is assumed to be white noise, the correlation can be observed from the investigated system alone.

SOBI is a two stage method. Firstly, the mode shapes are found through the mixing matrix. The natural frequencies and damping ratios are found in the second stage. Since the signals are separated into different sources, which are assumed to be mutually uncorrelated and temporally correlated, the frequencies and damping ratios can be found from SDOF methods of the sources correlation functions.

The method can handle different mixes of sources, both linear and non-linear. From a time-domain perspective it is natural to assume convolutive mixing, where the observed signal is regarded as a convolution product of the impulse response function and external force vector[21]. The extraction of sources from convolutive mixtures is not completely solved [6] and only static mixtures of sources are outlined in this section.

One drawback of the method is the limited ability to handle complex modes. The mixing matrix is a real valued matrix. Thus, real valued mode shapes are presented and the method is inherently limited to weakly damped systems.[22] The Blind Modal Identification (BMID) algorithm by McNeill and Zimmerman presents a solution to this problem [23]. Another limitation of SOBI is that the method requires the number of sensors to be larger than the number of active modes. Equation (2.63) shows the  $l$  dimensional vector  $\{y(t)\}$  and mixing matrix with dimensions  $l \times N_m$ .  $N_m$  is the number of columns equal to the number of active modes and sources. In order to identify the  $N_m$  modes,  $rank([A])$  must be at least  $N_m$ . Hence, the number of time histories  $\{y(t)\}$  needs to be  $l \geq Nm$ . The problem can be overcome by applying a passband filter so that only a limited range of frequencies is considered in one step. This method is only able to identify distinct modes, thus source signals must have different spectral shapes. Repeated modes are difficult to obtain by the SOBI method [22].

The assumptions for this method related to sources and noise properties are presented in the following equations. The sources are assumed to be mutually uncorrelated, stationary and scaled to have unit variance. The covariance matrix should equal the identity matrix:

$$[R_{ss}(0)] = E\{\{s(t)\}\{s(t)\}^T\} = [I] \quad (2.65)$$

where  $\{s(t)\}$  is a  $N_m$  dimensional source vector at time instant  $t$ .

The sensor noise is assumed to be a temporally and spatially white, stationary, and random process with the following properties:

$$E\{\{n(t)\}\} = \{0\} \quad (2.66)$$

$$[R_{nn}(0)] = E\{\{n(t)\}\{n(t)\}^T\} = \sigma^2[I] \quad (2.67)$$

The noise should be independent of the source signals:

$$E\{\{n(t)\}\{s(t)\}^T\} = [0] \quad (2.68)$$

The observed data should be detrended to obtain a mean equal to zero. A zero mean is therefore assumed in the following derivations, which forces the covariance and correlation to be equal. Therefore they will not be distinguished in the following section.

A step-by-step explanation of the method will be provided. The SOBI method starts with defining a whitening matrix to apply to the signal part  $\{x(t)\} = [A]\{s(t)\}$  so that the achieved data are uncorrelated and have a unit variance. The whitened observed data  $z$  is given as:

$$\{z(t)\} = [W]\{x(t)\} \Rightarrow [R_{zz}(0)] = E\{\{z(t)\}\{z(t)\}^T\} = [I] \quad (2.69)$$

Combining Equation (2.69) and (2.65) in (2.70), it is seen that  $[W][A]$  creates a unitary matrix, hereafter noted as  $[A']$ . A unitary matrix gives the identity matrix when multiplied with its own transpose. Hence, the mixing matrix can be factored as a product of the inverse whitening matrix and the unitary matrix  $[A']$ .

$$[R_{zz}(0)] = [W][A]E\{\{s(t)\}\{s(t)\}^T\}[A]^T[W]^T = [W][A][A]^T[W]^T = [I] \quad (2.70)$$

Two different approaches of defining the whitening matrix will be investigated. The first method, classical whitening, is covered by Belouchrain (1997) [20]. The whitening matrix obeys a linear model given as

$$[W]\{y(t)\} = [W]([A]\{s(t)\} + \{n(t)\}) = [A']\{s(t)\} + [W]\{n(t)\} \quad (2.71)$$

The signal part is now a unitary mixture of source signals. This is advantageous since changing  $[A']$  to any other unitary matrix will give an unchanged covariance of  $z(t)$  [20]. The covariance of the observed mixture is,

$$[R_{yy}(0)] = E\{\{y(t)\}\{y(t)\}^T\} = [A][A]^T + \sigma^2[I] \quad (2.72)$$

The following relation can be seen

$$[A][A]^T = [R_{yy}(0)] - \sigma^2[I] \quad (2.73)$$

If the noise covariance can be estimated, it can be shown that the whitening matrix can be estimated. Firstly, the eigenvalue decomposition of  $y$  is performed

$$[R_{yy}(0)] = [V][D][V]^T \quad (2.74)$$

Where  $[V]$  is an orthogonal eigenvector matrix, and  $[D]$  is the diagonal eigenvalue matrix. The  $(l - N_m)$  smallest eigenvalues are chosen to be regarded as noise. The variance of the noise, noted as  $\sigma^2$  (2.67) is calculated as the average of  $(l - N_m)$  eigenvalues.  $[D]$  is an eigenvalue matrix with the  $N_m$  largest eigenvalues. An estimate of the whitening matrix is calculated as:

$$[W] = ([D_{N_m}] - \sigma^2[I_{N_m}])^{-\frac{1}{2}}[V_{N_m}]^T \quad (2.75)$$

The second way of determining the whitening matrix is called the robust whitening procedure [24]. The assumption in Equation (2.67) is omitted and there is no assumption about the noise distribution or spatial correlation properties. The noise is assumed to be temporally white. The assumption in Equation (2.67) will be replaced with:

$$E\{\{n(t)\}\{n(t)\}^T\} = [R_{nn}] \quad (2.76)$$

Where  $[R_{nn}]$  is considered unknown. The robust whitening method performs an eigenvalue decomposition of the linear combination of correlation matrices of different time-lags. The correlation matrices must be positive definite and the lag should be nonzero. The correlation matrices are gathered in an  $l \times K$  matrix set, where  $l$  is the number of observed time series and  $K$  the number of time steps:

$$[R] = [\hat{R}_y(1) \dots \hat{R}_y(K)] \quad (2.77)$$

A singular value decomposition (SVD) of  $[R]$  is performed

$$[R] = [E_R][\Sigma][V]^T \quad (2.78)$$

To define the contribution factor,  $\alpha_i$ , which gives the contribution from the correlation matrices of a specific time-lag, a final-step global convergence algorithm is introduced in Equation (2.80) - (2.81) [24]. This algorithm will secure a positive definite combination. The factor  $[F]$  is computed:

$$[F_i] = [E_R^T][\hat{R}_y(i)][E_R]^T \quad (2.79)$$

$$[F] = \sum_{i=1}^K \alpha_i [F_i] \quad (2.80)$$

The smallest eigenvector of  $F$  is noted as  $E_F$  and should be used to update  $\alpha$  by defining  $d$  as:

$$d = \frac{[[E_F^T][F_1][E_F] + \dots + [E_F^T][F_K][E_F]]^T}{\|[[E_F^T][F_1][E_F] + \dots + [E_F^T][F_K][E_F]]\|} \quad (2.81)$$

The contribution factor,  $\alpha$ , is updated with  $\alpha_i = d + \alpha$ , and is inserted in Equation (2.80). If  $F$  is not positive definite, another update of  $\alpha$  by Equation (2.81) will be performed. If  $F$  is positive definite the linear combination of correlation matrices with contribution factor  $\alpha_i$  is given as:

$$[C] = \sum_{i=1}^K \alpha_i [\hat{R}_y(i)] \quad (2.82)$$

$[\hat{R}_y(i)]$  is the correlation matrix for time-lag  $i$ . An eigenvalue decomposition is performed on the linear combination matrix:

$$[C] = [V_c][D_c][V_c]^T \quad (2.83)$$

The whitening matrix defined by robust whitening is given as

$$[W] = ([D_c])^{-\frac{1}{2}}[V_c]^T \quad (2.84)$$

And the whitened correlation matrix becomes

$$[\hat{R}_y(i)] = [W][\hat{R}_y(i)][W]^T \quad (2.85)$$

After the whitening matrix is established from classical or robust whitening, the whitened correlation matrices for a series of time-lags are calculated.

$$[R_{zz}(\tau_i)] \quad i = 1, 2, \dots, K \quad (2.86)$$

Number of time lags  $K$  should be set to achieve a ratio of 10% between the first and last cycle for source correlation of the fundamental mode [22].

A unitary matrix,  $[\tilde{A}]$ , that minimizes the sum of off-diagonal terms of the shifted covariance matrix  $[R_{zz}(\tau_i)]$ . of  $\{z(t)\}$ . The joint diagonalization is performed with a numerical algorithm called the joint approximate diagonalization (JAD) technique, which is an extension of the Jacobi technique that finds a unitary diagonalizer as a product of the Givens rotation. An extended explanation can be found in reference [25].

The optimization problem is defined as:

$$\min_{[\Psi]} \sum_{i=1}^K \text{off}([\tilde{A}]^T [R_{zz}(\tau_i)] [\tilde{A}]) \quad (2.87)$$

The optimization problem is solved by the JAD technique. A threshold value,  $t$ , is set to stop the JAD iteration. By Rainier [22] it is shown that  $t$  can be assumed to be  $10^{-8}$ , and reducing  $t$  any further provides a negligible effect.

The mixing matrix  $[A]$  is then easily obtained as

$$[A] = [W]^+ [\tilde{A}] \quad (2.88)$$

The demixing matrix  $U$  is defined as

$$[U] = [\tilde{A}]^T [W] \quad (2.89)$$

And the source signal will be estimated from the demixing matrix as

$$\hat{s}(t) = [\tilde{A}]^T [W] x(t) = [U] x(t) \quad (2.90)$$

$[W]^+$  Implies the Moore-Penrose pseudoinverse.  $[R_{zz}(\tau_i)]$  is provided in the JAD function, as seen in Equation (2.87), and will be nearly shift-uncorrelated as the matrices are nearly diagonal:

$$[R_{ss}(\tau_k)] = [\tilde{A}]^T [W] E(y(t)y(t + \tau)^T) [W]^T [\tilde{A}] \quad (2.91)$$

$$= [\tilde{A}]^T [R_{zz}(\tau_k)] [\tilde{A}] = [U][R_{yy}][U]^T$$

The mode shapes are found directly from the columns of  $[A]$ . The columns will correspond to the numbered sources. Since the sources are independent, SDOF methods can be used.

The eigenfrequencies can be obtained from zero crossings of the independent sources or their correlation functions. However, damping is only estimated by the correlation function. Information from the random excitation is necessary if damping ratios are to be investigated from the time series of the sources [22].

The autocorrelation function of the displacement is related to the autocorrelation of the modal coordinate as derived in Section 2.2.2.

## 2.4.2 Stochastic Subspace Identification

Stochastic Subspace Identification (SSI) methods are output-only methods classified as parametric time domain methods. Within the field of system identification, SSI methods are considered to be among the most stable and reliable methods [6].

A real structure is characterized by an infinite number of DOFs, but this is shortened to a few dozen in a practical context. A stochastic state-space model search is performed to determine the order of the system and to determine the state-space matrices, as defined in section 2.2.3. The stochastic realization problem is defined as the method of identifying a stochastic state-space model from output-only data [6].

The estimation of state-space matrices can be done through different approaches, including partitioning as a covariance-driven SSI method and the data-driven SSI method. The former establishes the state-space matrices through preprocessing, including the establishment of covariance matrices. The latter establishes the state-space matrices directly from the raw data.

The covariance-driven stochastic subspace identification method is carried out in this study and the basic concepts will be explained in the following section. This method is chosen due to its ability to establish the variances of the identified system parameters.

### 2.4.2.1 Covariance-driven Stochastic Subspace Identification

To construct a state-space model, the system needs to be capable of establishing an observable and controllable part. The system is considered observable if it is possible to determine the state from the output, given that the state-space matrices are known. The



system is controllable if a state  $s_k$  at instant  $k$  can be reached from any initial state by some control actions. The model order  $n$  is the number of state variables, which should contain enough information to describe the system. Hence, the observability and controllability matrices need to be of rank  $n$  in order for the method to work. The order of the system  $n$  is most likely unknown. Thus, a conservative approach is to overestimate the order of the system. As a result of overestimating the order, the method will produce both physical and nonphysical poles, and the nonphysical poles need to be separated from the physical ones at a later stage in the method.

The main steps in the method are introduced in the following section, and explained more thoroughly by Rainieri et al. [6]. The output correlation matrices should be calculated from the  $l \times N$  data matrix,  $[Y]$ , containing  $N$  data samples from  $l$  observed data signals. The matrix  $[\bar{R}_i]$  denotes the unbiased estimate from time-lag  $i$ .

$$[\bar{R}_i] = \frac{1}{N-i} [Y_{(1:N-i)}][Y_{(i:N-i)}]^T \quad (2.92)$$

The output correlation matrix is stored in a block Toeplitz matrix, Equation (2.93).

$$[T_{1|i}] = \begin{bmatrix} [\hat{R}_i] & [\hat{R}_{i-1}] & \cdots & [\hat{R}_1] \\ [\hat{R}_{i+1}] & [\hat{R}_i] & \cdots & [\hat{R}_2] \\ \vdots & \vdots & \ddots & \vdots \\ [\hat{R}_{2i-1}] & [\hat{R}_{2i-2}] & \cdots & [\hat{R}_i] \end{bmatrix} \quad (2.93)$$

The block Toeplitz matrix will take on dimensions  $li \times li$ , where  $i$  is the number of time-lags. The requirement in this step is  $li > n$ , where  $n$  is the order of the system. The order of the system can be overestimated and the number of necessary time-lags  $i$  is therefore given by

$$i > n/l. \quad (2.94)$$

The number of singular values from the PSD matrix, or the number of peaks in the power spectra in the frequency domain, serves as an estimate of the system order. The order of the system is the only parameter used to fit the method to the model.

The correlation matrices describe the statistical properties of the system. Fundamental relations between the state-space equation and the statistical relations are given in section 2.2.3 and the state-space matrices might be estimated by decomposition of the covariance matrices. The Toeplitz matrix is factored according to Equation (2.46). The observability matrix  $[O_i]$  and reversed controllability matrix  $[\Gamma_i]$  is derived from this factorization as

$$[T_{1|i}] = \begin{bmatrix} [C] \\ [C][A] \\ \vdots \\ [C][A]^{i-1} \end{bmatrix} [[A]^{i-1}[G] \quad \dots \quad [A][G] \quad [G]] = [O_i][\Gamma_i] \quad (2.95)$$

Matrix  $[C]$  is the discrete-time output matrix,  $[A]$  equals the discrete-time state matrix and  $[G]$  is the next state-output covariance matrix. An SVD of the block Toeplitz matrix provides the rank, which equals the number of nonzero values. The rank will theoretically equal  $n$  if the system is both observable and controllable. The zero singular values and their corresponding eigenvalue vectors are omitted, and the decomposition of the Toeplitz matrix is given as

$$[T_{1|i}] = [U_1][\Sigma_1][V_1]^T = [O_i][\Gamma_i] \quad (2.96)$$

Where  $[U_1]$  is the matrix of left singular vectors corresponding to nonzero values,  $[\Sigma_1]$  holds the nonzero values, and  $[V_1]$  is the matrix of the right singular values. The SVD is then split into two parts by a non-singular square matrix  $[T]$ :

$$[O_i] = [U_1][\Sigma_1]^{1/2}[T] \quad (2.97)$$

$$[T_i] = [T]^{-1}[\Sigma_1]^{1/2}[V_1]^T \quad (2.98)$$

It can be shown that if  $[T]$  is a non-singular square matrix, this provides a similarity transformation explained in the reference [6].  $[T]$  can be chosen as the identity matrix.

The output influence matrix and the next state output covariance matrix can be obtained from the observability and controllability matrices, comparing Equations (2.47), (2.97), and (2.98). By creating a one lag shifted Toeplitz matrix, the state matrix  $[A]$  can be found from the decomposition as

$$[T_{2|i}] = [O_i][A][\Gamma_i] \quad (2.99)$$

Introducing Equation (2.97) and (2.98) into (2.99), gives the following equation for the state matrix:

$$[A] = [O_i]^+[T_{2|i}][\Gamma_i]^+ = [\Sigma_1]^{-1/2}[U_1]^T[T_{2|i}][V_1][\Sigma_1]^{-1/2} \quad (2.100)$$

$[ ]^+$  denotes the pseudoinverse. Other approaches to determine the state matrix are found in [6].

The eigenvalues of the state matrix  $[A]$  denote the poles. This needs to be converted into continuous time as given in Equation (2.41). Thereafter, properties can be determined from the physical poles. The natural frequency, damped modal frequencies and damping ratios are estimated from the poles  $\lambda_r$  according to Equations (2.19), (2.20), and (2.21). Couples with frequencies that are multiples of  $(2\pi / \Delta t)$  are indistinguishable. Thus,  $\Delta t$  must be chosen carefully and must be sufficiently short to prevent frequencies beyond the Nyquist frequency to be observed at lower frequencies in the realization.

The output correlation and the identified state space matrices are all estimates. Errors in the estimates arise due to different noise sources such as [6]:

1. Modelling inaccuracies if the system does not fit the stochastic state-space model
2. Measurement noise due to the measurement equipment
3. Computational noise raised from precision problems
4. Use of a finite number of data points, hence the output correlations are not exact.

Consequently, the factorization properties of the Toeplitz matrix do not hold, as the output correlations are not exact. Due to the noise, the order number of nonzero singular values does not correspond to the order  $n$  of the system. The smallest singular values can be removed due to noise. Hence, the gap between two subsequent singular values might give a prediction of the model order. Modal parameters are calculated for an increasing model order  $n$ , and plotted in a stabilization diagram, where the spurious modes are separated from the physical ones. See section 2.4.3 for the properties of the stabilization diagram.

One benefit of cov-SSI is the ability to assess the quality of the identified state-space model and the uncertainty of the estimated parameters. This is achieved by comparing the synthesized spectra from the identified state-space model with those estimated from the measurements. The spectra is derived by Peeters (2000) [26].

### 2.4.3 Quality check and comparison

If different OMA methods are performed, comparison can be used to check consistency of the obtained modal parameters. Normal approaches are presented by Rainier [6], and will be used in the investigation of modal properties. Relative scatter between natural frequencies obtained from different models or between estimated and analytical parameters can be compared and expressed in a percent as,

$$\Delta f_n = 100 \frac{f_{2,n} - f_{1,n}}{f_{1,n}} \quad (2.101)$$

where  $n$  denotes the  $n^{th}$  mode of comparison and index 1 and 2 denote the different models or analysis results under comparison.

The consistency between models can also be presented in a scatter plot. Values from the first set of analyses are on the horizontal axis and the second set under comparison is on the vertical axis. A trendline can be drawn and a line going through the origin with a slope of  $45^\circ$  demonstrates good correlation. It is important to check information about the modes so that the corresponding frequencies are compared.

The modes shape correlations can be investigated by graphical representation as scatter plots, as explained above, or by comparing MAC values. MAC value is a squared, linear regression correlation coefficient. It measures the degree of linearity between two vectors and is computed as [6]:

$$MAC(\{\phi_n^1\}, \{\phi_n^2\}) = \frac{|\{\phi_n^1\}^T \{\phi_n^2\}|^2}{(\{\phi_n^1\}^T \{\phi_n^1\})(\{\phi_n^2\}^T \{\phi_n^2\})} \quad (2.102)$$

Where 1 and 2 denote the different methods for comparison of the  $n$ 'th mode. This provides an estimate of the consistency, but does not ensure validity. A MAC value of 1 indicates full correlation. MAC values from two different models can be presented in a CrossMAC matrix. It is a MAC matrix but it consists of modes from two different sets of estimated mode shapes. It will have a unit value at the diagonal and zero elsewhere if the mode shape estimates are consistent.

The sensor layout is important in an OMA in order to observe the correct modes. The performance with identifying modes can be investigated by an AutoMAC matrix. This is a matrix consisting of the mode shapes from one OMA method. The diagonal will be unity. If off-diagonal terms are close to zero, the obtained modes can be regarded as independent of each other. If the off-diagonal terms are large, further investigation should be performed. It might indicate that repeated modes are found for distinct frequencies. This could also be due to orthogonality, spatial aliasing, or spurious modes that are included in the obtained modes. Spatial aliasing is the counterpart of time aliasing and occurs when the number of sensors is too small to measure the correct shapes and occurs if the wave number of one mode exceeds the number of sensors regularly spaced in that direction. The aliased mode shape will be repeated as a mode with a lower wave number.

---

The modal complexity contains valuable information needed to validate the result. Complex modes originate from several sources, including gyroscopic effects, aerodynamic effects, nonlinearities and non-proportional damping [2]. So, in some cases, more or less complex modes are expected. However, when normal modes are expected the complexity can be an important part of validating the results. As complex modes often occur due to poor signal-to-noise ratio, this can be used to distinguish between physical and spurious modes. The degree of complexity can be investigated visually in a complexity plot. A few indexes that provide a quantitative measure of the degree of complexity are presented in the following section. They will later be utilized in the process of picking modes in the stabilization diagram.

Modal Phase Collinearity (MPC) is an index that assesses modal shape complexity. It takes on the value 1 for mode shapes with a phase equal to  $180^\circ$  or  $0^\circ$  which indicates a normal (real) mode. A MPC value of 1 is therefore sought after when expecting normal modes, whereas a low MPC value can indicate a non-structural mode. The detailed calculations can be found in reference [6]. For a normal (real) mode shape, both MPD and Mean Phase ought to be close to zero.

Stabilization diagrams are a common practice for the parametric method, and can determine which system order the modal parameter should be estimated from. The diagram itself does not solve for modal parameters, but is a helpful graphical tool to separate physical modes from spurious ones. Modal parameters are calculated for an increasing model order  $n$ . The spurious ones occur from noise modes due to system excitation and because of overestimation. If white noise is present, the poles are different from the system poles. However, when coloured noise is present, the modes can look quite similar to the physical ones [27]. Typical indications of spurious modes are high damping ratios or unrealistic mode shapes.

For state space models, eigenvalues corresponding to system poles for different system orders are found. Poles are given in complex conjugate pairs, refer to Section 2.2.1. As only poles with positive imaginary components give positive damping, they are the only poles that are plotted. The state-space model only provides half the order of modal parameters. True poles are detected by comparing modes from different orders  $n$ . Modal parameters can be chosen from the alignment of stable modes.

Stable modes are defined by following criteria [6]:

---

$$\frac{|f_n(n) - f_n(n+1)|}{f_n(n)} < \textit{stability requirement} \quad (2.103)$$

$$\frac{|\xi(n) - \xi(n+1)|}{\xi(n)} < \textit{stability requirement} \quad (2.104)$$

$$[1 - \textit{MAC}\{\phi(n)\}\{\phi(n+1)\}] < \textit{stability requirement} \quad (2.105)$$

For frequency  $f_n$ , damping  $\xi$  and MAC values of the mode shape for each order  $n$ .

## Chapter 3      Method

Two case studies are presented in the method chapter. Firstly, a benchmark example is established in order to check accuracy of the implemented SOBI method. Both results and description are provided in case study 1. In Case study 2, the data obtained from Dolmsundet Bridge during construction is investigated. The result from this case is provided in the following chapter.

### 3.1 Implementation of system identification method

The SOBI method is implemented in MATLAB, based on the theory described in section 3.3.7, patterned after reference [22]. Different ways of establishing the whitening matrix were investigated. Robust whitening was preferred as whitening method as it does not require spatial white noise. Some errors occurred in the implementation of robust whitening, and the implementation was replaced by the with classical whitening method. The method is limited to handle non-complex modes.

The SOBI method does not provide any statistical parameters of accuracy as in the cov-SSI method. Hence, checking assumption validity and comparing graphical outputs is important in order to control the quality of the results.

### 3.2 Case study I –Implementation of SOBI on a shear frame

In order to investigate the implemented SOBI method, a simplified shear frame is studied. The load is modelled as Gaussian white noise and applied in the systems DOFs. The noise is generated by the random number generation function in MATLAB, *randn()*. Rayleigh damping is used for applying damping ratios, defined in Equation (2.48)-(2.50). The simulated response are calculated numerically with Newmark's method, with constant acceleration properties. This analytical response is used as the vibration input to the implemented SOBI method.

Two different shear frames are generated in case study 1. Firstly, system 1 is generated in order to implement and give an overview of the performance of the SOBI method. System 2

is analyzed in order to check the methods performance with closely spaced modes. The impact of varying damping ratios and time series duration are investigated for system 1 and presented in the case study 1 results. The modes are compared with analytical values, hence, the accuracy is investigated.

### 3.2.1 Properties of 5DOF shear frame

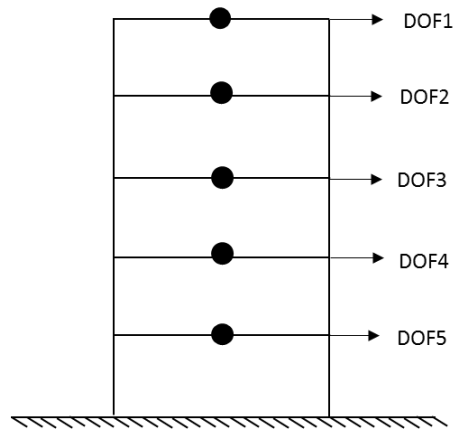


Figure 3.1 Illustration of MDOF shear frame and numbering of DOFs.

The system is applied Rayleigh damping, which is proportional damping. The system's modal parameters are solved analytically by the complex eigenvalue solution, section 2.2.1. Analytical results are viewed in Table 3-1, where the damping variations of system 1 are included.

Table 3-1 Properties of system 1 and 2, Case Study 1

Mode	System 1					System 2	
	$f_n$ [Hz]	$\xi_a$	$\xi_b$	$\xi_c$	$\xi_d$	$f_n$ [Hz]	$\xi_a$
1	0.2615	0.05	0.0	0.10	0.20	0.109	0.05
2	0.7634	0.03	0.0	0.07	0.14	0.3092	0.03
3	1.2035	0.04	0.0	0.08	0.16	0.4991	0.04
4	1.546	0.05	0.0	0.09	0.18	0.7399	0.05
5	1.7633	0.05	0.0	0.10	0.20	0.7517	0.05

### 3.2.2 Method

The method is explained by analysis performed on System 1 with damping ratios case a, and a signal length 60 minutes. The simulated response was resampled from 100 Hz to 20 Hz and a low-pass Butterworth filter of order 6 and cut-off frequency 2 Hz was applied. The preprocessing is explained more throughout in the theory section 2.3. The low pass-band filter is applied close to the desired frequencies as mode 5 was hard to excite, and it was necessary to remove noise in order to identify this mode.



The new time series  $\{z(t)\} = [W]\{x(t)\}$  is obtained by linear transformation of  $\{x(t)\}$  with the whitening matrix. The correlation  $R_{zz}$  is checked to take form as the identity matrix, which denotes uncorrelated data.

The MATLAB code for JAD is provided by Jean-Francois Cardoso and is available online [28], explained in reference [25]. This code solves the optimization problem in Equation (2.87) and provides a unitary matrix, which the sources and mixing matrix can be calculated from.

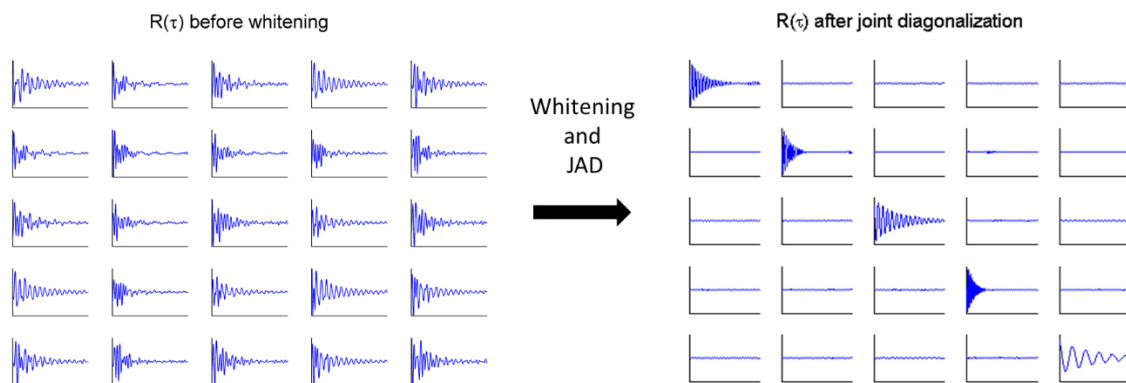


Figure 3.2 a-b) Illustration of correlation matrix before and after applied whitening and JAD.

Figure 3.2 a) represents the correlation of the observed signal, whereas part b) gives the correlation of the separated sources. The diagonal represents autocorrelation of the signal and the off-diagonal represents the cross-correlation, both with respect to time-lags. This illustrates how the signals are separated into spatial uncorrelated sources, and is helpful in order to see if the method was able to separate the sources.

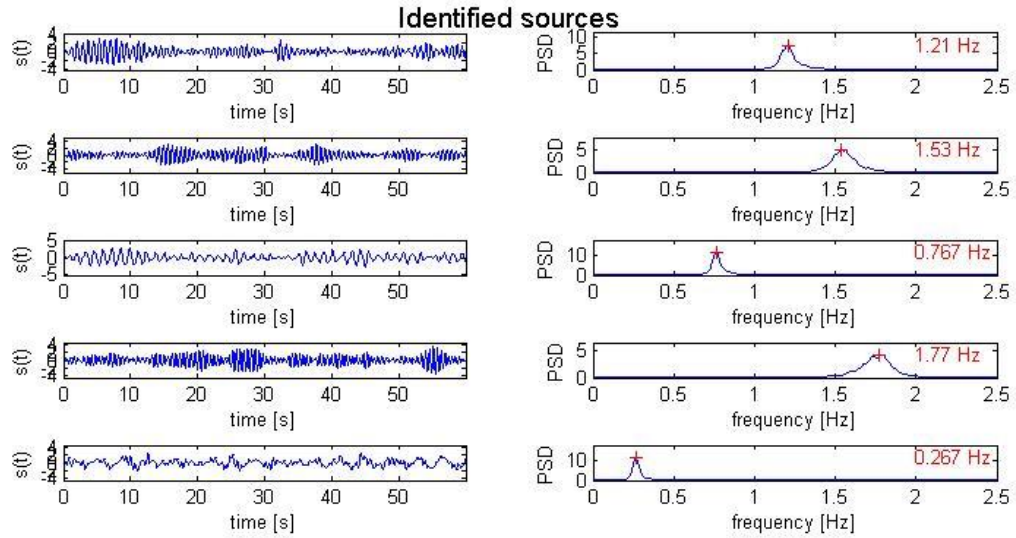


Figure 3.3 Sources, shown for the 60 first second, is shown to the left. PSD of sources are shown to the right with corresponding peak value.

The sources are provided in Figure 3.3, showing with time series of the first 60 seconds and a PSD plot. The PSD shows a narrow banded process. This is in accordance with the comparison of a damped SDOF system loaded with white noise. As the system is loaded with white noise, the sources will inherit several frequencies close to their eigenfrequencies. Damping ratios would not be possible to identify from the sources' time series as the system is excited with random excitation [22]. Peak picking of the PSD shows approximate estimates of the damped eigenfrequencies. The decay of a SDOF systems' correlation function will provide the damping ratio. Hence, it is not necessary to compute the sources separately, as the sources' correlation functions are provided from the joint diagonalization. The number of time-lags is crucial when modal parameters are derived from the correlation functions. The number of time-lags is set such that a ratio equal to 10 % of the last and first peak in the fundamental mode is obtained, as recommended by Rainieri (2014) [22].

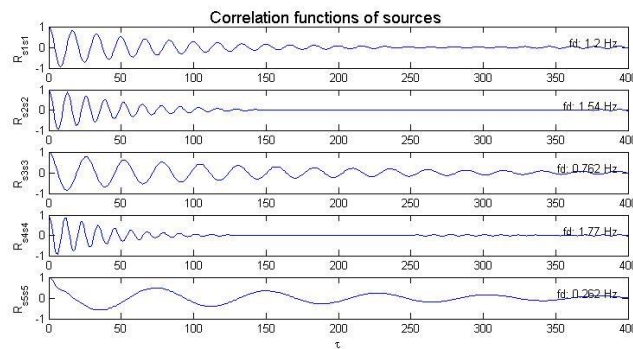


Figure 3.4 Correlation of sources, given with damped frequencies,  $f_d$ .

Figure 3.4 shows correlation functions with estimated damped frequencies. Frequencies are then found by zero-crossings of the correlation functions of the independent sources, and damping ratios are calculated from the decay. The logarithmic decrement can be calculated with a various numbers of maxima, given by Equation (2.51). Linear regression on  $k\delta_j$  and  $2\ln(\frac{r_0}{r_k})$  is used to find an estimated value of the logarithmic decrement, where  $k$  is the number of maximas included. The value of  $k$  is selected depending on the best linear fit. This is illustrated in Figure 3.5. The  $k$  peaks included are marked with the solid line. Damping ratios are then defined after Equation (2.52).

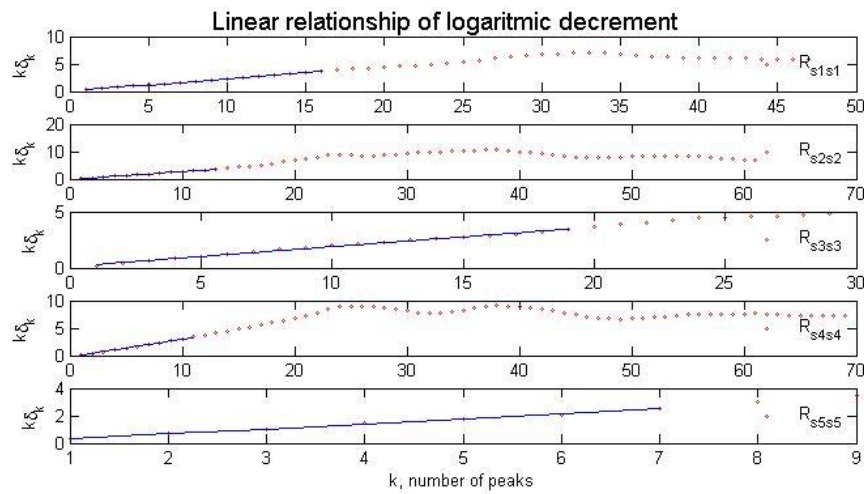


Figure 3.5 The slope of the linear curve gives an estimated value of the logarithmic decrement.

### 3.2.3 Result and considerations

Relative deviances from analytical values are shown in Table 3-2 and Table 3-3. MAC values are used to estimate the correlation between analytical solved modes and the ones obtained from the mixing matrix A.

Table 3-2 Result, system 1a.

System 1a					
Mode	Analytical $f_n$	$\Delta f_n$ [%]	$\Delta \xi_n$ [%]	MAC	Corresponding source
1	0.262	0.306	14.7	1.00	5
2	0.763	0.121	18.2	1.00	3
3	1.20	0.518	9.64	1.00	1
4	1.55	0.155	0.704	0.99	2
5	1.76	0.343	2.71	0.99	4

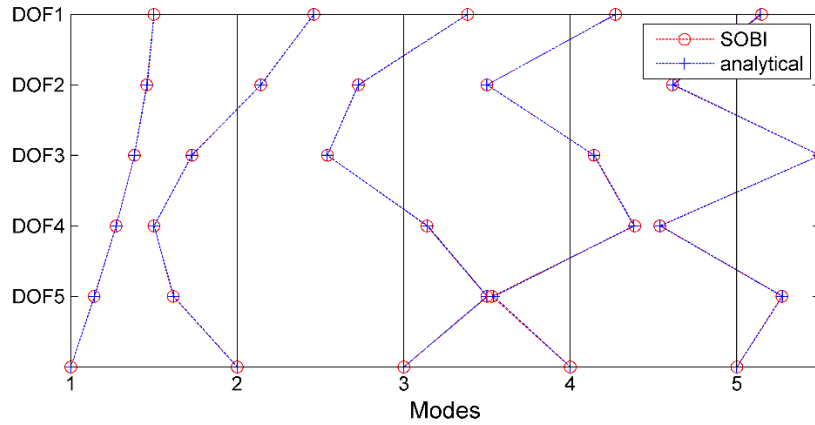


Figure 3.6 Mode shapes from analytical solution and from the mixing matrix  $a$ . Scaled to unit displacement in DOF1.

System 2a is analysed to check performance at closely spaced modes, and the deviation from analytical values are small.

Table 3-3 Results, system 2a

System 2a				
Mode	Analytical $f_n$	$\Delta f_n$ [%]	$\Delta \xi_n$ [%]	MAC
1	0.109	0.0749	4.12	0.99
2	0.309	0.101	1.12	1.00
3	0.499	0.594	7.87	1.00
4	0.740	0.116	2.67	0.99
5	0.751	0.238	8.50	0.99

System 1a is analysed with 5 different simulation durations. This was performed in order to investigate the error in damping ratio, as it was found to be almost 20 % in system 1a with 60 minutes analysis-length. Figure 3.7 shows how the damping deviates from the analytical result for different time-intervals.

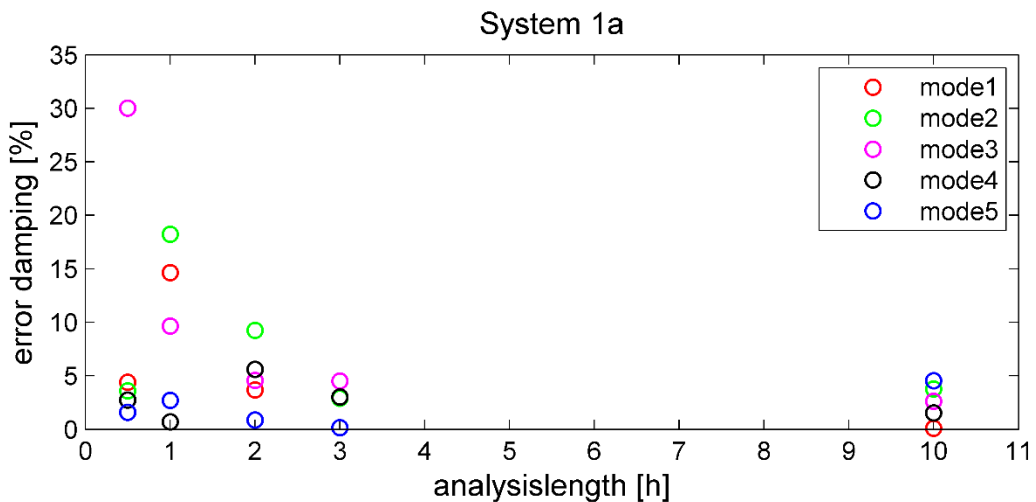


Figure 3.7 Error of damping ratio with respect to length of the analysed signal.

The duration of analysis is seen to improve the damping estimates, and the scatter for series of short duration is significant. However, in practical context, the loading is not likely to be stationary for a long time interval.

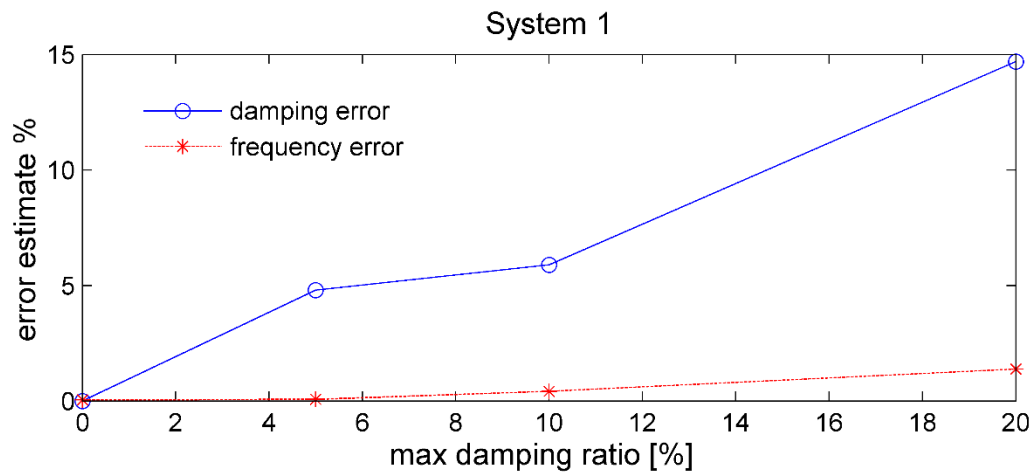


Figure 3.8 Error estimates for different damping ratios.

Mean error for each damping case in system 1 is provided in Figure 3.8, performed with an analysis-length of two hours. The damping ratio is found to have considerable impact on the error estimate, especially for damping error. It is also observed that frequency errors are generally notably smaller than for damping estimates, which corresponds to a series of research results from investigation of OMA methods [6].

### 3.3 Case Study 2 - Operational modal analysis of Dolmsundet Bridge

#### 3.3.1 Dolmsundet Bridge

The total length of Dolmsundet Bridge is 462 meters, with a maximal main span of 190 meters and a maximum sailing height of 32 meters. The bridge has two main pillars. The cross-section is a box girder with a height varying from 2.75 meters to a maximum of 10 meters positioned directly over the pillars. The maximum cantilever arm before connection is 98.7 meters. Additional support during construction is needed, and temporary structures are installed 48 m from the pillars, see Figure 3.9.

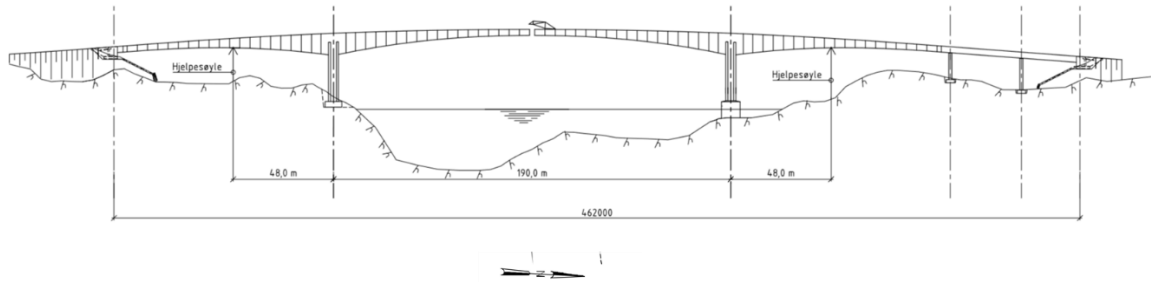


Figure 3.9 Bridge with dimensions, before connecting to adjacent cantilever.

A cantilever bridge is built from both sides, standing as two cantilevers before being connected at the middle. The span is expanded symmetrically from each side of the columns, to reduce the moment in the column. The dynamic demands are usually largest during construction, and this will often give the dimensional criteria of the bridge.

Dolmsundet Bridge is a cast-in-situ concrete construction. The falsework for each section is moved forward along the bridge as construction proceeds with a form traveller. A form traveller is attached to each side of the cantilever as seen on Figure 3.10. The form travellers are attached to the cross section by tension legs, between the different casting stages. The different casting sections are marked on figure Figure 3.9, where the largest section length is 4.9 meters [29].



Figure 3.10 Dolmsundet bridge under construction. a) view from Dolmsundet towards Hitra [30] b) Cantilever with form traveller on the cantilever edges [31].

A FEM analysis of the bridge is performed by Norwegian Public Roads Administration in the RM bridge program. The bridge is constructed for windload class II under construction, and for windload class I for the final structure [32]. Thus, calculation of dynamic response is only included during the construction phase. There are two construction stages of interest. Maximum free cantilever from axis 2, before installing a support-column, is called building stage B21. Building stage B22 is the critical stage, after added support structure and before connection to adjacent cantilever [32]. One additional section is added at one side to capture

the effects of unsymmetrical casting. The result from the dynamic analysis will be used for comparison in the method and result part of this thesis. Data from different construction stages are chosen in order to better understand the construction of a cantilever bridge with respect to dynamic parameters. An overview of calculated, predicted, cast stages and measurement points of interest is provided in Figure 3.11.

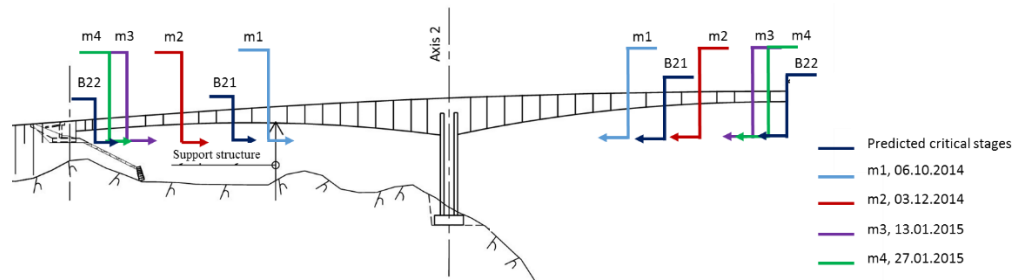


Figure 3.11. Included elements in the different analysis m1-m4, with dates of the obtained measurements.

### 3.3.2 Instrument positions

It is fundamental to achieve high-quality measurements in order to get the best modal identification estimates [6]. This varies with how the sensors are placed on the structure, and how the sampling frequencies are set. The sensor location affects the observability of the different structural modes. In this study, the sensor locations and their sampling frequencies are already set, and the measurement data is provided by Norwegian Public Roads Administration, obtained from the survey system provider Cautus Geo. Information about the instrument installation is found in the installation document for axis 2, received from the survey system provider [33]. There are 18 strain sensors, 8 located in the column and 10 in the pier head. In the work carried out for this thesis, it was revealed that strain measurements were collected for static analysis as they were sampled once every hour. Hence, they are useless for the purpose of dynamic analysis. Therefore, the vibration data available is the data from the two accelerometers, with acceleration measurements in three directions located on the north sides of axis2. Figure 3.12 shows the instrument positions with coordinates.

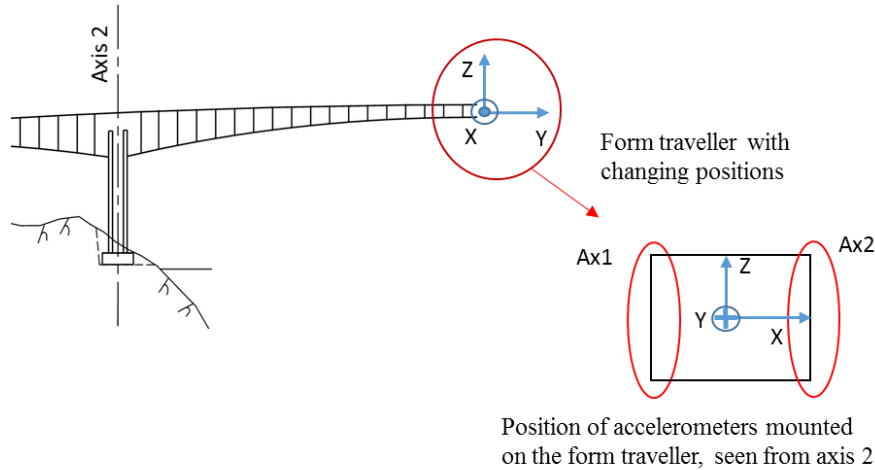


Figure 3.12 Instrument positions with local and global coordinates.

The 3D accelerometers are mounted on the form traveller. Thus, the accelerometers position changes during construction stages. The accelerometer positions for measurements in this study are shown and labeled in Figure 3.11.

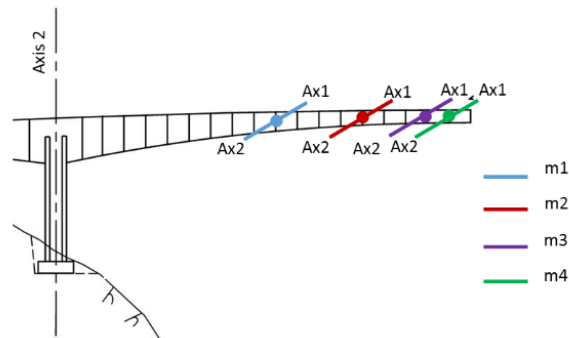


Figure 3.13 Accelerometer positions along the span.

Wind measurements are received from a 3D anemometer mounted on column axis 2, oriented in the north direction.

### 3.3.3 Description of file structure and importing considerations

This section gives a description of the dataset structure. The organization of data is explained in detail which will be helpful for others who wants to make use of the measurements. Firstly, an overview of the map structure is provided in Figure 3.14. Windfiles are stored in two main folders, containing different time-periods. Files are stored in subfolders, named for each date between the 15<sup>th</sup> of January 2015 and the 3<sup>rd</sup> of February. All wind data files obtained before the 15<sup>th</sup> of January are included in one folder. Acceleration files from the 15<sup>th</sup> of January



2015 to the 3<sup>rd</sup> of February 2015 are stored in one folder, while acceleration data prior to this date are stored in subfolders named after respective month.

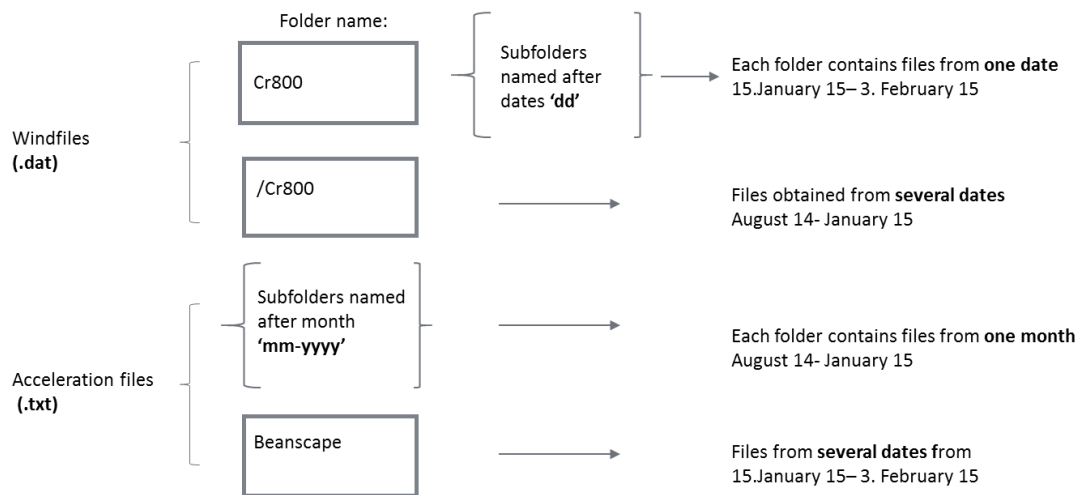


Figure 3.14 Overview over file storage.

Windfiles are saved as .dat files. The information used in this study includes information of date and time, vertical wind speed, wind direction and corresponding wind speed. Start date and time is labelled in the file name and saved in a new file approximately once per hour, stored with sampling frequency of 1 Hz.

Acceleration files are stores as .txt files, containing two columns each with information of record number and acceleration value for one direction. The record number starts with zero at the beginning of each sequence. Each sequence is stored in several files, starting as part000, part001, etc. Part000 contains metadata for the sequence, where one sequence represents approximately one hour of sampling. This is done separately for  $x$ ,  $z$ ,  $y$  direction and separated by noting 0\_0\_0, 0\_1\_0 and 0\_2\_0 in the filename. It is worth noting that the different sensors start their sequence at different time instants, and the record numbers for the different sensors do not correspond to eachother. However, the data series measured in the three directions of a sensor have corresponding record numbers. Accelerations are sampled with 100 Hz.

The rawdata is organized in a way that requires a location pointer in order to find series with desired wind properties, and then match it with the corresponding acceleration time series. The difference in start time of the different sensors needs to be adjusted for. An illustration of the procedure is given in figure Figure 3.15.

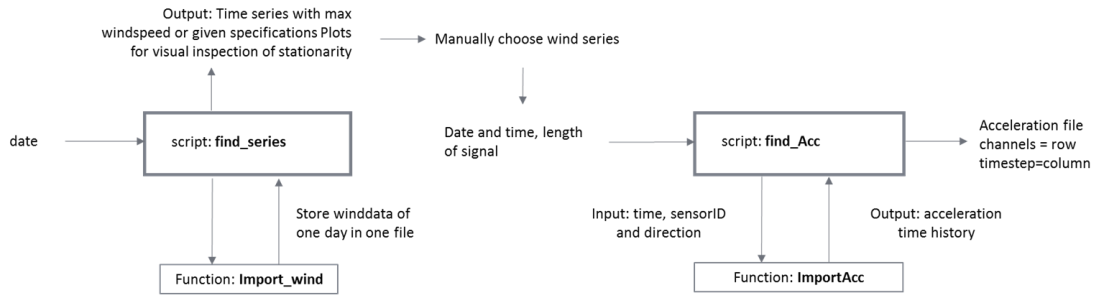


Figure 3.15 Flow chart of import procedure.

As the acceleration and wind is organized in different folders, they are best connected to each other by the date and time, which are given in the filename of each file. The script Find\_series imports wind files into one file for each day by the function Import\_wind. Thereafter, it searches for the time intervals with the highest wind speeds of each date. The start times of the chosen wind series are then the input to the find\_Acc script. Series of each direction and sensor are then imported with the function importAcc.

It should be noted that some of the recorded samples have dropped out. This must be corrected in order to prevent delay between vibration data from different sensors and directions. Find\_Acc solves this by doing linear interpolation with the function *interp1*(·) before the series are assembled. Example of the interpolation is shown in Figure 3.16. A cubic interpolation was found to add information, and increase amplitudes in the system, and linear interpolation was therefore preferred.

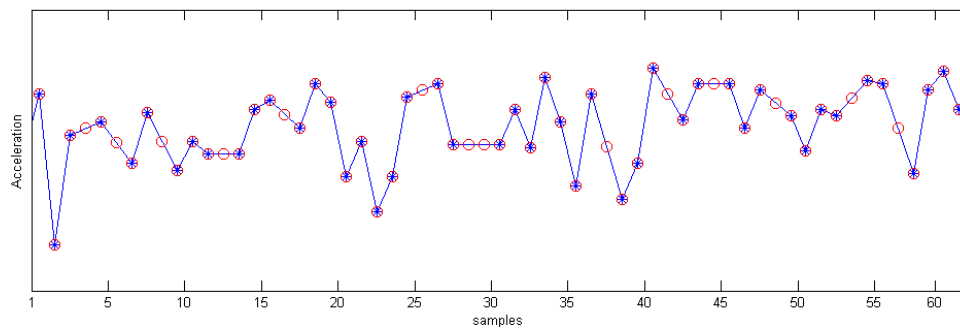


Figure 3.16 Illustration of 60 samples, sampled with  $fs=100$ . Blue stars denotes original series, red circles are added the series in the interpolation.

Data from each time interval was thereafter stored in a  $[6 \times n]$  dimensional matrix, with 6 different acceleration channels, and  $n$  is the number of sample points. The chosen series are given different IDs and an overview of selected series are provided in Appendix A.

---

### 3.3.4 Choice of time series

The data needs to be picked carefully in order to get the best possible estimates. It is important to analyze sequences where expected levels of vibration of the structure are significantly higher than noise from measurement devices and hardware [6]. Wind-measurements are used to choose the most adequate data, by ensuring the desired statistical properties and amplitude of the excitation system. A wind direction transversal to the bridge span was found to excite the fundamental modes adequately. This would be equal to the east-west direction, as the bridge spans from north to south. Firstly, the time series that were considered had comparable wind speed and wind direction throughout the building stage. This gave a low mean wind speed, which seemed too low to excite the modes of interest. Hence, the maximum mean speeds that occurred for different construction stages were investigated.

Time series collected by night were chosen in order to avoid building activity on the bridge, and thus reduce the amount of noise in the dataset. Hence, time series measured between 8 pm and 7 am are preferred. There is no adjustments for any potential storage of equipment on the bridge. This could affect the dynamic properties of the system.

### 3.3.5 Validation of dataset

Wind series are investigated in order to secure the assumption of stationary data. The direction is represented in Figure 3.17, in both Cartesian - and polar coordinates. The directional plot is corrected with `unwrap()` in MATLAB, such that the direction is represented within the interval  $0^\circ - 360^\circ$ . The time series used in the examples is obtained from the time series interval ID07, refer to Appendix A for ID overview.

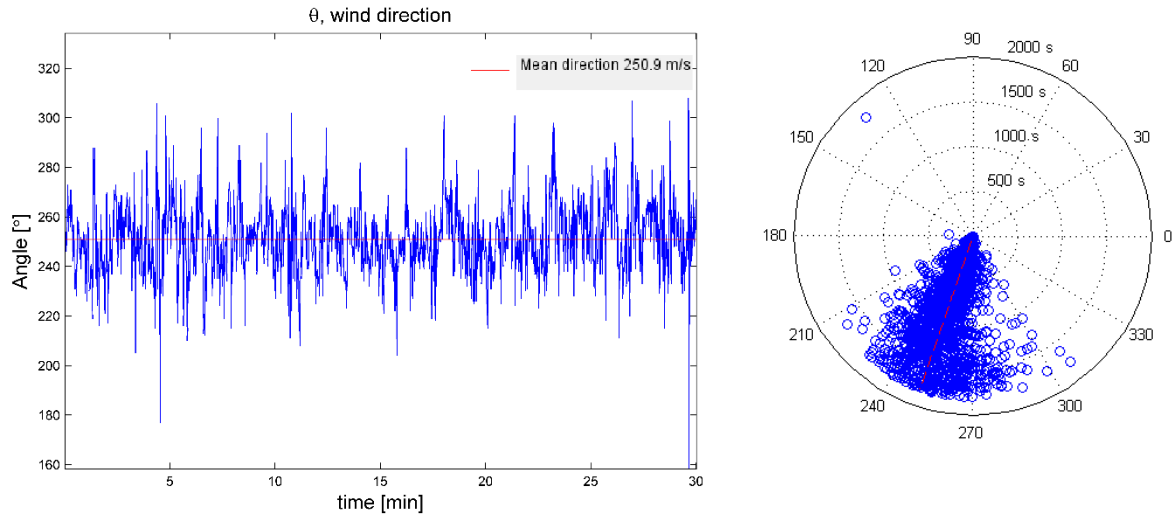


Figure 3.17 Wind direction a) Cartesian coordinates b) Polar coordinates.

The preferred time series for this study have a near constant wind speed and wind direction. A constant mean value, independent of the time it is calculated for, secures stationary behavior. The wind should follow a Gaussian distribution. Both horizontal wind for given directions and vertical winds are shown with its representative distribution in Figure 3.18. The red line shows the theoretical Gaussian distribution.

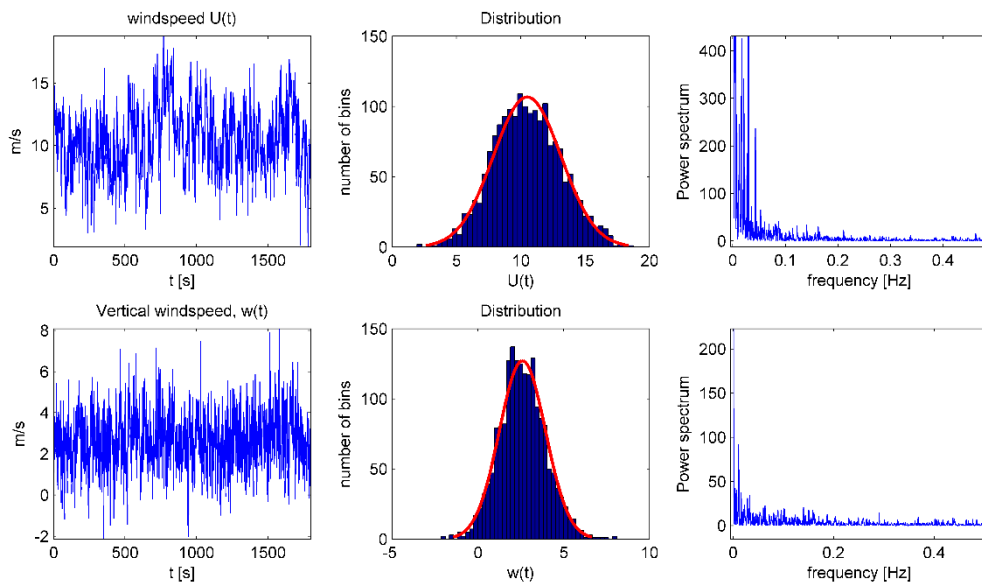


Figure 3.18 Wind time series, distribution and PSD plot for vertical- and horizontal wind speeds.

The load transfer function should equal a broadbanded process, in order to excite the structural modes of interest, refer to section 2.4. An overview of the PSD of the wind speed reveals that only low frequencies are excited. It should be noted that the wind is sampled

with 1 Hz, hence it is not possible to capture all fluctuation in the wind. Thus, the signal might contain aliasing, and its frequency distribution is questionable. However, it implies that a limited amount of modes would be found in the signal.

Inspection of time histories with respect to their distribution will reveal anomalies in the dataset. It should be a stationary, random signal and not exhibit any periodicities [6]. Acceleration series from from equivalent time-interval, obtained from sensor Ax1 in x-direction is investigated in figure Figure 3.19 and Figure 3.20.

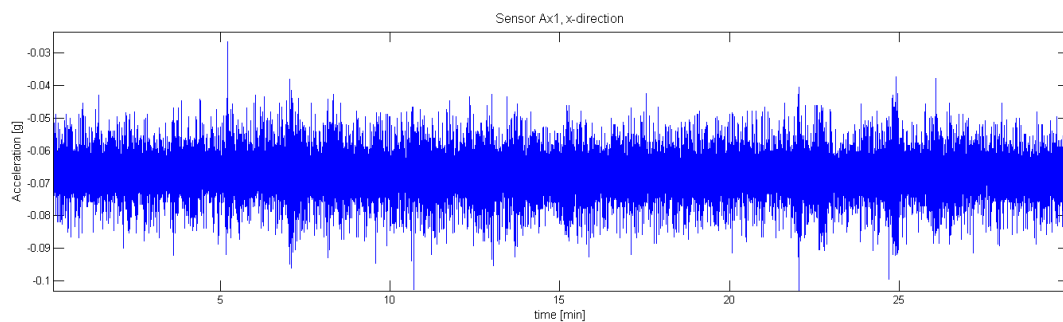


Figure 3.19 Acceleration time series.

The acceleration should follow a Gaussian distribution. However, the unfiltered acceleration does not seem to be Gaussian distributed. The tails of the probability distribution are to thick in comparison with the theoretical distribution marked with red solid line in Figure 3.20.

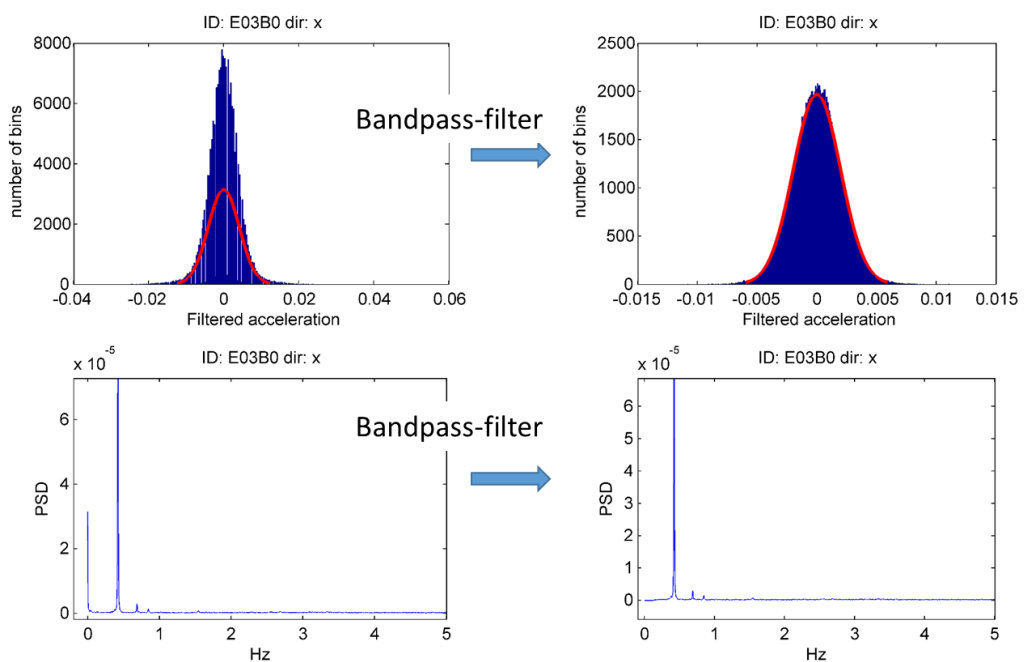


Figure 3.20 The raw data accelerations do not follow a Gaussian distributed, in a), and are bandpass filtered, shown in b).

A few possible reasons for why we can not obtain a Gaussian distribution are investigated. The higher mean wind speed, the more spikes are usually found in the signal. This might be due to physical events or intermittent noise. Spikes in the signal have short pulses, that have flat density spectra, and will provide a more flat distribution in the signal and make a thicker tail in the signal distribution. The noise might be induced by some periodicities, as a periodic signal will give sharp peaks in the distribution, which can be confused with narrowband resonances. This can to some extent be seen in the unfiltered acceleration distribution plot. Linear interpolation is applied to the dataset during import, see section 3.3.3. This causes a similar dropout effect in some series, and a dropout with duration of 0.5 sec can be seen in Figure 3.21. This might cause some inaccuracies [6] in the results and can be identified by spikes in the distribution.

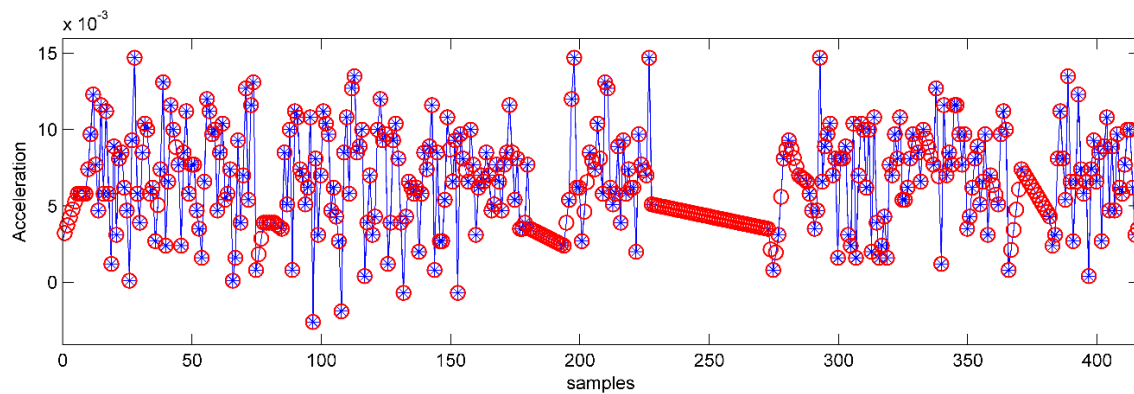


Figure 3.21 The linear interpolation creates dropouts in the signal.

This problem is reduced by applying band pass filter such that the acceleration is found to follow a Gaussian distribution, recall Figure 3.20. This is valuable information in the signal processing part, as most series needs band-pass filter in order to have the wanted distribution.

### 3.3.6 Signal processing

Firstly, the series are detrended in order to remove offsets from a zero-mean. A Butterworth high-pass filter and low-pass filter of order 5 are used in the signal processing. The high-pass cut off frequency is set to 0-0.2 Hz and the low-pass filter is applied with a cut-off frequency of 1-3 Hz, depending on the modes of interest and noise in the signal. A Butterworth filter with low-pass  $f_c = 3$  Hz and high-pass  $f_c = 0.14$  Hz is shown in Figure 3.22.

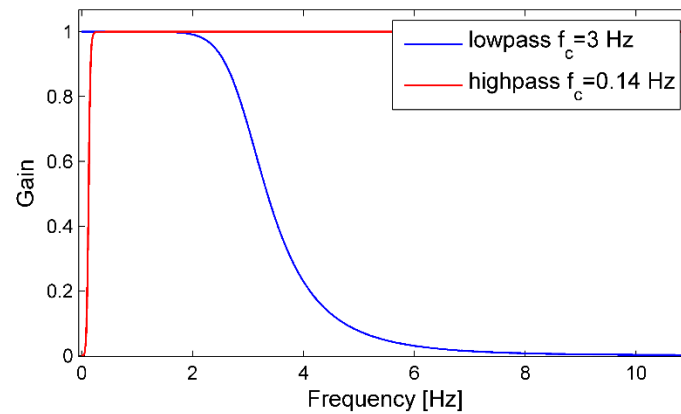


Figure 3.22 Applied filter Butterworth filter of order 5, with lower  $f_c$  of 3 Hz and higher  $f_c$  of 0.14 Hz.

An acceleration time series and spectral density, before and after applied filter, can be seen in Figure 3.23. The amplitude loss can be seen in the filtered time series. The PSD is attenuated below 0.14 Hz and above 3 Hz. The peak between 0.4 and 0.5 Hz is significantly more excited, and is not represented in order to get a better view of the impact from the Butterworth filter.

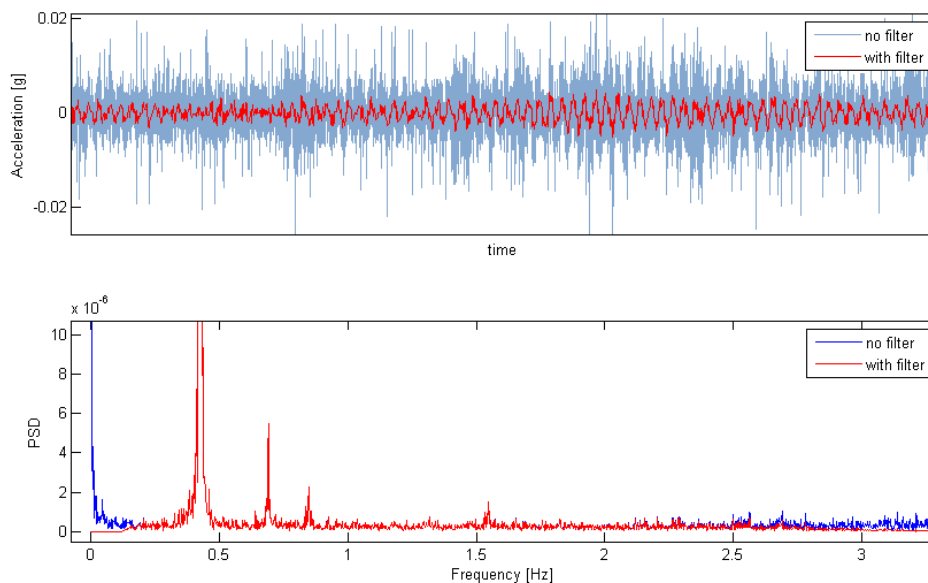


Figure 3.23 Acceleration time series, top plot, and spectral density, bottom plot, before and after applied filter.

The series are resampled in order to decrease computational effort. To avoid aliasing, the filter upper  $f_c$  is checked to be less than 50–80% of the *Nyquist frequency*, as recommended by Rainier [6]. For higher  $f_c = 3$  Hz, a decimation factor of 10 is applied, reducing the sampling frequency to 10 Hz from the original  $f_s = 100$  Hz.

### 3.3.7 Second-order Blind Identification method

SOBI seems to be more sensitive with regard to noise, and it is found necessary to filter closely to the wanted frequency, recall case study 1. Even though a peak close to 1.5 Hz can be seen from the PSD in the acceleration plot, Figure 3.23, this is not separated by the SOBI method. It was found necessary to filter with lower pass-band  $f_c = 1.5$ .

Due to classical whitening formulation, only the number of active modes needs to be included. PSD of the sources are viewed in Figure 3.24. Source 5-6 have significant noise and do not represent a SDOF system applied white noise spectrum. Hence, the number of active modes is set to  $N_m=4$ . In the whitening matrix calculation, only the four highest eigenvalues of the covariance matrix from the input signal and their eigenvectors will be included, as explained in section 2.4.1.

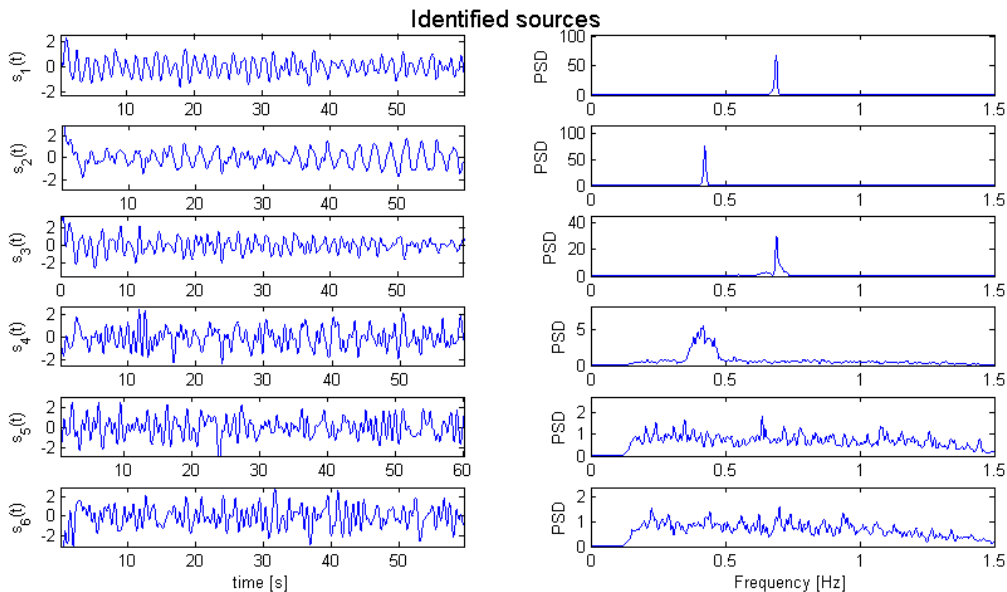


Figure 3.24 Choice of  $N_m$  active modes. Noise is seen in the two bottom time series.

The whitened signal satisfies the requirement of variance equal to identity matrix given in Equation (2.70). The separated sources should be independent of each other. However, the joint diagonalization does not make all sources independent, seen in Figure 3.25. Thus, one might expect sources 3 and 4 to not correctly represent modal coordinates.



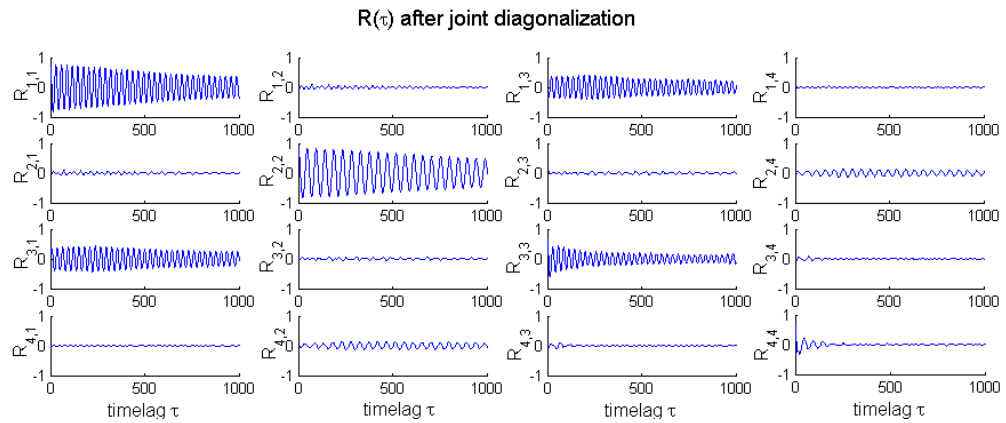


Figure 3.25. Cross correlation matrix of Sources for time-lags 1:1000.

Identified sources with their corresponding peak spectral density plots are shown in Figure 3.26. The PSD is not a part of SOBI. However, it gives an indication of the frequency content in the sources.

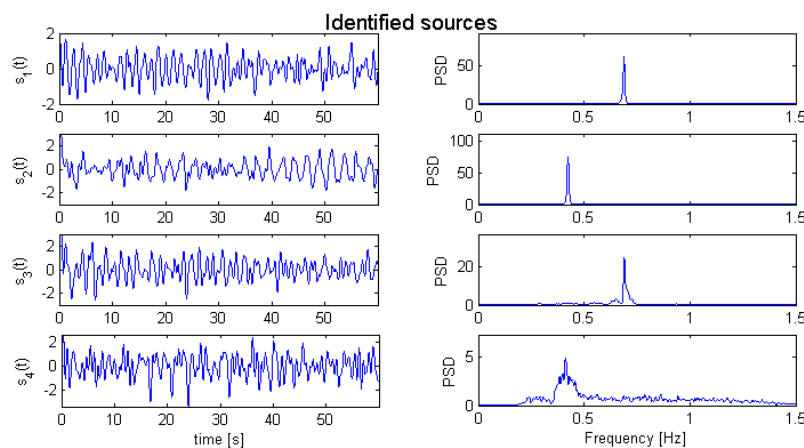


Figure 3.26 Identified sources with peak spectral density plot

Their autocorrelation functions are shown in Figure 3.27.

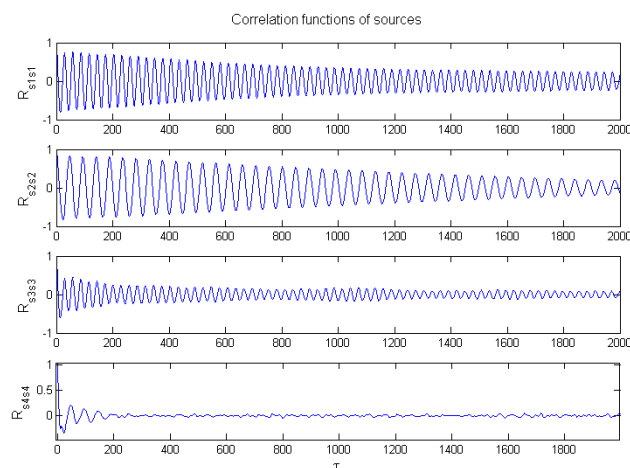


Figure 3.27 Autocorrelation functions with respect to number of time-lags,  $\tau$

SDOF methods are used to obtain frequencies and damping ratios. Figure 3.28 shows the identified maxima and zero crossings for correlation of source 1.

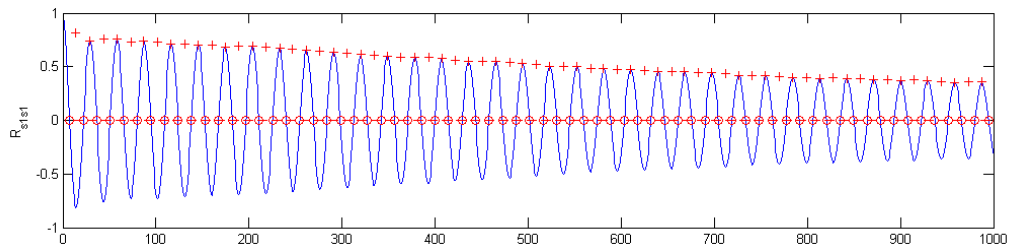


Figure 3.28 Zero crossings and maxima of autocorrelation function from source 1.

A linear regression on the logarithmic decrement and peak number is shown in Figure 3.29, with different numbers of peaks included. The correlation functions for source 3 and 4 are not well defined and damping estimates can give several different outcomes, depending of the number of peaks included in the regression.

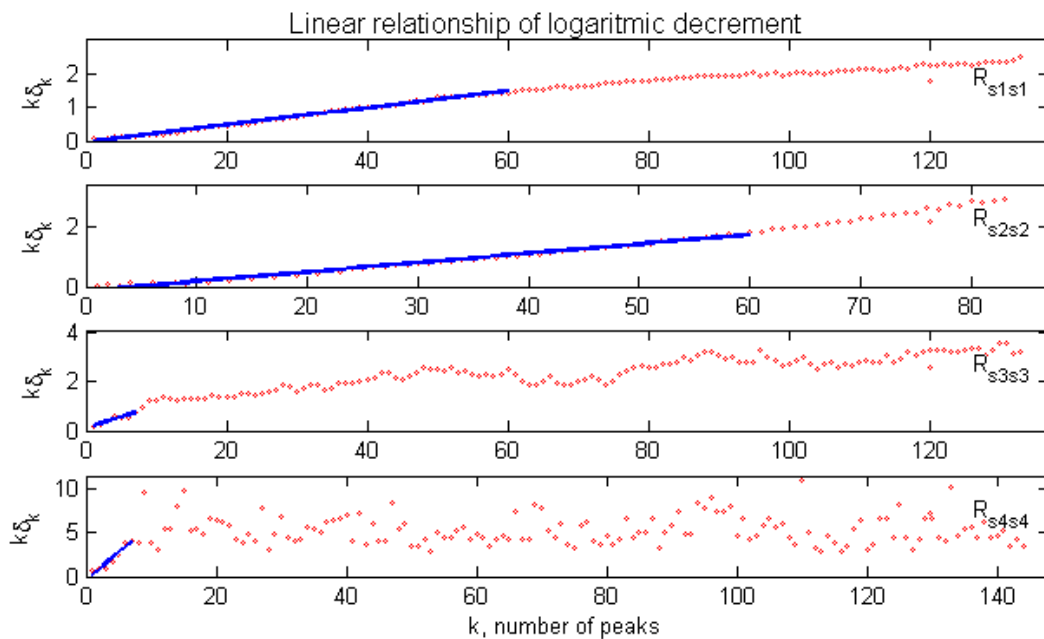


Figure 3.29 Linear regression of the logarithmic decrement

The obtained modal parameters with corresponding mode shapes are provided in results.

### 3.3.8 cov-SSI with MACEC software

MACEC 3.2 is a MATLAB toolbox for experimental and operational Modal Analysis of structures [5] and is used in this study. It is developed at the Structural Mechanics division of KU Leuven. The toolbox has data conversion, signal processing, system identification, methods for selection of modes and tools for visualization of data.

Several different identification methods are available, including deterministic, stochastic and combined deterministic stochastic system identification methods. As mentioned in section 2.4.2, the state-space models are robust and have a range of advantages and will be utilized in this analysis. The SSI methods are provided with both data driven and covariance driven versions, where SSI-covariance is preferred in this study due to its ability to provide variances of the estimates.

The acceleration time series are analysed with the Cov-SSI identification method. This provides a comparison with the SOBI obtained modal parameters. The spectra can be calculated for the obtained state-space model, and provides variances of the modal parameters, refer to section (2.4.2.1)

Signal processing is performed in the MACEC toolbox system. The current analyzed signal is processed with constant detrend, Butterworth filter of 5<sup>th</sup> order with lower  $f_c = 0.2$  Hz and higher  $f_c = 3$  Hz. A decimation factor of 10 is applied, achieving a new sampling frequency of 10 Hz. The parameters chosen for SSI and corresponding singular value plot are presented in Figure 3.30.

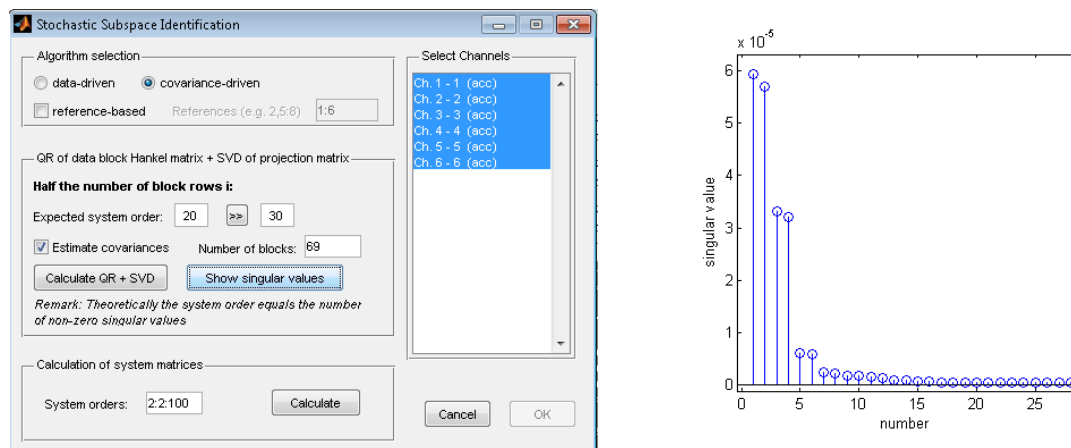


Figure 3.30 a) Screenshot of SSI window in MACEC b) Singular value plot

Firstly, an expected model order is determined. This should equal 2 times the number of expected modes, as the poles received are complex valued conjugate pairs. A few trials are carried out and an expected system order of 4-6 is found from the singular value plot, which are the singular values from the SVD of the block Toeplitz matrix of correlations. The gap between singular values should theoretically equal the order number necessary to describe the dynamical behaviour. Due to noise in the data, the order number needs to be over-specified, in correspondence with the discussion in section 3.3.8. The order number is over-specified by MACEC and the expected model order is therefore multiplied by 8, yielding an order number of  $8 \times 20 = 160$  [5].

The block number  $i$  determines the number of covariance matrices gathered in the block Toeplitz matrix. The required number of block rows is specified with Equation (2.94) by MACEC and equals 27 in this case. This is only a recommendation for the minimum block  $i$  value. From Reynders and De Roeck, it is recommended to set the block rows as large as possible [27]. Their recommended number of blocks is given with respect to the sampling frequency, given by  $i > \frac{f_s}{2*f_0}$ . This will correspond to a minimum of 13 blocks, when  $f_s$  is equal 10 Hz and the minimum frequency  $f_0$  is set to 0.4. Hence, their suggestion yields a lower bound. However, even higher numbers of blocks were investigated, but gave less stable modes in the stabilization diagram. According to Raineri et al (2010) the variance of the estimate decreases when the number of block rows increases due to the noise rejection, but increases again with an overestimated block row number [34]. Hence, an optimization of the number of blocks  $i$  is necessary, and several trials were investigated.

The maximal possible system order is equal to  $i \times l$ . However, from the singular value plot, the physical poles are prone to stabilize earlier. Hence, the maximum order in the construction of the stabilization diagram is set to  $n=100$ , with stepsize 2. In order to estimate the covariances, a number of blocks must be chosen, see Figure 3.30. This block number equals the number of blocks that the time data is divided into, before the sample covariances are calculated. The number of blocks is set to the MACEC suggested value of 69. The number needs to be large enough to give a reasonable accuracy of the variance, yet low enough for the data blocks to be statistically independent of each other.

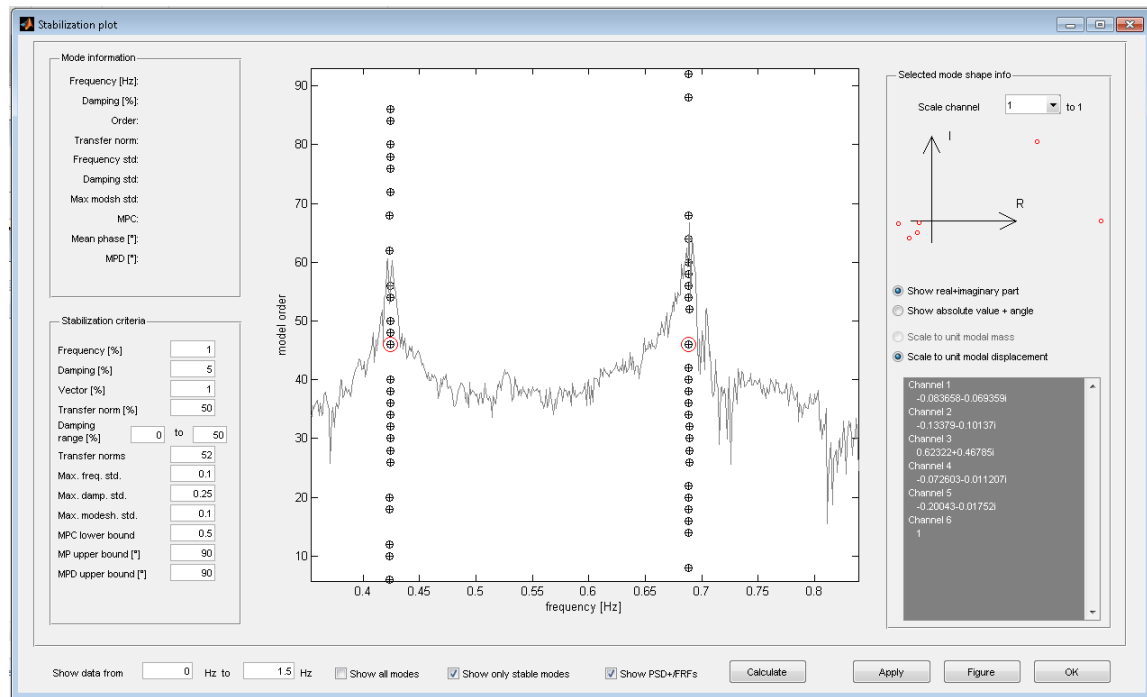


Figure 3.31 User interface in MACEC of the stabilization diagram, provided with variance limits.

The nonzero singular values from the Toeplitz matrix are used to compute the observability matrix and reversed controllability matrix. The state matrix  $[A]$  is then achieved and the poles are found from the eigenvalues determined for different system orders. These are plotted in a discrete format in the stabilization diagram. Mathematically, an equal number of poles and order of system will be obtained. This gives a number of spurious poles, which can be sorted out in the stabilization diagram. A screenshot of the stabilization window is given in Figure 3.31. Here, the variance criteria is applied. If the covariance criteria is left out, the parameters for validity is set to 1% for frequency, 5% for damping and 1% for mode shapes. The obtained stabilization diagram is given in Figure 3.32.

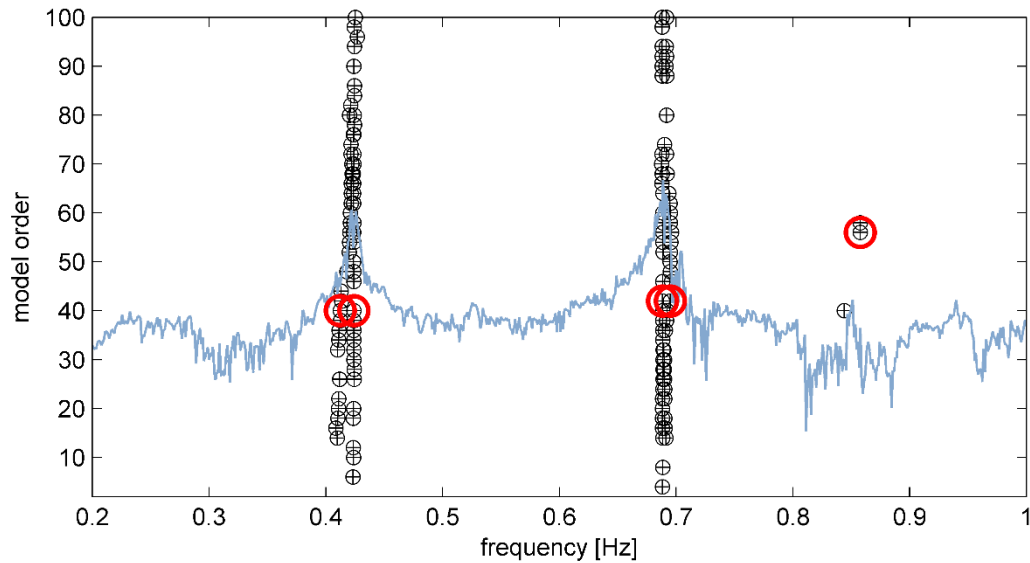


Figure 3.32 Stabilization diagram, without variance limits, 5 modes are selected in frequency range from 0.2-1 Hz.

Physical poles are chosen from the alignment of stable modes. As the objective is identification of accurate modal parameters, and not to obtain an estimated order number, poles are chosen from different order numbers. Poles with MPC close to 1, MD close to  $0^\circ$  and a low MPD value are preferable, indicating low damping values and non-complex mode shapes.

To better distinguish the spurious and physical modes, a power spectrum is shown on top of the stabilization diagram, even though it is not a part of the SSI method. This is shown in Figure 3.32. One pole is selected for each identified structural mode, marked with the red circle in the figure. These poles denote where the modal parameters are estimated from, presented in the result section.

Results from all investigated time series are provided in Appendix B. A few comments are made on often-occurred stabilization diagram. Alignments of apparently stable modes shows up for poles around 2 Hz, and around the lower cut off frequency and higher cut off frequency. However, these are easily distinguished from the physical poles by looking at the damping ratio, which is unrealistically high for those frequencies. The poles around 2 Hz are assumedly a result of coloured input instead of white noise, which means that the load frequencies might appear as modes. The spurious modes are identified by unreasonably high damping of about 30%, and are not included as stable poles. If several sensor points were present, they would most likely be distinguished from physical modes by weird looking mode shapes.

## **Chapter 4      Results and discussion**

The results section contains two parts.

The first part presents the obtained result of time series, ID7, and predicted measurements from building stage B22. This is outlined in order to investigate the quality and consistency of obtained results from the two modal analysis methods. The results are found by investigation of time series ID07, which is obtained at stage m4. The reader should be aware of the difference of between stage B22 and stage m2, recall Figure 3.11. Stage m4 includes one less cast section than predicted stage B22, reducing the dimension of each cantilever by 4.9 meters. The parameters and analysis considerations for these given results are presented in method sections 3.3.7-3.3.8.

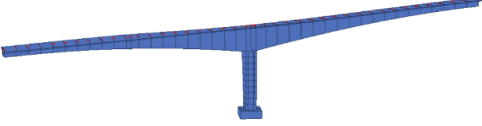
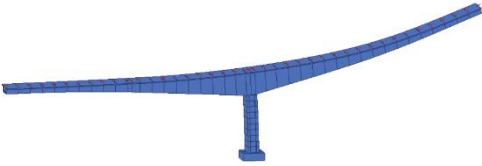
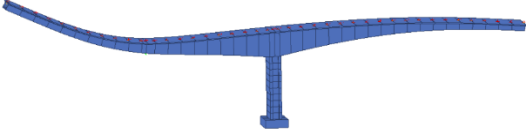
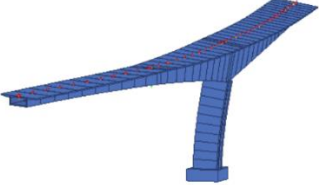
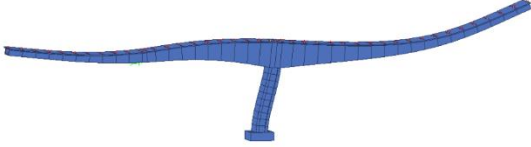
The second part presents the results obtained from different building stages. The emphasis is comparing trends and predicted behavior. Results from all time series analysed can be found in the Appendix(B).

### **4.1    Modal parameters from construction stage 2**

#### **4.1.1    Predicted modal parameters**

The following eigenfrequencies and mode shapes are predicted by the Norwegian Public Roads Administration for construction stage B22. A 0.8% damping ratio is applied in the model for the dynamic analysis of the Service Limit State (SLS) [32].

Table 4-1 Predicted eigenfrequencies and mode shapes for construction stage B22. Illustration and frequencies are obtained from calculation report provided by the Norwegian Public Roads Administration [32].

<p>MODE 1</p> <p><math>f_1 = 0.472</math></p> <p>Torsion of column</p>	
<p>MODE 2</p> <p><math>f_2 = 0.583</math></p> <p>Vertical displacement of cantilever</p>	
<p>MODE 3</p> <p><math>f_3 = 0.945</math></p> <p>Vertical displacement and torsion of deck</p>	
<p>MODE 4</p> <p><math>f_4 = 1.339</math></p> <p>Transversal bending</p>	
<p>MODE 5</p> <p><math>f_5 = 1.389</math></p> <p>Bending of cantilevers</p>	

#### 4.1.2 Modal parameters obtained by SOBI

Review Figure 3.27 for the obtained sources from time series ID07. As it is not possible to determine the order of the identified sources by the SOBI method, the frequencies are sorted in ascending order [21]. Corresponding source number is given in Table 4-2.



Table 4-2 Result obtained by SOBI, time series ID07, construction stage m4.

Mode	$f_n$ [Hz]	$\xi$ [%]	Source number
1	0.4002	10.0887*	4
2	0.4235	0.4517	2
3	0.6885	0.4009	1
4	0.6931	2.6062	3

\* denotes much uncertainty from when the damping ratio was found from a linear regression on the logarithmic decrement seen in Figure 3.29.

A look at the PSD of source 4, in Figure 3.27, reveals a source that is not fully separated. The influence of other frequencies is significant. It is likely that the obtained modes are contributions from several processes or noise.

Four mode shapes are obtained from the mixing matrix and illustrated together with corresponding frequencies in Table 4-3. The modes are scaled to unity. Due to sensor location, only local displacements are available, and only one cantilever end is investigated. The left plot illustrates the edge of the deck, and seen from the column, axis2. Here, modes with vertical and out-of plane movement can be illustrated. Corresponding coordinates can be reviewed from Figure 3.12. The view of the right plot is from above the deck. Movement in the bridge span direction (coordinate y) and transverse to the span (coordinate x) can be observed.

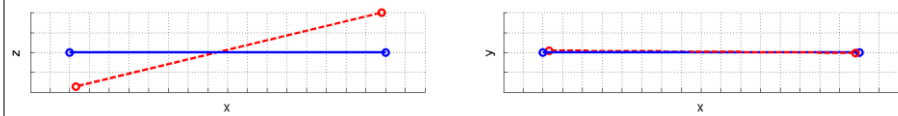
Table 4-3 Illustration of modes obtained from SOBI, and labelled with assumed mode shape description.

<p>Mode 1</p> <p><math>f_1 = 0.4002</math></p> <p>Undetermined</p>	
<p>Mode 2</p> <p><math>f_2 = 0.4235</math></p> <p>Torsion of column</p>	
<p>Mode 3</p> <p><math>f_3 = 0.6885</math></p> <p>Vertical displacement</p>	

Mode 4

$$f_4 = 0.6931$$

Torsion of deck



Visual inspection of the cantilever edge movements may give indicators of the bridge's global mode shape. Mode 1 shows high uncertainty, both due to the correlated source and by visual inspection of the mode shape. The mode shape indicates movements of both cantilever edges in opposite x-directions. This is inferred as large strain in the concrete box girder and does not represent a physical movement for such low frequencies. However, it can also occur due to movements of the other cantilever and a minor displacement in the measured end. Then the unrealistic movement in the x-direction might be accounted for from enlargement of the shape due to unit scaling. It will be regarded as non-physical due to lack of further information.

Mode 2 shows lateral movement of the cantilever end. This might indicate torsion of the column. Torsion of column is an expected finding when referring to the predicted mode shapes. The vertical displacement of mode 3 might indicate a vertical displacement of the cantilever deck, either caused by bending of the cantilever or as vertical displacement of the cantilever. The vertical twisting of the deck seen in mode 4 indicates torsion of the bridge deck.

An AutoMAC matrix of the obtained SOBI modes is provided in Figure 5.2. An AutoMAC matrix was created in order to investigate the dependence between obtained mode shapes. This is used in order to detect non-real obtained modes or investigate the efficiency of the sensor locations. Correlation might indicate that same mode shape is identified for distinct modes, or indicate a non-efficient sensor layout. It also might indicate problems such as spatial aliasing or spurious modes.

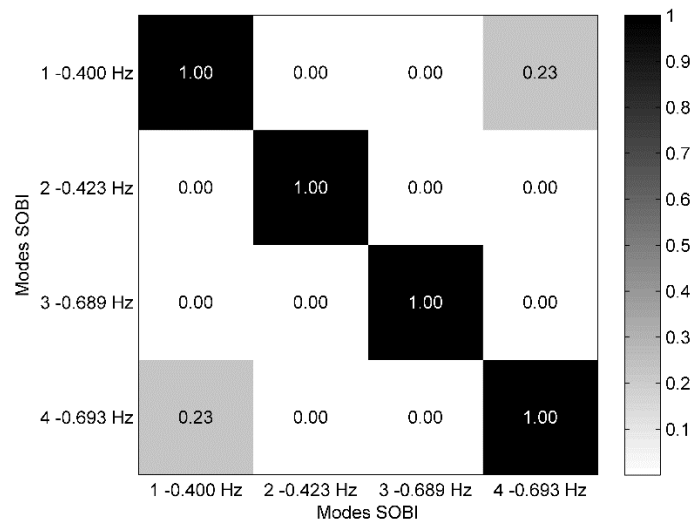


Figure 4.1 AutoMac matrix of modes obtained from SOBI.

The diagonal shows the modes correlated with themselves, and will, by definition, be equal to one. The off-diagonal terms provide a measurement of the colinearity between the obtained modes. Zero indicates no correlation and 1 is complete coincidence. Note the correlation between mode 1 and 4. By visual inspection, this is due to the torsion of deck being present in both mode shapes. Since information is compared from only a few points, this might also imply inefficiency of the sensor layout.

#### 4.1.3 Modal parameters obtained by cov-SSI

Cov-SSI was performed with the MACEC toolbox in MATLAB. The modal parameters with a 95 % confidence interval of the Gaussian distribution are provided in Table 4-4. The confidence interval is estimated based on the obtained space-state model in MACEC. The MPC, MP and MPD values are provided in order to investigate the modes shape's complexity. A completely real mode shape will hold a MPC equal to 1, and MP and MPD equal to 0.

Table 4-4 Result obtained by Cov-SSI, time series ID07, construction stage m4. Included with  $2\sigma$  confidence interval.

Mode	$f_n$ [Hz]	$\xi$ [%]	MPC	MP	MPD
1	$0.4122 \pm 0.0161$	$7.3715 \pm 2.5961$	0.89	3.42	12.4
2	$0.4239 \pm 0.0013$	$0.4120 \pm 0.2358$	0.99	2.35	4.57
3	$0.6883 \pm 0.0026$	$0.5358 \pm 0.3629$	0.65	13.5	17.7
4	$0.6951 \pm 0.0225$	$3.0443 \pm 2.3455$	0.84	1.00	15.0
5	$0.8576 \pm 0.0296$	$1.5797 \pm 4.5774$	0.86	4.15	11.5

Note the significantly smaller uncertainty for the damping and frequency of mode numbers 2 and 3. The complexity varies, with number 3 being significantly more complex, with a low MPC value and a significant MP and MPD value. The mode shapes are illustrated in Table

4-5. The upper plot provides the cantilever edge seen from column axis 2, whereas the lower plot illustrates the edge from above. A complexity plot is provided for each mode, where each arrow equals displacement in one DOF with illustrated phase angle.

Table 4-5 Illustration of modes and complexity plot obtained from Cov-SSI and labelled with assumed mode shape description

<p>Mode 1</p> <p><math>f_1 = 0.4122</math></p> <p>--</p>	
<p>Mode 2</p> <p><math>f_2 = 0.4239</math></p> <p>Torsion of column</p>	
<p>Mode 3</p> <p><math>f_3 = 0.6883</math></p> <p>Vertical displacement</p>	
<p>Mode 4</p> <p><math>f_4 = 0.6951</math></p> <p>Torsion of deck + Vertical</p>	
<p>Mode 5</p> <p><math>f_5 = 0.8576</math></p> <p>Vertical displacement</p>	

The modes are illustrated with their real parts. This will not give a significant difference for complex modes with maximum phase of  $\pm 10^\circ$  from  $0^\circ$  to  $180^\circ$  [6], but it is considered approximate to apply this to all phase angles [2]. The first mode in SSI exhibits non-physical movement in the x-direction. This might be due to a spurious obtained mode, review the stabilization diagram in Figure 3.32, with two closely spaced modes at frequency 0.4 Hz.

The complexity of the mode shape is pronounced, with one DOF displacement  $30^\circ$  off-phase. Mode 2 shows an almost completely real mode with lateral displacement, this can be interpreted as torsion of the column, equivalent to mode 2 obtained from the SOBI method. Mode 3 has vertical displacement and a small amount of twisting, indicating a mode with vertical displacement and torsion of the deck. However, the complexity plot indicates a complex mode, as also seen from high MPC, and low MP and MPD value. Complex modes occur if non-proportional damping is present, but is also often a result of noise in the measurements, recall theory section 2.4.3. The variance obtained from cov-SSI is low, so a complex mode may be more likely than noise in the measurements. Mode 4 displays the same behavior as Mode 3, but the torsion of the deck is pronounced. This mode also has a high complexity, but low amplitude. Mode 5 has some complexity and contains both vertical and lateral displacement indicating vertical displacement and torsion of the column.

The following gives the AutoMAC matrix of obtained modes from cov-SSI.

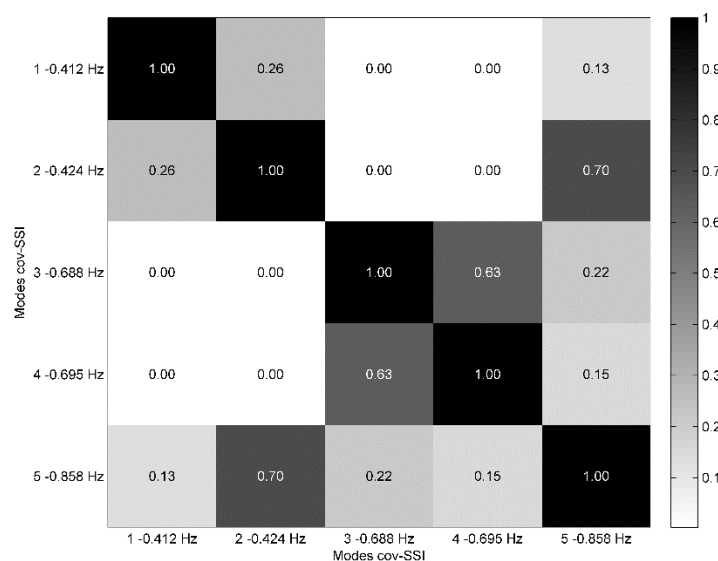


Figure 4.2 AutoMAC matrix of the modes from cov-SSI

The correlation between modes 2-5 and 3-4 stands out with a value above 60 %. This corresponds to the visual inspection of the modes. Review Table 4-4 where modes 1, 4 and 5 have a significantly higher confidence interval for both frequencies and damping together, and with a less stable alignment on the stabilization diagram for the same modes. It is likely that modes 1, 4 and 5 are spurious modes.

#### 4.1.4 Comparison of modal parameters obtained from SOBI and cov-SSI

The mode shapes are visually inspected in order to compare corresponding eigenfrequencies. The four first modes from SOBI and SSI will be compared in the following, even though some of the mode shapes deviate slightly. All of these are included in the comparison analysis, even though some of the modes show dependence in the AutoMAC matrix, as this could be due to inappropriate sensor layout. The relative scatter between frequency and damping from the two methods in comparison are noted in Table 4-6 together with the corresponding MAC value.

Table 4-6 Relative scatter and mac values comparing SOBI modes with cov-SSI

SOBI/ SSI	$\Delta f_n$ [%]	$\Delta \xi_n$ [%]	MAC
1/1	2.92	36.9	0.53
2/2	0.113	9.64	0.99
3/3	0.0323	25.2	0.87
4/4	0.291	14.4	0.66

Note, the relative scatter of lightly damped modes is severe. Mode shape vectors are compared with a scatter diagram in Figure 4.3. Positive real values are plotted for comparison. The vectors real parts with positive signs are compared. A line going through the origin with a slope of  $45^\circ$  is added to the plots. For perfect collinear modes, the points should lie on this line.

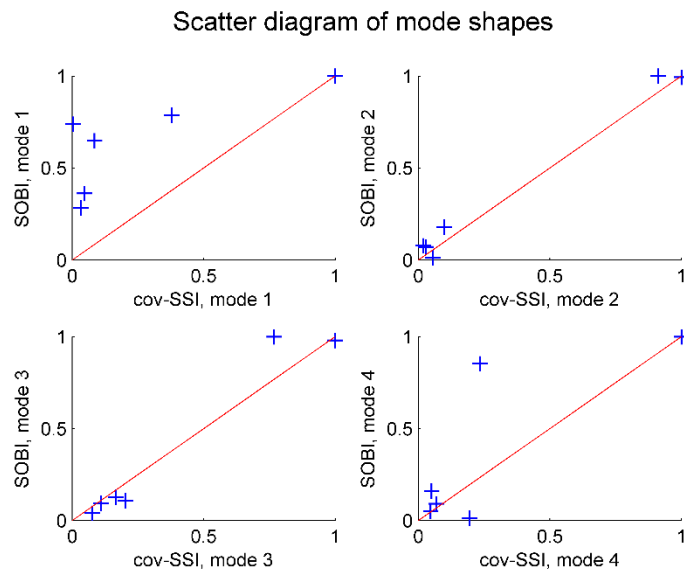


Figure 4.3 Scatter diagram representing the scatter between mode shape vectors obtained from the two methods.

Note that cov-SSI gives consistently lower values compared to SOBI. This might be due to the complexity of cov-SSI, and the absolute value might be larger. Note the distribution of points in mode 1, with nearly all points on one side of the  $45^\circ$  line. Deviations with all points

on one side might imply a systematic error. It seems like mode 2 and 3 show good consistency. The diagram does not ensure validity, only consistency between the methods.

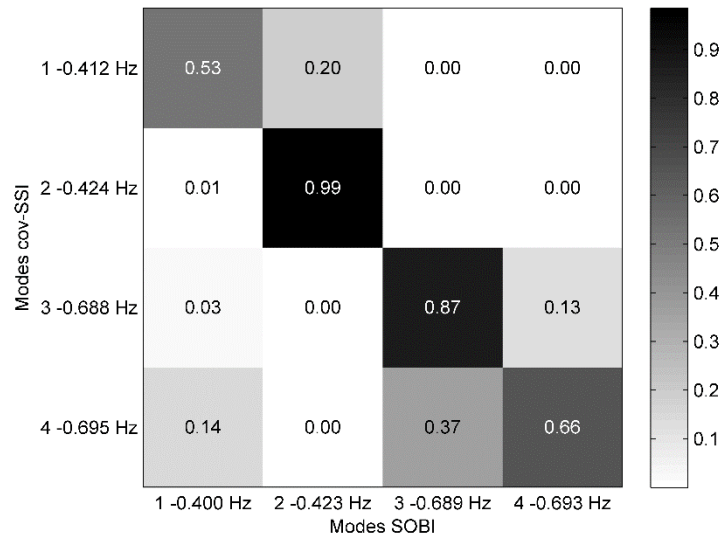


Figure 4.4 CrossMAC matrix of SOBI and cov-SSI modes.

The CrossMAC matrix between the mode shapes considered for the comparison are provided in Figure 4.4. MAX-values larger than 0.8-0.9 are accepted as indicators of good consistency in practical aspects [6]. Good consistency is observed between mode 2 from SOBI and mode 2 from SSI (hereafter noted mode 2/2) and between mode 3/3, with high MAC values on the diagonal. Note the low MAC value between modes 1/1 and modes 4/4. This might result from the cov-SSI mode, which seems to be a combination of several distinct modes. Recall the assumption of mode 1 and 4 being spurious modes. The low consistency between the methods supports this assumption.

The modes that show consistency between the methods, and hold a physically reasonable mode shape obtained from an independent source in SOBI, are reviewed in Table 4-7. They will be used further in comparison between different construction stages. The modes are labeled after their assumed global mode shape. TC=Torsion of Column, V=Vertical displacement of cantilever, TD=Torsion of Deck.

Table 4-7 Modes chosen to be compared for different construction stages

SOBI/SSI mode	SOBI		SSI-cov		MAC	Mode label
	$f_n$ [Hz]	$\xi$	$f_n$ [Hz]	$\xi$		
2/2	0.4235	0.4517	$0.4239 \pm 0.0013$	$0.4120 \pm 0.2358$	0.99	TC
3/3	0.6885	0.4009	$0.6883 \pm 0.0026$	$0.5358 \pm 0.3629$	0.87	V

Even though there is a high relative scatter between damping ratios from Table 4-6, both the damping ratio and the frequency estimates from SOBI fall within the confidence bound found from cov-SSI.

The comparison between the predicted and analyzed mode was done through visual inspection. The Torsion of Column (TC) and Vertical displacement (V) modes are found in both the analyzed and predicted results. The frequency deviation between the predicted and analyzed results is significant, due to the element difference between stage m4 and B22. The measured wind speeds did not reach velocities large enough to excite higher modes.

#### **4.1.5 Uncertainty considerations**

Several sensors at different locations are helpful in order to eliminate spurious and uncertain obtained sources. Here, only assumptions of mode shapes are available, and the presented results will not be enough to assess the correct modal shapes. The quality of visual inspection is therefore shown to be limited. This makes it harder to reject spurious modes on the basis of coincidence from MAC values.

Coincidence of mode shapes from different methods can be seen through MAC values close to 1 and low scatter values. However, this does not imply accuracy to the real modes. Errors might be present and bias the results from both methods. One of these biases might follow from the analyzed dataset. The interpolation utilized before the data was assembled introduced a drop out in the signal that can lead to errors in both methods. However, this bias can be limited if a large number of time series is analyzed.

The SOBI method does not identify complex modes, which might be a source of the uncertainty in the presence of complex modes, which are implied by the cov-SSI estimates. The SOBI method has problems with repeated modes, recall section 2.4.1. As few sensors are available, so modes might appear to be repeated even though they would turn out to be distinct with several sensor locations.

The OMA technique assumes white noise. In a practical context, few processes are perfectly white, resulting in inaccuracies of the results. Noise in the data can produce highly damped modes, which are found and rejected in the stabilization diagram provided by cov-SSI. Noise in the data leads to spurious and complex modes.

The accelerometers are mounted on the form traveler. This is attached to the bridge cross-section by tension legs and is assumed not to influence the obtained vibration from the system. Little information of the form traveller's appearance has been available. Thus, the



impact of the form traveller to the investigated system is not verified and might add errors to the result.

## 4.2 Variation of Modal parameters through different building stages

The previous section reviewed the uncertainty of the measurements and measured consistency by comparison between methods. Eight distinct time series from construction stage m1-m4 are analyzed with both cov-SSI and the SOBI method. As SOBI found more shapes in general, these are included even though consistency with SSI method is not present. This might be due to different stabilization criteria from SSI and choices of SOBI modes. In addition, different signal processing filter  $f_c$  have been applied, which might also influence the results.

It has been found reasonable to distinguish the findings into modes that might correspond to Torsion of Column (TC), Vertical displacement of cantilever (V) and Torsion of Deck (TD). Review Table 4-3 and Table 4-5 for an illustration of the mode shapes.

### 4.2.1 Eigenfrequencies

The frequencies obtained from time series 1-8 are shown in Table 4-8. The variation in the eigenfrequencies within each construction stage is found to be small. It is noted that Torsion of Column (TC), Vertical displacement (V) and Torsion of Deck (TD) are present in all stages.

Table 4-8 Frequencies obtained from casting stage m1-m4, frequencies are given as SOBI/SSI

SOBI/SSI	Series ID	Mode label		
		TC	V	TD
m1	1	0.4408/-	0.4860/0.4846	0.4866/0.4862
	<b>Mean m1</b>	<b>0.4408</b>	<b>0.4853</b>	<b>0.4864</b>
m2	2	0.5635/-	0.9909/0.9903	0.9929/0.9947
	3	0.5625/-	0.9926/0.9897	0.9919/-
	4	0.5620/-	-/0.9954	-/-
	<b>Mean m2</b>	<b>0.5627</b>	<b>0.9918</b>	<b>0.9932</b>
m3	5	0.4526/-	-/0.7593	0.7584/-
	6	0.4508/0.4521	0.7596/-	0.7608/-
	<b>Mean m3</b>	<b>0.4518</b>	<b>0.7594</b>	<b>0.7596</b>
m4	7	0.4237/0.4239	0.6890/0.6884	-
	8	0.4240/0.4243	0.6867/0.6872	0.6966/-
	<b>Mean m4</b>	<b>0.4240</b>	<b>0.6878</b>	<b>0.6966</b>

Figure 4.5 shows the mean values of eigenfrequencies with respect to construction stages. The plot demonstrates an increase of frequency value between stage m1 and m2 and a reduction in frequency values between stage m2 and m4. The same tendencies are

pronounced for the three different modes of interest. It should be clear that the stages are not equally spaced in time or by casting stage, and the slope is not indicating a rate.

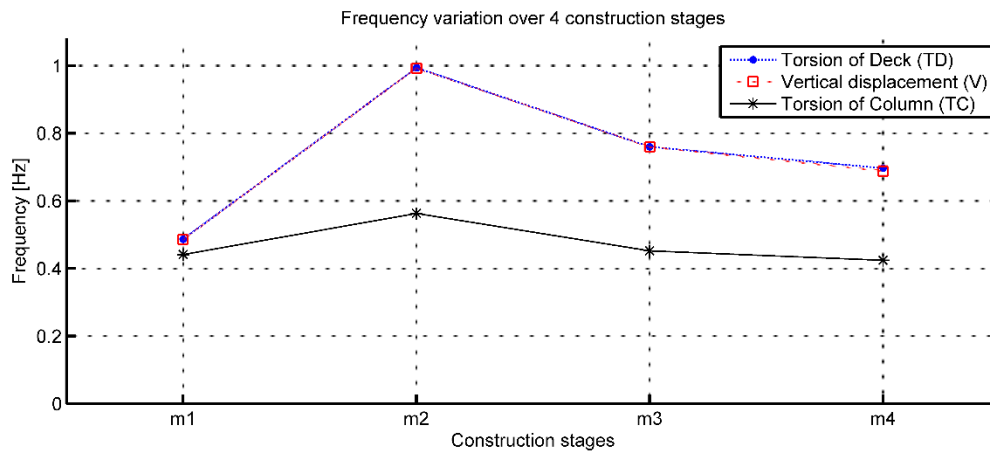


Figure 4.5 Frequency variation for construction stage m1-4.

Adding mass during construction stages is assumed to reduce the eigenfrequencies. The findings in Figure 4.5 support this assumption within the interval m2-m4. The jump between stage m1 and m2 can be explained to be a result of the installation of the support structure between these stages. The increase in frequency between m1 and m2 is observed for all modes, but is significant for modes including vertical displacement. A support structure is likely to affect the vertical modes the most, as the temporary support column is weaker with respect to bending than axial deformation.

Table 4-9 Frequencies and mode labels from predicted construction stages B21 and B22, mode 1-3.

mode	B21		B22	
	$f_n$ [Hz]	Mode shapes	$f_n$ [Hz]	Mode shapes
1	0.419	Torsion of column	0.472	Torsion of column
2	0.448	Vertical displacement of cantilever	0.583	Vertical displacement of cantilever
3	0.958	Bending in transversal direction	0.945	Vertical displacement and torsion of deck

The relation between eigenfrequencies from analysis and the two first predicted modes in stage B21 and B22 are investigated and included in Figure 4.6. The Torsion of Deck (TD) mode shape is present in predicted modes at higher frequencies. However, due to limited sensor locations, it is hard to determine which modes contain torsion of deck in analysis. Note that modes containing torsion of the deck are significantly higher in the predicted modes. TD mode is closely spaced to the TC mode, and the SSI method has problem in particular has problems with identifying this one.

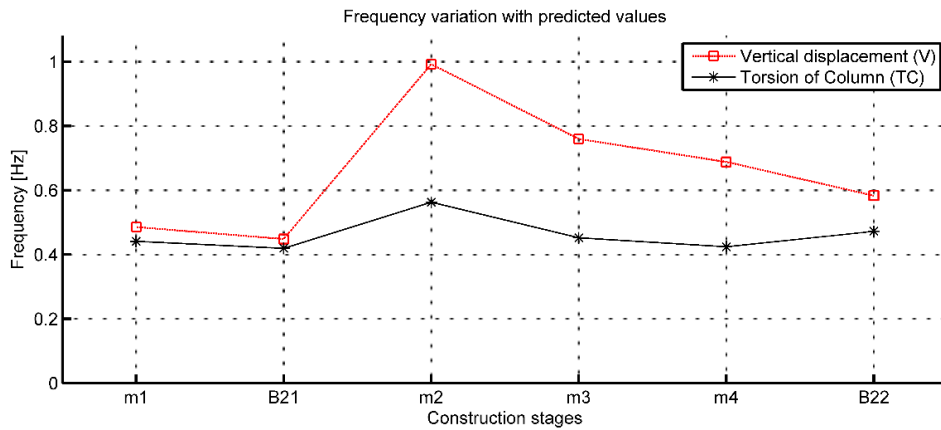


Figure 4.6 Frequency variation for construction stage m1-m4 and numerically predicted modes in B21 and B22.

B21 includes one cast stage more than analyzed stage m1. Both the corresponding V and TC modes have a frequency between m1 and B21. Hence, modes from predicted stage B21 follow the same tendencies as obtained by OMA. Note that the support structure is applied after B21. B22 corresponds to one cast stage after m4. The vertical displacement mode follows the assumed reduction in frequencies. However, the predicted torsion (TC) mode deviates from the observed tendency with an increasing value. Seen from Table 4-1, mode 1 for stage B22 contains bending of the cantilever, which does not occur for mode 1, B21. This might also affect the frequency.

Frequencies are regarded to be confidently and easily estimated [6]. Due to uncertainty of the obtained modes, this data does not provide enough validity to reject the predicted parameter, as several uncertainty factors are pronounced.

#### 4.2.2 Damping

Table 4-10 present damping ratio with respect to modes from different construction stages.

Table 4-10 Damping ratios obtained from casting stage m1-m4, given from two methods SOBI/SSI

SOBI/SSI	Series ID	Mode label		
		TC	V	TD
Stage 1	1	0.64/-	0.24/0.51	0.91/1.7
<b>Mean m1</b>		<b>0.64</b>	<b>0.38</b>	<b>1.3</b>
Stage 2	2	0.58/-	0.45/0.44	0.62/0.60
	3	0.73/-	0.35/0.58	0.51/-
	4	0.60/-	-/0.47	-
<b>Mean m2</b>		<b>0.63</b>	<b>0.46</b>	<b>0.58</b>
Stage 3	5	0.60/-	-/0.51	0.46/-
	6	0.55/0.57	0.56/-	0.49/-
<b>Mean m3</b>		<b>0.57</b>	<b>0.54</b>	<b>0.48</b>
Stage 4	7	0.50/0.41	0.40/0.51	-
	8	0.38/0.30	0.30/0.28	0.56/-
<b>Mean m4</b>		<b>0.40</b>	<b>0.38</b>	<b>0.56</b>

A large scatter of damping ratios from different time series is observed. Mode V for stage 4 have ratios going from 0.28-0.51. The mean should be used with care. Inaccurate damping estimates are a known problem in OMA, as it is usually characterized by large error bounds [6]. A linear system is assumed in OMA. However, damping consist of several damping mechanisms, with a linear damping independent of motion and an non-linear part, which denotes damping dependent of the amplitudes of motion [6]. Different series will give different amplitudes of motion. This can be seen for time series 7 and 8, where time series 7 has a consistently higher damping ratio than from time series 8. Series with different wind speeds add uncertainty to predicting the changes with respect to time stages. This should be noted as a limitation of the ability to compare the results. The duration since last cast will most likely affect the result, however this is not investigated any further.

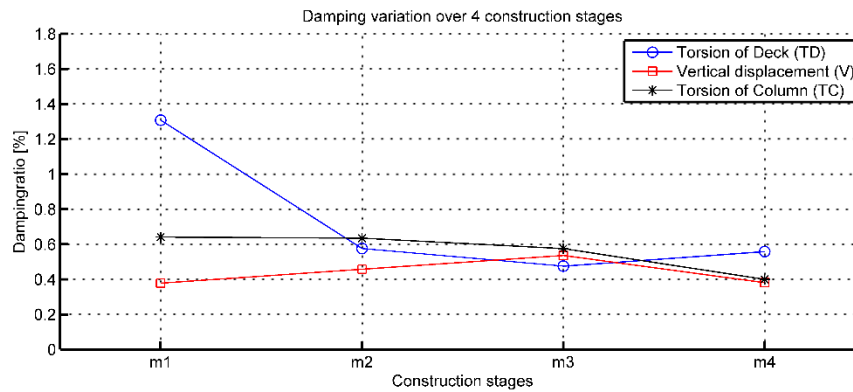


Figure 4.7 Mean values of damping ratios for different construction stages.

Figure 4.5 presents the estimated damping ratio over different construction stages. The mode labeled Torsion of Deck (TD) seems to give the highest scatter. The damping in the first stage may be rejected, due to the high damping ratio indicating noise or a spurious mode. The mean of the vertical displacement (V) mode is observed as consistently lower than the mean damping ratio from TC for the respective construction stages.

The applied SLS damping ratio for the predicted results is equal to 0.8 % [32]. This might be considered as an un-conservative estimate. However, with larger loading, the non-linear damping might increase resulting from friction and aerodynamic damping. The wind speed during construction stages was too low to investigate this relationship

## Chapter 5      Concluding remarks

The implemented SOBI method was tested with a 5 DOF shear frame with non-proportional damping. The accuracy of the obtained parameters in relation to the damping ratio was investigated, and the quality of the results was considerably reduced for higher damping ratios. The method showed noteworthy improvement for longer time series durations.

The SOBI-obtained parameters fall within the 95% confidence interval provided by the cov-SSI method for selected time series where variances were calculated. The methods found a different number of modes. The frequency deviations between the methods were small, but the methods provided varying damping estimates.

Three mode shapes are identified throughout the different construction stages. They are assumed to correspond to torsion in the column, vertical displacement of the cantilever, and torsion of the deck. The two first modes provided the best variance estimates obtained from cov-SSI. They were also the most frequently observed modes in the series investigated.

The change in eigenfrequencies during construction was investigated and the temporary structure was seen to have a significant effect on the eigenfrequency values. The eigenfrequencies rised after construction of the temporary structure, and then decreased with increasing construction stages. This is an expected tendency, as adding mass is likely to lower the eigenfrequencies. By comparison of the first two modes, the predicted first stage follows the obtained trend, while the predicted second building stage shows significant deviation. The last mode of interest in the experimental data appears at a lower frequency than the predicted mode.

Damping is estimated to be between 0.4-0.7% for the two modes which coincide with predicted mode shapes. The applied damping of 0.8% seen in the predictions is, therefore, found to be non-conservative for the investigated wind speed. However, a large amount of uncertainty is related to the damping estimates, and the results should be considered accordingly.

The number of sensors and the sensor layout are found critical in order to detect non-physical and correlated modes. Modal parameters obtained from a more extensive dataset will provide a more reliable result.

## Chapter 6 Further work

Different ways of establishing the whitening matrix in the SOBI method were investigated. Robust whitening does not require spatial white noise and is able to handle more noise. This was first investigated, but then rejected due to time limitations. The implemented SOBI method can be improved by adding the robust whitening found described in section 2.4.1.

The SOBI methods performance on non-proportional damping should be investigated more. The BMID algorithm could be implemented in order to improve the handling of complex modes [23]. This is merely adjustments on the preprocessing part of the implemented code, and an equivalent JAD code for complex number is available online [28].

Only a few data series from each stage are analyzed, and it is advantageous to investigate more time series to reduce the bias in the results. The results can be compared with analyses by other OMA methods. However, the quality obtained by two closely spaced sensor locations is limited for the purpose of modal assessment. It is therefore advised to use the dataset primarily for static investigations.

Other investigations of cantilever bridges should be performed. It is then important to require a minimum number of sensor locations to capture the different mode shapes. A sensor on each cantilever, as well as the column is regarded as a minimum layout. Preferably, due to bending modes of the cantilever, and the observability of torsion of deck, more sensors should be available. The sampling rate is important with regard to dynamic analyses and can with advantage be set equal 200 Hz for acceleration and strain measurements. The wind should preferably be sampled with a minimum of 20 Hz. The validity of a wireless data collection should be investigated due to the amount of record sample dropouts found during this study.





## Chapter 7      References

1. Catbas, F.N., et al., *Topics in Dynamics of Civil Structures, Volume 4: Proceedings of the 31st IMAC, A Conference on Structural Dynamics, 2013*. Vol. 4. 2013: Springer Science & Business Media.
2. Ewins, D.J., *Modal testing : theory, practice and application*. 2nd ed. ed. Modal testing 2. Vol. 10. 2000, Baldock: Research Studies Press.
3. Kwak, H.G. and J.K. Son, *Determination of design moments in bridges constructed by balanced cantilever method*. *Engineering Structures*, 2002. **24**(5): p. 639-648.
4. Statens Vegvesen. *Fv. 714 Dolmsundet*. 2014 [cited 2015 23.03.2015]; Available from: <http://www.vegvesen.no/Fylkesveg/fv714dolmsundet>.
5. Reynders, E., M. Schevenels, and G.D. Roeck, *Users manual, MACEC 3.3*, K. LEUVEN, Editor. 2014.
6. Rainieri, C. and G. Fabbrocino, *Operational Modal Analysis of Civil Engineering Structures*. 2014: Springer New York.
7. Rainieri, C. and G. Fabbrocino, *Accurate Damping Estimation by Automated OMA Procedures*, in *Topics in Dynamics of Civil Structures, Volume 4*, F.N. Catbas, et al., Editors. 2013, Springer New York. p. 1-9.
8. Bendat, J.S., *Random data : analysis and measurement procedures*, A.G. Piersol, Editor. 2010, Wiley: Hoboken, N.J.
9. Næss, A. and T. Moan, *Stochastic Dynamics of Marine Structures*. 2013, New York: Cambridge University Press.
10. Strømmen, E.N., *Theory of bridge aerodynamics*. 2010, Springer: Berlin.
11. Lallement, G. and D. J. Innmann, *A tutorial on complex eigenvalues*. 1995.
12. Chopra, A.K., *Dynamics of structures : theory and applications to earthquake engineering*. 4th ed. ed. Prentice-Hall international series in civil engineering and engineering mechanics. 2012, Boston, Mass: Prentice Hall.
13. Strømmen, E.N., *Structural Dynamics*, SpringerLink, Editor. 2014.

14. Brincker, R., et al., *Identification of Dynamical Properties from Correlation Function Estimates*. Aalborg: Danish Society for Structural Science and Engineering, 1992. **63**.
15. Donnelly, D. and B. Rust, *The fast Fourier transform for experimentalists*. Computing in Science & Engineering, 2005. **7**(3): p. 71.
16. Kreyszig, E., H. Kreyszig, and E.J. Norminton, *Advanced engineering mathematics*. 10th ed., international student version. ed. 2011, Hoboken, N.J: Wiley.
17. Harris, F.J., *On the use of windows for harmonic analysis with the discrete Fourier transform*. Proceedings of the IEEE, 1978. **66**(1): p. 51-83.
18. Welch, P.D., *The use of fast Fourier transform for the estimation of power spectra: A method based on time averaging over short, modified periodograms*. Audio and Electroacoustics, IEEE Transactions on, 1967. **15**(2): p. 70-73.
19. Leis, J., *Digital Signal Processing Using MATLAB for Students and Researchers*. 2011, Hoboken, NJ, USA: John Wiley & Sons.
20. A Belouchrani, K.A.-M., JF Cardoso, E Moulines, *A Blind Source Separation Technique Using Second-Order Statistics*. Signal Processing, IEEE Transaction on, 1997. **45**(2): p. 434-444.
21. Poncelet, F., et al., *Output-only modal analysis using blind source separation techniques*. Mechanical Systems and Signal Processing, 2007. **21**(6): p. 2335-2358.
22. Rainieri, C., *Perspectives of Second-Order Blind Identification for Operational Modal Analysis of Civil Structures*. Shock and Vibration, 2014. **2014**: p. 9.
23. McNeill, S.I. and D.C. Zimmerman, *A framework for blind modal identification using joint approximate diagonalization*. Mechanical Systems and Signal Processing, 2008. **22**(7): p. 1526-1548.
24. Belouchrani, A. and A. Cichocki, *Robust whitening procedure in blind source separation context*. Electronics Letters, 2000. **36**(24): p. 2050-2051.
25. Jean-François Cardoso, A.S., *Jacobi Angles for Simultaneous Diagonalization*. SIAM Journal on Matrix Analysis and Applications, 1996. **17**: p. 161-164.
26. Peeters, B., *System Identification and Damage Detection in Civil Engineering*. 2000.
27. Reynders, E. and G.D. Roeck, *Reference-based combined deterministic–stochastic subspace identification for experimental and operational modal analysis*. Mechanical Systems and Signal Processing, 2008. **22**(3): p. 617-637.

- 
28. Cardoso, J.F. *JOINT DIAGONALIZATION*. Available from: <http://perso.telecom-paristech.fr/~cardoso/jointdiag.html>.
  29. Statens Vegvesen, *16-1481 Dolmsundbrua Konstruksjonsberegninger, K1: Prosjekteringsgrunnlag*. 2013.
  30. Statens Vegvesen. 2014 Illustration available from [www.vegvesen.no](http://www.vegvesen.no).
  31. Elektro1 Hitra & Frøya. 2014, [www.e1hf.no](http://www.e1hf.no). Picture obtained from Facebook and is used with permission.
  32. Statens Vegvesen, *16-1481 Dolmsundbrua, Beregninger Kapittel 2: Globalanalyser*. 2013.
  33. Cautus Geo, *Fv. 714 Dolmsundprosjektet -Installasjonsrapport Akse 2*. 2014.
  34. Rainieri, C., G. Fabbrocino, and E. Cosenza. *On damping experimental estimation*. in *Proceedings of 10th international conference on computational structures technology, Valencia*. 2010.



## A Selected time series

Eight different time series from four construction stages are analyzed. A description of the time series investigated us provided in Table A-1. Corresponding date, Start time and construction stage are shown. All series have a duration of 30 minutes.

*Table A-1 Date and time of collected time series*

ID	Date	Start time	Construction stage
1	06.10.2014	23.01.01	m1
2	03.12.2014	20.29.56	m2
3	03.12.2014	21.04.42	m2
4	03.12.2014	07.03.35	m2
5	13.01.2015	02.25.29	m3
6	13.01.2015	03.30.17	m3
7	27.01.2015	21.15.01	m4
8	27.01.2015	21.57.02	m4

The time series corresponding file names are given in Table A-2. The name is given for x-direction and part000, although all directions and several parts are included in the analysis.

*Table A-2 Time series with corresponding filenames.*

ID	Filename from sensor: Ax1	Filename from sensor: Ax2
1	'Streaming_0_x_0_0_x_00158D00000E03B0_06-10-2014_22.48.40_part000.txt'	'Streaming_0_x_0_0_x_00158D00000E0462_06-10-2014_22.47.32_part000.txt'
2	'Streaming_0_x_0_0_x_00158D00000E03B0_03-12-2014_20.02.11_part000.txt'	'Streaming_0_x_0_0_x_00158D00000E0462_03-12-2014_20.04.38_part000.txt'
3	'Streaming_0_x_0_0_x_00158D00000E03B0_03-12-2014_21.02.15_part000.txt'	'Streaming_0_x_0_0_x_00158D00000E0462_03-12-2014_21.04.42_part000.txt'
4	Streaming_0_x_0_0_x_00158D00000E03B0_03-12-2014_07.01.10_part000.tx	'Streaming_0_x_0_0_x_00158D00000E0462_03-12-2014_07.03.37_part000.txt'
5	Streaming_0_x_0_0_x_00158D00000E03B0_13-01-2015_02.25.29_part000.txt'	Streaming_0_x_0_0_x_00158D00000E0462_13-01-2015_02.22.28_part000.txt'
6	'Streaming_0_x_0_0_x_00158D00000E03B0_13-01-2015_03.25.33_part000.txt'	'Streaming_0_x_0_0_x_00158D00000E0462_13-01-2015_03.22.32_part000.txt'
7	'Streaming_0_x_0_0_x_00158D00000E03B0_27-01-2015_20.46.27_part000.txt'	'Streaming_0_x_0_0_x_00158D00000E0462_27-01-2015_20.56.58_part000.txt'
8	'Streaming_0_x_0_0_x_00158D00000E03B0_27-01-2015_21.46.31_part000.txt'	'Streaming_0_x_0_0_x_00158D00000E0462_27-01-2015_21.57.02_part000.txt'



## B Result from all investigated time series

Time series analyzed with cov-SSI are preprocessed with a Butterworth filter of order 6 with high-pass  $f_c = 0.2 \text{ Hz}$  and low-pass  $f_c = 3 \text{ Hz}$ . The time series are decimated to  $f_s = 10 \text{ Hz}$ . Number of Block rows  $i$  and number of blocks for covariance estimates inserted in MACEC are provided in Table B-1.

Time series analyzed with SOBI are preprocessed with a lower low-pass filter  $f_c$  than SSI. This was found necessary in order to receive separated sources. A lower  $f_c = 0.2 \text{ Hz}$  is used for all time series. The higher  $f_c$  for distinct time series is given in Table B-1. The time series are decimated to 25 Hz.

*Table B-1 Parameters variations for different time series*

ID	SOBI	Block rows $i$	SSI
	<i>higher</i> $f_c$ [Hz]		Blocks-covariance estimates
1	0.8	50	60
2	1.5	50	60
3	1.5	50	-
4	1.5	30	-
5	1	50	-
6	1	50	-
7	1.5	30	69
8	1	50	-

The modes in the result section are labeled after assumed mode shape. TC denotes Torsion of Column, V denotes Vertical displacement of cantilever and TD represent Torsion of Deck. U labels an undetermined/nonphysical mode. Positions of sensors were adjusted late in the study. Accelerometer positions were first assumed placed on each cantilever, therefore, some modes which are later considered nonphysical are included in comparison between the methods. However, they are not included in comparison of different construction stages given in the main document.

This appendix presents all modes found from the stabilization diagram and separation of sources. However, many modes were found to have high confidence interval from cov-SSI, not separated by SOBI or unrealistic damping. The consistence between the mode is checked, and the modes which followed the observed TC, V and TD mode shaped and showed best quality are selected. A comprehensive overview from the included mode is given in main document in Table 4-8 and Table 4-10.

Note, results from time series ID7 are not included in appendix since a full description of the results are provided in main report section 4.1.



## B.1 Results from time series ID01

### B.1.1 Result from cov-SSI

Modes found from stabilization diagram is presented with a  $2\sigma$  confidence interval.

Table B-2 cov-SSI result from time series ID01, given with  $2\sigma$  confidence interval

Mode	$f_n$ [Hz]	$\xi$ [%]	MPC	MP	MPD	Label
1	$0,4423 \pm 0,0055$	$1,081 \pm 1,0420$	0,99	0,847	5,56	U
2	$0,4443 \pm 0,0026$	$0,530 \pm 0,6517$	0,62	13,5	24,0	U
3	$0,4846 \pm 0,0033$	$0,514 \pm 0,4390$	0,99	0,38	2,88	V
4	$0,4862 \pm 0,0043$	$1,701 \pm 1,2324$	0,75	10,4	14,1	TD

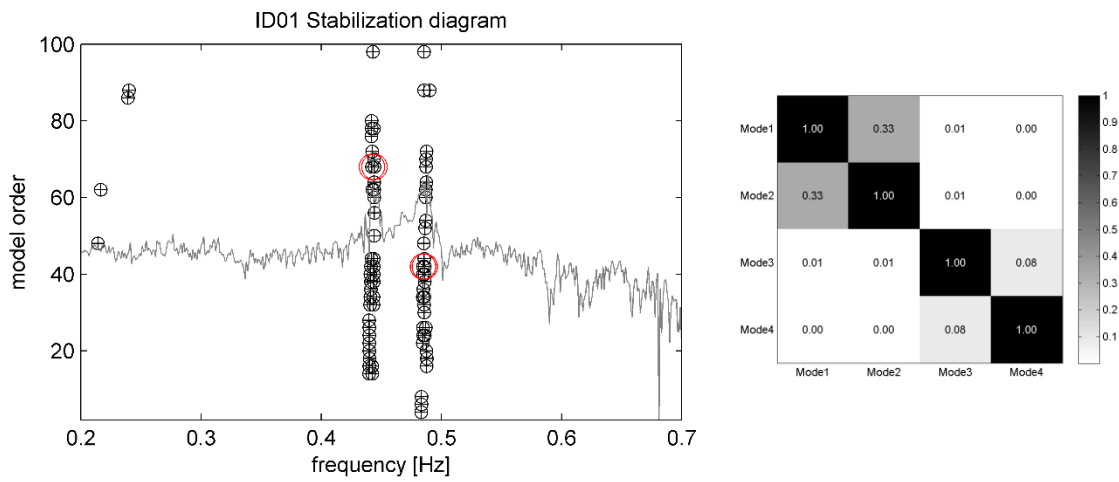


Figure B.1 a) Stabilization diagram b) AutoMAC matrix, time series ID01

### B.1.2 Results from SOBI

Table B-3 SOBI result from time series ID01

Mode	$f_n$ [Hz]	$\xi$ [%]	Source number	Label
1	0,440845	0,6411	3	T
2	0,444061	0,6177	4	U
3	0,48604	0,2415	1	V
4	0,486622	0,9144	6	TD

No correlation between the modes are found in AutoMAC matrix.

### B.1.3 Comparison

Table B-4 Comparison of SOBI and SSI modes from time series ID01

SOBI/ SSI	$\Delta f_n$ [%]	$\Delta \xi_n$ [%]	MAC	Mode label
2/2	0,046	16,6	0,79	U
3/3	0,291	53,1	0,98	V
4/4	0,084	46,3	0,92	TD

Notice that the damping and frequencies from SOBI falls within the confidence interval provided by cov-SSI.

## B.2 Time series ID02

### B.2.1 Result from cov-SSI

Modes found from stabilization diagram is presented with a  $2\sigma$  confidence interval.

Table B-5 cov-SSI result from time series ID02, given with  $2\sigma$  confidence interval

Mode	$f_n$ [Hz]	$\xi$ [%]	MPC	MP	MPD	Label
1	$0,5632 \pm 0,0020$	$0,5604 \pm 0,2794$	0,58	9,93	20,3	T
2	$0,9903 \pm 0,0021$	$0,4426 \pm 0,2936$	0,79	9,49	12,8	V
3	$0,9947 \pm 0,0034$	$0,5958 \pm 0,3343$	0,72	13,4	15,9	TD
4	$1,1199 \pm 0,0338$	$1,1282 \pm 5,3937$	0,84	0,85	10,6	V/TD

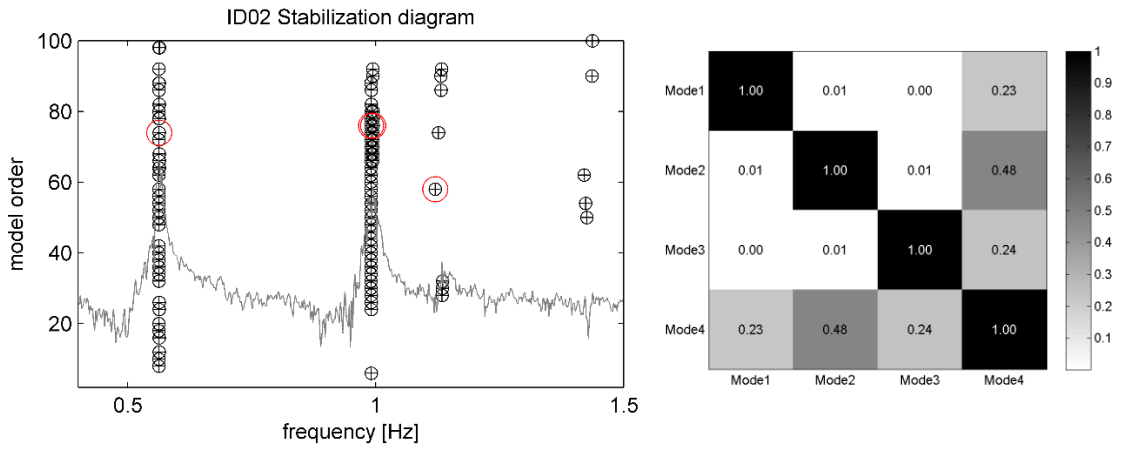


Figure B.2 a) Stabilization diagram b) AutoMAC matrix, time series ID02

Mode 4 is rejected due to its high confidence interval. It is also seen to correlate with the other modes as seen in the AutoMAC matrix in Figure B.2 b).

### B.2.2 Results from SOBI

Table B-6 SOBI results from time series ID02

Mode	$f_n$ [Hz]	$\xi$ [%]	Source number	Label
1	0,5626	0,6395	3	U
2	0,5635	0,5754	1	T
3	0,9909	0,4459	2	V
4	0,9930	0,6167	4	TD

### B.2.3 Comparison

Table B-7 Comparison of SOBI and SSI modes from time series ID02

SOBI/ SSI	$\Delta f_n$ [%]	$\Delta \xi_n$ [%]	MAC	Mode label
2/1	0,0518	2,6844	0,4905	T
3/2	0,0601	0,7464	0,8555	V
4/3	0,1766	3,5067	0,8356	TD

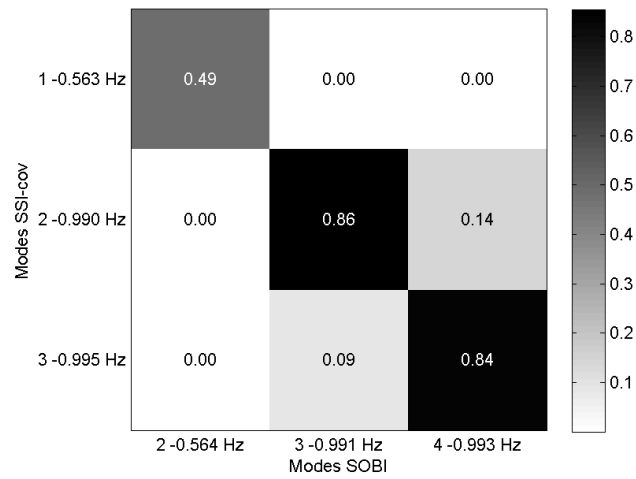


Figure B.3 CrossMAC matrix, comparing modes from cov-SSI and SOBI.

Note the low MAC value between mode 2/1 from SOBI/SSI. See the high complexity of mode 1 from SSI. Recall that SOBI method does not provide complex modes.

## B.3 Time series ID03

### B.3.1 Result from cov-SSI

Table B-8 cov-SSI result from time series ID03

Mode	$f_n$ [Hz]	$\xi$ [%]	MPC	MP	MPD	Label
1	0,5606	0,6633	0,58	10,2	21,1	U
2	0,9897	0,5760	0,99	1,97	3,64	V

Higher stabilization limits were used in this case, given as frequency=2% damping=10% and vectors 2%.

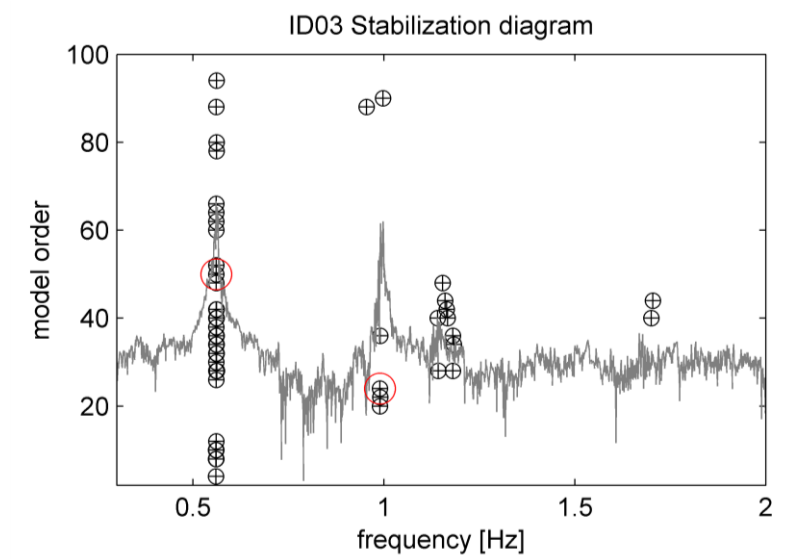


Figure B.4 Stabilization diagram, ID03.

It should be noted that the recognized nonphysical mode shape does have a significant and clear peak in the PSD spectrum, plotted on the top of the stabilization diagram in Figure B.4.

### B.3.2 Results from SOBI

Table B-9 SOBI results from time series ID03

Mode	$f_n$ [Hz]	$\xi$ [%]	Source number	Label
1	0,561	0,577	1	U
2	0,563	0,728	3	T/U
3	0,992	0,514	4	TD
4	0,993	0,351	2	V

### B.3.3 Comparison

Table B-10 Comparison of SOBI and SSI modes from time series ID03

SOBI/ SSI	$\Delta f_n$ [%]	$\Delta \xi_n$ [%]	MAC	Mode label
1/1	0,134	13,04	0,586	U
4/2	0,292	39,13	0,930	V



## B.4 Time series ID04

### B.4.1 Result from cov-SSI

Table B-11 cov-SSI result from time series ID04

Mode	$f_n$ [Hz]	$\xi$ [%]	MPC	MP	MPD	Label
1	0,5646	0,6208	0,99	1,70	2,88	U
2	0,9954	0,4722	0,97	2,61	4,72	V

Higher stabilization limits were used in this case. frequency=3% damping=10% and vectors 3%.

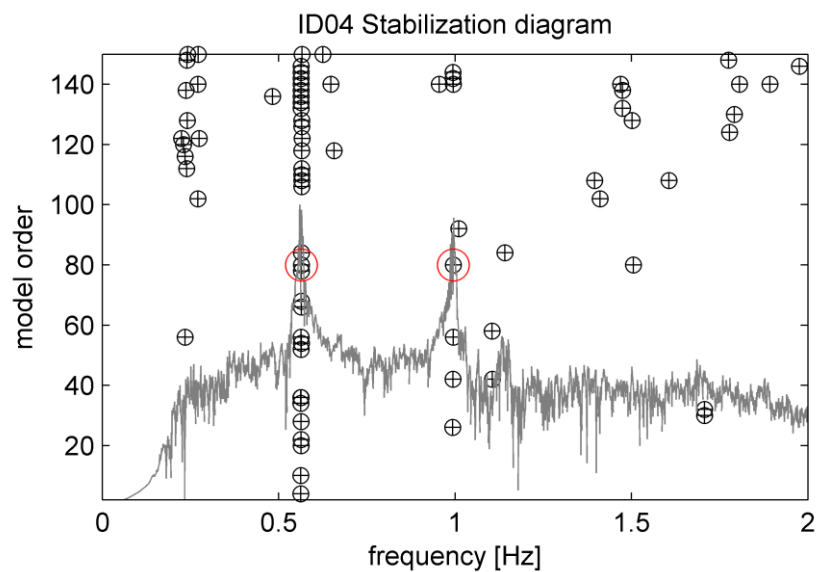


Figure B.5 Stabilization diagram

Mode 1 is labelled as undetermined mode due to unexpected mode shape behaviour. Note the corresponding peak in the PSD plot, which is seen to represent a physical mode.

### B.4.2 Results from SOBI

Table B-12 SOBI result from time series ID04

Mode	$f_n$ [Hz]	$\xi$ [%]	Source number	Label
1	0,5620	0,60	3	U/T
2	0,5624	0,56	1	U
3	0,9929	0,36	2	V*
4	0,9932	0,34	4	V*

\*only displacement in one DOF

### B.4.3 Comparison

Table B-13 Comparison of SOBI and SSI modes from time series ID04

SOBI/ SSI	$\Delta f_n$ [%]	$\Delta \xi_n$ [%]	MAC	Mode label
2/1	0,394	9,12	0,75	U
4/2	0,226	27,7	0,88	V



## B.5 Time series ID05

### B.5.1 Result from cov-SSI

Table B-14 cov-SSI result from time series ID05

Mode	$f_n$ [Hz]	$\xi$ [%]	MPC	MP	MPD	Label
1	0,7593	0,5113	0,89	8,75	9,31	V
2	1,498	0,4188	0,90	-10,9	8,06	V/U
3	1,629	0,5613	0,85	7,97	13,2	U

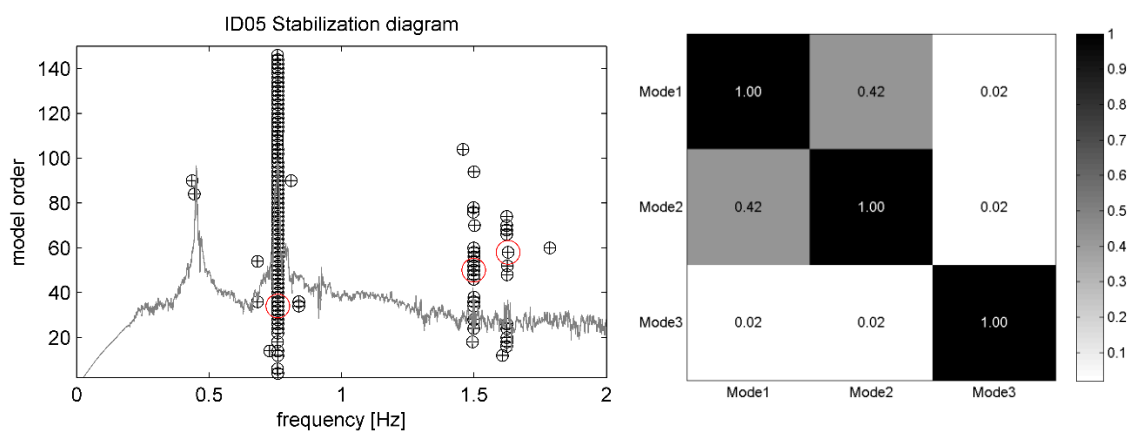


Figure B.6 a) Stabilization diagram b) AutoMAC matrix of modes from cov-SSI, time series ID05

Note from stabilization diagram. Peak just below 0.5 Hz had unrealistic high damping, 19%, and was regarded as a spurious mode. The AutoMAC matrix reveals high correlation between mode 1 and 2.

### B.5.2 Results from SOBI

Table B-15 SOBI result from time series ID05

Mode	$f_n$ [Hz]	$\xi$ [%]	Source number	Label
1	0,4522	0,39	3	U
2	0,4526	0,60	2	T
3	0,7584	0,46	1	TD

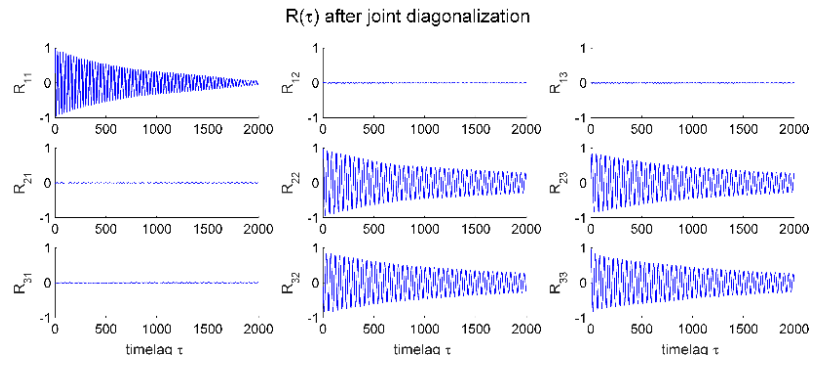


Figure B.7 Cross correlation matrix from SOBI, time series ID05

Note from the correlations between source 2 and 3, which implies a not separated source.

### B.5.3 Comparison

Table B-16 Comparison of SOBI and SSI modes from time series ID05

SOBI/ SSI	$\Delta f_n$ [%]	$\Delta \xi_n$ [%]	MAC	Mode label
1/1	0,124	9,10	0,97	U

## B.6 Time series ID06

### B.6.1 Result from cov-SSI

Table B-17 cov-SSI result from time series ID06

Mode	$f_n$ [Hz]	$\xi$ [%]	MPC	MP	MPD	Label
1	$0,4521 \pm 0,001$	$0,5676 \pm 0,2026$	0,65	-17,0	18,3	T

Higher stabilization limits were used in this case. frequency=2% damping=10% and vectors 2%.

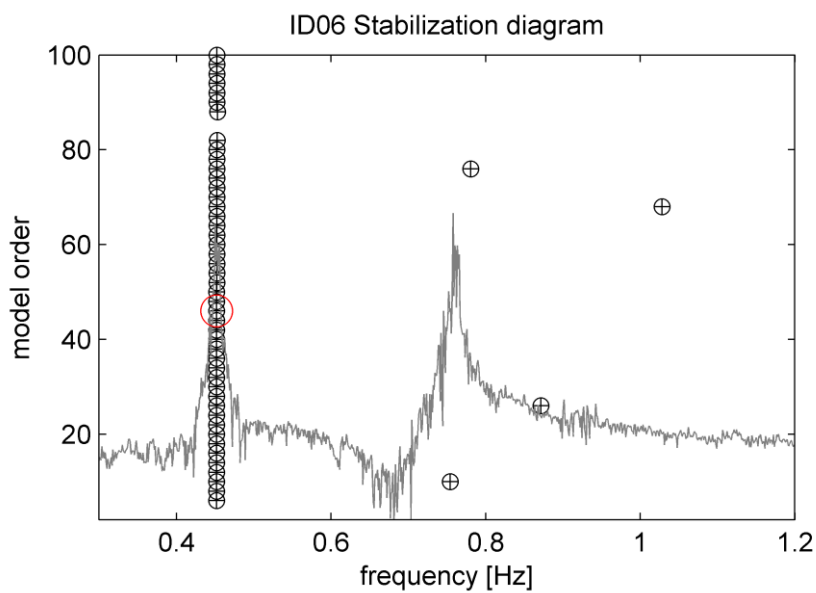


Figure B.8 Stabilization diagram obtained from time series ID06

No alignments of poles for the peak seen in the PSD plot just below 0.8 Hz.

### B.6.2 Results from SOBI

Table B-18 SOBI result from time series ID06

Mode	$f_n$ [Hz]	$\xi$ [%]	Source number	Label
1	0,4501	0,56	4	U
2	0,4508	0,55	2	T
3	0,7596	0,56	1	V
4	0,7608	0,48	3	TD

### B.6.3 Comparison

Table B-19 Comparison of SOBI and SSI modes from time series ID06

SOBI/ SSI	$\Delta f_n$ [%]	$\Delta \xi_n$ [%]	MAC	Mode label
2/1	-0,28	-2,48	0,90	T



## B.7 Time series ID08

### B.7.1 Result from cov-SSI

Table B-20 cov-SSI result from time series ID08

Mode	$f_n$ [Hz]	$\xi$ [%]	MPC	MP	MPD	Label
1	0,4243	0,3024	1,00	1,29	2,48	T
2	0,6872	0,2834	0,64	15,8	18,4	V/TD

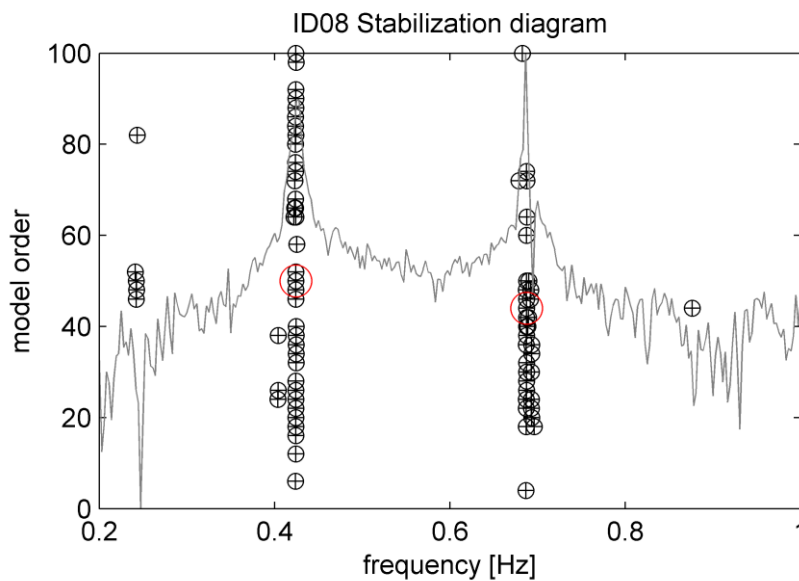


Figure B.9 Stabilization diagram from ID08

### B.7.2 Results from SOBI

Table B-21 SOBI result from time series ID08

Mode	$f_n$ [Hz]	$\xi$ [%]	Source number	Label
1	0,4240	0,38	2	T
2	0,6867	0,30	1	V
3	0,6966	0,56	3	TD

### B.7.3 Comparison

Table B-22 Comparison of SOBI and SSI modes from time series ID08

Mode SOBI/Mode	$\Delta f_n$ [%]	$\Delta \xi_n$ [%]	MAC	Mode label
1/1	0,052	27,08	0,98	T
2/2	0,080	6,699	0,88	V